

RL-TR-96-126
In-House Report
May 1996



IMAGE RECONSTRUCTION FROM STRONGLY SCATTERING PENETRABLE OBJECTS USING A DIFFERENTIAL CEPSTRAL FILTER

John B. Morris

APPROVED FOR PUBLIC RELEASE; DISTRIBUTION UNLIMITED.

19980602 120

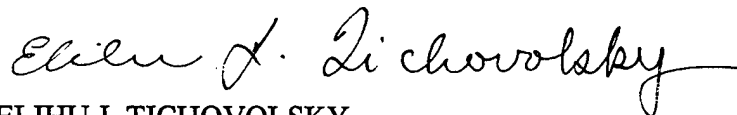
DTIC QUALITY INSPECTED 4
DTIC QUALITY INSPECTED 4

Rome Laboratory
Air Force Materiel Command
Rome, New York

This report has been reviewed by the Rome Laboratory Public Affairs Office (PA) and is releasable to the National Technical Information Service (NTIS). At NTIS it will be releasable to the general public, including foreign nations.

RL-TR-96-126 has been reviewed and is approved for publication.

APPROVED:



ELIHU J. TICHOVOLSKY
Acting Chief, Applied Electromagnetics Division
Electromagnetics & Reliability Directorate

FOR THE COMMANDER:



ROBERT V. McGAHAN
Acting Director
Electromagnetics & Reliability Directorate

If your address has changed or if you wish to be removed from the Rome Laboratory mailing list, or if the addressee is no longer employed by your organization, please notify Rome Laboratory/ERCS, Hanscom AFB, MA 01731. This will assist us in maintaining a current mailing list.

Do not return copies of this report unless contractual obligations or notices on a specific document require that it be returned.

REPORT DOCUMENTATION PAGE			Form Approved OMB No. 0704-0188	
Public reporting burden for this collection of information is estimated to average 1 hour per response, including the time for reviewing instructions, searching existing data sources, gathering and maintaining the data needed, and completing and reviewing the collection of information. Send comments regarding this burden estimate or any other aspect of this collection of information, including suggestions for reducing this burden, to Washington Headquarters Services, Directorate for Information Operations and Reports, 1215 Jefferson Davis Highway, Suite 1204, Arlington, VA 22202-4302, and to the Office of Management and Budget, Paperwork Reduction Project (0704-0188), Washington, DC 20503.				
1. AGENCY USE ONLY (Leave blank)		2. REPORT DATE May 1996		3. REPORT TYPE AND DATES COVERED Scientific In-House (1 Jul 1994-1 April 1995)
4. TITLE AND SUBTITLE Image Reconstruction From Strongly Scattering Penetrable Objects Using a Differential Cepstral Filter			5. FUNDING NUMBERS PE 62702F PR 4600 TA 15 WU 14	
6. AUTHOR(S) John B. Morris				
7. PERFORMING ORGANIZATION NAME(S) AND ADDRESS(ES) Rome Laboratory/ERCS 31 Grenier St Hanscom AFB, MA 01731-3010			8. PERFORMING ORGANIZATION REPORT NUMBER RL-TR-96-126	
9. SPONSORING / MONITORING AGENCY NAME(S) AND ADDRESS(ES)			10. SPONSORING / MONITORING AGENCY REPORT NUMBER	
11. SUPPLEMENTARY NOTES Rome Laboratory Project Engineer: John B. Morris/ERCS, 617-377-3439				
12a. DISTRIBUTION / AVAILABILITY STATEMENT Approved for public release; distribution unlimited.			12b. DISTRIBUTION CODE	
13. ABSTRACT (Maximum 200 words) Conventional algorithms for media characterization in diffraction tomography rely on weakly scattering approximations such as the Born or Rytov methods. In this report, we investigate the utility of a nonlinear filtering procedure applied to single-view backpropagated images of strongly scattering two-dimensional objects. With a single illumination direction and constant wavenumber k_0 , exact scattered far fields are backpropagated to form an image of the scattering potential times the total field. The multiplicative field, in this case, precludes one from ascertaining quantitative information on the scattering potential. We apply a differential cepstral filter to single-view backpropagated images in order to remove the perturbing field. Phase wrapping problems associated with cepstral filtering procedures are avoided in the differential cepstrum, since phase ambiguities introduced by the complex algorithm are avoided in its definition. Exact scattering solutions are used from several strongly scattering cylinders ranging from $k_0 a(\sqrt{\epsilon_r} - 1) = 2$ to $k_0 a(\sqrt{\epsilon_r} - 1) = 41$ where a is the maximum dimension of the object and ϵ_r is the relative permittivity. For the lower range, the filtered single-view backpropagated images are superior to the unfiltered. As the range increases, object features become less resolved due to the limited Fourier data available. Results and limitations of the proposed methods are discussed.				
14. SUBJECT TERMS Differential cepstral filter Born approximation Rytov approximation Image reconstruction Penetrable targets Backpropagation			15. NUMBER OF PAGES 118	
			16. PRICE CODE	
17. SECURITY CLASSIFICATION OF REPORT Unclassified	18. SECURITY CLASSIFICATION OF THIS PAGE Unclassified	19. SECURITY CLASSIFICATION OF ABSTRACT Unclassified	20. LIMITATION OF ABSTRACT SAR	

Contents

1	INTRODUCTION	1
2	SCATTERED FIELD IN A TWO-DIMENSIONAL INHOMOGENEOUS REGION	3
3	BORN APPROXIMATION	5
4	RYTOV APPROXIMATION	7
5	FAR-FIELD TRANSVERSE MAGNETIC (TM) SCATTERING FROM A CIRCULAR CYLINDER	9
6	FAR-FIELD TRANSVERSE MAGNETIC (TM) SCATTERING FROM TWO CONCENTRIC CYLINDERS	18
7	IMAGE RECONSTRUCTION ALGORITHM	21
8	BORN RECONSTRUCTIONS	31
9	DIFFERENTIAL CEPSTRAL FILTERING	34
10	DIFFERENTIAL CEPSTRAL FILTERING APPLIED TO EXACT $V \frac{\Psi}{\Psi^i}$	48

11	DIFFERENTIAL CEPSTRAL FILTERING APPLIED TO SINGLE- VIEW BACKPROPAGATED $\nabla \frac{\Psi}{\Psi^i}$	60
12	DIFFERENTIAL CEPSTRAL FILTERING APPLIED TO SINGLE- VIEW BACKPROPAGATED $\nabla \frac{\Psi}{\Psi^i}$ USING A PRIORI KNOWLEDGE OF THE OBJECT'S SUPPORT	71
13	DIFFERENTIAL CEPSTRAL FILTER APPLIED TO MEASURED DATA	86
14	CONCLUSIONS	92
15	RECOMMENDATIONS	93
	REFERENCES	95
A	FAR-FIELD APPROXIMATION	99
B	2-D INVERSE FOURIER TRANSFORM	101
C	SIMULATED SCATTERED FAR-FIELDS	103

Illustrations

1	Cross section of homogeneous dielectric cylinder of radius a .	10
2	Total field intensity internal and external to a homogeneous dielectric cylinder of radius 0.0425 m and relative permittivity $\epsilon_r = 1.0$ under plane wave illumination at 10 GHz. Field-of-view is 0.1984 m on each side.	13
3	Total field intensity internal and external to a homogeneous dielectric cylinder of radius 0.0425 m and relative permittivity $\epsilon_r = 1.1$ under plane wave illumination at 10 GHz. Field-of-view is 0.1984 m on each side.	13
4	Total field intensity internal and external to a homogeneous dielectric cylinder of radius 0.0425 m and relative permittivity $\epsilon_r = 1.2$ under plane wave illumination at 10 GHz. Field-of-view is 0.1984 m on each side.	14
5	Total field intensity internal and external to a homogeneous dielectric cylinder of radius 0.0425 m and relative permittivity $\epsilon_r = 1.4$ under plane wave illumination at 10 GHz. Field-of-view is 0.1984 m on each side.	14
6	Total field intensity internal and external to a homogeneous dielectric cylinder of radius 0.0425 m and relative permittivity $\epsilon_r = 1.8$ under plane wave illumination at 10 GHz. Field-of-view is 0.1984 m on each side.	15
7	Total field intensity internal and external to a homogeneous dielectric cylinder of radius 0.0425 m and relative permittivity $\epsilon_r = 2.2$ under plane wave illumination at 10 GHz. Field-of-view is 0.1984 m on each side.	15
8	Total field intensity internal and external to a homogeneous dielectric cylinder of radius 0.0425 m and relative permittivity $\epsilon_r = 2.56$ under plane wave illumination at 10 GHz. Field-of-view is 0.1984 m on each side.	16
9	Total field intensity internal and external to a homogeneous dielectric cylinder of radius 0.0425 m and relative permittivity $\epsilon_r = 3.0$ under plane wave illumination at 10 GHz. Field-of-view is 0.1984 m on each side.	16

10	Total field intensity internal and external to a homogeneous dielectric cylinder of radius 0.0425 m and relative permittivity $\epsilon_r = 5.0$ under plane wave illumination at 10 GHz. Field-of-view is 0.1984 m on each side.	17
11	Total field intensity internal and external to a homogeneous dielectric cylinder of radius 0.0425 m and relative permittivity $\epsilon_r = 10.0$ under plane wave illumination at 10 GHz. Field-of-view is 0.1984 m on each side.	17
12	Cross section of two concentric cylinders of inner radius a and outer radius b .	19
13	Total field intensity internal and external to two concentric dielectric cylinders (inner radius 0.0215 m and outer radius 0.0425 m) under plane wave illumination at 10 GHz. Relative permittivity of inner cylinder is fixed at $\epsilon_r = 2.2$ and relative permittivity of outer annulus is $\epsilon_r = 1.0$ Field-of-view is 0.1984 m on each side.	22
14	Total field intensity internal and external to two concentric dielectric cylinders (inner radius 0.0215 m and outer radius 0.0425 m) under plane wave illumination at 10 GHz. Relative permittivity of inner cylinder is fixed at $\epsilon_r = 2.2$ and relative permittivity of outer annulus is $\epsilon_r = 1.1$ Field-of-view is 0.1984 m on each side.	22
15	Total field intensity internal and external to two concentric dielectric cylinders (inner radius 0.0215 m and outer radius 0.0425 m) under plane wave illumination at 10 GHz. Relative permittivity of inner cylinder is fixed at $\epsilon_r = 2.2$ and relative permittivity of outer annulus is $\epsilon_r = 1.2$ Field-of-view is 0.1984 m on each side.	23
16	Total field intensity internal and external to two concentric dielectric cylinders (inner radius 0.0215 m and outer radius 0.0425 m) under plane wave illumination at 10 GHz. Relative permittivity of inner cylinder is fixed at $\epsilon_r = 2.2$ and relative permittivity of outer annulus is $\epsilon_r = 1.4$ Field-of-view is 0.1984 m on each side.	23
17	Total field intensity internal and external to two concentric dielectric cylinders (inner radius 0.0215 m and outer radius 0.0425 m) under plane wave illumination at 10 GHz. Relative permittivity of inner cylinder is fixed at $\epsilon_r = 2.2$ and relative permittivity of outer annulus is $\epsilon_r = 1.8$ Field-of-view is 0.1984 m on each side.	24
18	Total field intensity internal and external to two concentric dielectric cylinders (inner radius 0.0215 m and outer radius 0.0425 m) under plane wave illumination at 10 GHz. Relative permittivity of inner cylinder is fixed at $\epsilon_r = 2.2$ and relative permittivity of outer annulus is $\epsilon_r = 2.2$ Field-of-view is 0.1984 m on each side.	24
19	Total field intensity internal and external to two concentric dielectric cylinders (inner radius 0.0215 m and outer radius 0.0425 m) under plane wave illumination at 10 GHz. Relative permittivity of inner cylinder is fixed at $\epsilon_r = 2.2$ and relative permittivity of outer annulus is $\epsilon_r = 2.56$ Field-of-view is 0.1984 m on each side.	25
20	Total field intensity internal and external to two concentric dielectric cylinders (inner radius 0.0215 m and outer radius 0.0425 m) under plane wave illumination at 10 GHz. Relative permittivity of inner cylinder is fixed at $\epsilon_r = 2.2$ and relative permittivity of outer annulus is $\epsilon_r = 3.0$ Field-of-view is 0.1984 m on each side.	25
21	Total field intensity internal and external to two concentric dielectric cylinders (inner radius 0.0215 m and outer radius 0.0425 m) under plane wave illumination	

	at 10 GHz. Relative permittivity of inner cylinder is fixed at $\epsilon_r = 2.2$ and relative permittivity of outer annulus is $\epsilon_r = 5.0$ Field-of-view is 0.1984 m on each side.	26
22	Total field intensity internal and external to two concentric dielectric cylinders (inner radius 0.0215 m and outer radius 0.0425 m) under plane wave illumination at 10 GHz. Relative permittivity of inner cylinder is fixed at $\epsilon_r = 2.2$ and relative permittivity of outer annulus is $\epsilon_r = 10.0$ Field-of-view is 0.1984 m on each side.	26
23	Radial cuts in relative permittivity for various cylinders under investigation a) obj_1.1/1.03 b) obj_1.03/1.1 c) obj_4/4 d) obj_4/2 e) obj_2/4.	32
23	(cont.) Radial cuts in relative permittivity for various cylinders under investigation a) obj_1.1/1.03 b) obj_1.03/1.1 c) obj_4/4 d) obj_4/2 e) obj_2/4.	33
24	Real part of equivalent Born reconstruction of obj_1.1/1.03 using 15 equally spaced illumination directions. Field-of-view 64x64 cm ² .	35
25	Imaginary part of equivalent Born reconstruction of obj_1.1/1.03 using 15 equally spaced illumination directions. Field-of-view 64x64 cm ² .	35
26	Magnitude of equivalent Born reconstruction of obj_1.1/1.03 using 15 equally spaced illumination directions. Field-of-view 64x64 cm ² .	36
27	One dimensional slice through the center of Figure 26. Length of slice is 64cm.	36
28	Real part of equivalent Born reconstruction of obj_1.03/1.1 using 15 equally spaced illumination directions. Field-of-view 64x64 cm ² .	37
29	Imaginary part of equivalent Born reconstruction of obj_1.03/1.1 using 15 equally spaced illumination directions. Field-of-view 64x64 cm ² .	37
30	Magnitude of equivalent Born reconstruction of obj_1.03/1.1 using 15 equally spaced illumination directions. Field-of-view 64x64 cm ² .	38
31	One dimensional slice through the center of Figure 30. Length of slice is 64cm.	38
32	Real part of equivalent Born reconstruction of obj_4/4 using 15 equally spaced illumination directions. Field-of-view 64x64 cm ² .	39
33	Imaginary part of equivalent Born reconstruction of obj_4/4 using 15 equally spaced illumination directions. Field-of-view 64x64 cm ² .	39
34	Magnitude of equivalent Born reconstruction of obj_4/4 using 15 equally spaced illumination directions. Field-of-view 64x64 cm ² .	40
35	One dimensional slice through the center of Figure 34. Length of slice is 64cm.	40
36	Real part of equivalent Born reconstruction of obj_4/2 using 15 equally spaced illumination directions. Field-of-view 64x64 cm ² .	41
37	Imaginary part of equivalent Born reconstruction of obj_4/2 using 15 equally spaced illumination directions. Field-of-view 64x64 cm ² .	41
38	Magnitude of equivalent Born reconstruction of obj_4/2 using 15 equally spaced illumination directions. Field-of-view 64x64 cm ² .	42
39	One dimensional slice through the center of Figure 38. Length of slice is 64cm.	42
40	Real part of equivalent Born reconstruction of obj_2/4 using 15 equally spaced illumination directions. Field-of-view 64x64 cm ² .	43
41	Imaginary part of equivalent Born reconstruction of obj_2/4 using 15 equally spaced illumination directions. Field-of-view 64x64 cm ² .	43

42	Magnitude of equivalent Born reconstruction of obj_2/4 using 15 equally spaced illumination directions. Field-of-view 64x64 cm ² .	44
43	One dimensional slice through the center of Figure 42. Length of slice is 64cm.	44
44	Exact computation of $\left \frac{\mathcal{V}\Psi}{\Psi_i} \right $ for obj_1.1/1.03 at 10 GHz. Inner radius 3.6 cm, outer radius 9.9 cm, Field-of-view 64x64 cm ² .	49
45	Magnitude of the differential cepstrum of $\frac{\mathcal{V}\Psi}{\Psi_i}$ for obj_1.1/1.03.	49
46	Magnitude of the differential cepstrum of \mathcal{V} for obj_1.1/1.03.	50
47	Magnitude of the reconstructed image of \mathcal{V} after low pass filtering in the differential cepstral domain of obj_1.1/1.03. Field-of-view 64x64 cm ² .	50
48	Exact computation of $\left \frac{\mathcal{V}\Psi}{\Psi_i} \right $ for obj_1.03/1.1 at 10 GHz. Inner radius 3.6 cm, outer radius 9.9 cm, Field-of-view 64x64 cm ² .	52
49	Magnitude of the differential cepstrum of $\frac{\mathcal{V}\Psi}{\Psi_i}$ for obj_1.03/1.1.	52
50	Magnitude of the differential cepstrum of \mathcal{V} for obj_1.03/1.1.	53
51	Magnitude of the reconstructed image of \mathcal{V} after low pass filtering in the differential cepstral domain of obj_1.03/1.1. Field-of-view 64x64 cm ² .	53
52	Exact computation of $\left \frac{\mathcal{V}\Psi}{\Psi_i} \right $ for obj_4/4 at 10 GHz. Inner radius 3.6 cm, outer radius 9.9 cm, Field-of-view 64x64 cm ² .	54
53	Magnitude of the differential cepstrum of $\frac{\mathcal{V}\Psi}{\Psi_i}$ for obj_4/4.	54
54	Magnitude of the differential cepstrum of \mathcal{V} for obj_4/4.	55
55	Magnitude of the reconstructed image of \mathcal{V} after low pass filtering in the differential cepstral domain of obj_4/4. Field-of-view 64x64 cm ² .	55
56	Exact computation of $\left \frac{\mathcal{V}\Psi}{\Psi_i} \right $ for obj_4/2 at 10 GHz. Inner radius 3.6 cm, outer radius 9.9 cm, Field-of-view 64x64 cm ² .	56
57	Magnitude of the differential cepstrum of $\frac{\mathcal{V}\Psi}{\Psi_i}$ for obj_4/2.	56
58	Magnitude of the differential cepstrum of \mathcal{V} for obj_4/2.	57
59	Magnitude of the reconstructed image of \mathcal{V} after low pass filtering in the differential cepstral domain of obj_4/2. Field-of-view 64x64 cm ² .	57

60	Exact computation of $\left \frac{V\Psi}{\Psi_i} \right $ for obj_2/4 at 10 GHz. Inner radius 3.6 cm, outer radius 9.9 cm, Field-of-view 64x64 cm ² .	58
61	Magnitude of the differential cepstrum of $\frac{V\Psi}{\Psi_i}$ for obj_2/4.	58
62	Magnitude of the differential cepstrum of V for obj_2/4.	59
63	Magnitude of the reconstructed image of V after low pass filtering in the differential cepstral domain of obj_2/4. Field-of-view 64x64 cm ² .	59
64	Magnitude of single-view backpropagated image $\left(\frac{V\Psi}{\Psi^i} ** h \right)$ for obj_1.1/1.03. Field-of-view 64x64 cm ² .	61
65	Magnitude of the differential cepstrum of $\frac{V\Psi}{\Psi^i} ** h$ for obj_1.1/1.03.	61
66	Magnitude of the reconstructed image of V after low pass filtering in the differential cepstral domain of obj_1.1/1.03. Field-of-view 64x64 cm ² .	62
67	Magnitude of the image in Figure 66 averaged over 15 equally spaced views. Field-of-view 64x64 cm ² .	62
68	Magnitude of single-view backpropagated image $\left(\frac{V\Psi}{\Psi^i} ** h \right)$ for obj_1.03/1.1. Field-of-view 64x64 m ² .	63
69	Magnitude of the differential cepstrum of $\frac{V\Psi}{\Psi^i} ** h$ for obj_1.03/1.1.	63
70	Magnitude of the reconstructed image of V after low pass filtering in the differential cepstral domain of obj_1.03/1.1. Field-of-view 64x64 cm ² .	64
71	Magnitude of the image in Figure 70 averaged over 15 equally spaced views. Field-of-view 64x64 cm ² .	64
72	Magnitude of single-view backpropagated image $\left(\frac{V\Psi}{\Psi^i} ** h \right)$ for obj_4/4. Field-of-view 64x64 cm ² .	65
73	Magnitude of the differential cepstrum of $\frac{V\Psi}{\Psi^i} ** h$ for obj_4/4.	65
74	Magnitude of the reconstructed image of V after low pass filtering in the differential cepstral domain of obj_4/4. Field-of-view 64x64 cm ² .	66
75	Magnitude of the image in Figure 74 averaged over 15 equally spaced views. Field-of-view 64x64 cm ² .	66
76	Magnitude of single-view backpropagated image $\left(\frac{V\Psi}{\Psi^i} ** h \right)$ for obj_4/2. Field-of-view 64x64 cm ² .	67

77	Magnitude of the differential cepstrum of $\frac{V\Psi}{\Psi^i} ** h$ for obj_4/2.	67
78	Magnitude of the reconstructed image of V after low pass filtering in the differential cepstral domain of obj_4/2. Field-of-view 64x64 cm ² .	68
79	Magnitude of the image in Figure 78 averaged over 15 equally spaced views. Field-of-view 64x64 cm ² .	68
80	Magnitude of single-view backpropagated image $\left(\frac{V\Psi}{\Psi^i} ** h\right)$ for obj_2/4. Field-of-view 64x64 cm ² .	69
81	Magnitude of the differential cepstrum of $\frac{V\Psi}{\Psi^i} ** h$ for obj_2/4.	69
82	Magnitude of the reconstructed image of V after low pass filtering in the differential cepstral domain of obj_2/4. Field-of-view 64x64 cm ² .	70
83	Magnitude of the image in Figure 82 averaged over 15 equally spaced views. Field-of-view 64x64 cm ² .	70
84	Magnitude of single-view backpropagated image $\left(\frac{V\Psi}{\Psi^i} ** h\right)$ for obj_1.1/1.03 using <i>a priori</i> knowledge of object support. Field-of-view 64x64 cm ² .	72
85	Magnitude of the differential cepstrum of $\frac{V\Psi}{\Psi^i} ** h$ for obj_1.1/1.03 using <i>a priori</i> knowledge of object support.	72
86	Magnitude of the reconstructed image of V after low pass filtering in the differential cepstral domain of obj_1.1/1.03 (using <i>a priori</i> knowledge of object support). Field-of-view 64x64 cm ² .	73
87	Magnitude of the image in Figure 86 averaged over 15 equally spaced views. Field-of-view 64x64 cm ² .	73
88	Magnitude of single-view backpropagated image $\left(\frac{V\Psi}{\Psi^i} ** h\right)$ for obj_1.03/1.1 using <i>a priori</i> knowledge of object support. Field-of-view 64x64 cm ² .	74
89	Magnitude of the differential cepstrum of $\frac{V\Psi}{\Psi^i} ** h$ for obj_1.03/1.1 using <i>a priori</i> knowledge of object support.	74
90	Magnitude of the reconstructed image of V after low pass filtering in the differential cepstral domain of obj_1.03/1.1 (using <i>a priori</i> knowledge of object support). Field-of-view 64x64 cm ² .	75
91	Magnitude of the image in Figure 90 averaged over 15 equally spaced views. Field-of-view 64x64 cm ² .	75
92	Magnitude of single-view backpropagated image $\left(\frac{V\Psi}{\Psi^i} ** h\right)$ for obj_4/4 using <i>a priori</i> knowledge of object support. Field-of-view 64x64 cm ² .	76

93	Magnitude of the differential cepstrum of $\frac{V\Psi}{\Psi^i} ** h$ for obj_4/4 using <i>a priori</i> knowledge of object support.	76
94	Magnitude of the reconstructed image of V after low pass filtering in the differential cepstral domain of obj_4/4 (using <i>a priori</i> knowledge of object support). Field-of-view $64 \times 64 \text{ cm}^2$.	77
95	Magnitude of the image in Figure 94 averaged over 15 equally spaced views. Field-of-view $64 \times 64 \text{ cm}^2$.	77
96	Magnitude of single-view backpropagated image $\left(\frac{V\Psi}{\Psi^i} ** h\right)$ for obj_4/2 using <i>a priori</i> knowledge of object support. Field-of-view $64 \times 64 \text{ cm}^2$.	78
97	Magnitude of the differential cepstrum of $\frac{V\Psi}{\Psi^i} ** h$ for obj_4/2 using <i>a priori</i> knowledge of object support.	78
98	Magnitude of the reconstructed image of V after low pass filtering in the differential cepstral domain of obj_4/2 (using <i>a priori</i> knowledge of object support). Field-of-view $64 \times 64 \text{ cm}^2$.	79
99	Magnitude of the image in Figure 98 averaged over 15 equally spaced views. Field-of-view $64 \times 64 \text{ cm}^2$.	79
100	Magnitude of single-view backpropagated image $\left(\frac{V\Psi}{\Psi^i} ** h\right)$ for obj_2/4 using <i>a priori</i> knowledge of object support. Field-of-view $64 \times 64 \text{ cm}^2$.	80
101	Magnitude of the differential cepstrum of $\frac{V\Psi}{\Psi^i} ** h$ for obj_2/4 using <i>a priori</i> knowledge of object support.	80
102	Magnitude of the reconstructed image of V after low pass filtering in the differential cepstral domain of obj_2/4 (using <i>a priori</i> knowledge of object support). Field-of-view $64 \times 64 \text{ cm}^2$.	81
103	Magnitude of the image in Figure 102 averaged over 15 equally spaced views. Field-of-view $64 \times 64 \text{ cm}^2$.	81
104	Magnitude of single-view backpropagated image $\left(\frac{V\Psi}{\Psi^i} ** h\right)$ for obj_4/2 with S/N=20 dB. Field-of-view $64 \times 64 \text{ cm}^2$.	82
105	Magnitude of single-view backpropagated image $\left(\frac{V\Psi}{\Psi^i} ** h\right)$ for obj_4/2 with S/N=15 dB. Field-of-view $64 \times 64 \text{ cm}^2$.	82
106	Magnitude of single-view backpropagated image $\left(\frac{V\Psi}{\Psi^i} ** h\right)$ for obj_4/2 with S/N=10 dB. Field-of-view $64 \times 64 \text{ cm}^2$.	83

107	Magnitude of single-view backpropagated image $\left(\frac{V\Psi}{\Psi^i} ** h\right)$ for obj_4/2 with S/N=5 dB. Field-of-view 64x64 cm ² .	83
108	Magnitude of the differential cepstrum of $\frac{V\Psi}{\Psi^i} ** h$ for obj_4/2 using <i>a priori</i> knowledge of object support, S/N=20 dB.	84
109	Magnitude of the reconstructed image of V after low pass filtering in the differential cepstral domain of obj_4/2, with S/N=20 dB (using <i>a priori</i> knowledge of object support). Field-of-view 64x64 cm ² .	84
110	Magnitude of the single-view backpropagated image using bistatic angles 0° to 180° and incident angle 0°. Field-of-view 64x64 cm ² .	87
111	Magnitude of the single-view backpropagated image using bistatic angles 0° to 180° and incident angle 60°. Field-of-view 64x64 cm ² .	87
112	Magnitude of the single-view backpropagated image using bistatic angles 0° to 180° and incident angle 120°. Field-of-view 64x64 cm ² .	88
113	Magnitude of the single-view backpropagated image using bistatic angles 0° to 180° and incident angle 180°. Field-of-view 64x64 cm ² .	88
114	Magnitude of the single-view backpropagated image using bistatic angles 0° to 180° and incident angle 240°. Field-of-view 64x64 cm ² .	89
115	Magnitude of the single-view backpropagated image using bistatic angles 0° to 180° and incident angle 300°. Field-of-view 64x64 cm ² .	89
116	Magnitude of the equivalent Born reconstruction using three views (0°, 60°, 120°). Field-of-view 64x64 cm ² .	90
117	Magnitude of the equivalent Born reconstruction using six views (0°, 60°, 120°, 180°, 240°, 300°). Field-of-view 64x64 cm ² .	90
118	Magnitude of the equivalent Born reconstruction using twelve views (0°, 30°, 60°, 90°, 120°, 150°, 180°, 210°, 240°, 270°, 300°, 330°). Field-of-view 64x64 cm ² .	91
119	Magnitude of the resultant image when the differential cepstral filter is applied to the twelve-view reconstruction. Field-of-view 64x64 cm ² .	91
C.1	Magnitude and Phase (simulated) of the scattered far-field from obj_4/4.125	103
C.2	Magnitude and Phase (simulated) of the scattered far-field from obj_4/2.126	104
C.3	Magnitude and Phase (simulated) of the scattered far-field from obj_2/4.127	105

IMAGE RECONSTRUCTION FROM STRONGLY SCATTERING PENETRABLE OBJECTS USING A DIFFERENTIAL CEPSTRAL FILTER

1. INTRODUCTION

This report describes an attempt to produce quantitative images of penetrable dielectric objects from a limited set of far-field scattered data. The objects considered are strong scatterers, deterministic, and confined to a finite support. A single-frequency plane wave is used to excite polarization currents within the object which, in turn, generate a scattered field that may be collected using a separated receiver (bistatic arrangement). In the regime considered, $k_0 a \approx 1$, where k_0 is the wavenumber of the incident plane wave and a is a characteristic dimension of the inhomogeneity. In this regime, diffraction effects of the wavefield must be accounted for.

Strong scatterers are objects that possess multiple scattering within the object itself. This multiple scattering complicates our knowledge of the internal fields, making the direct problem of computing the scattered field a difficult one. We backpropagate scattered fields from both simulated and measured data and show how the image relates to the desired permittivity distribution times the total field. The problem here is that the backpropagated image is disrupted by this unwanted multiplicative field factor that cannot be removed through conventional linear filtering. We exploit a nonlinear filtering technique known as differential cepstral filtering to isolate the desired permittivity distribution from the perturbed backpropagated image of strongly scattering objects. In principle, quantitative information on the object's permittivity profile can be obtained through a properly calibrated routine.

This work contrasts with well developed x-ray tomographic techniques [Mueller, et al, 1979] that use high energy ($k_0 a \gg 1$), non-diffracting radiation to produce images. X-rays propagate in essentially straight lines so that ray theory may be used to project the object's attenuation profile onto an array of detectors. The Fourier transform of these "projections" maps onto slices of the two-dimensional Fourier transform of the object (Fourier-slice theorem).

Multiple views are then used to "fill up" Fourier space and images may be reconstructed (after interpolation) by Fourier inversion [Pan, et al, 1983].

Wolf [1969] was the first to show scattered field data mapped onto spectral components of the scattering potential for weakly scattering objects. The scattering potential is defined as $k_0^2(n^2(\mathbf{r}) - 1)$ for a free space background, where $n(\mathbf{r})$ is the object's refractive index. By allowing both the transmitter and receiver to vary over $[0, 2\pi]$ in a bistatic radar configuration, Fourier data are collected for those spatial frequencies less than $|2k_0|$. Image reconstruction by Fourier inversion provides a low-pass reconstruction of the scattering potential.

Weakly scattering approximations such as the first Born approximation (BA) and Rytov approximation (RA) linearize the integral equation of scattering, allowing a tractable solution to the scattering potential in diffraction tomography ($k_0a \approx 1$ or $k_0a \ll 1$). Devaney [1982] introduced a filtered backpropagation algorithm analogous to the filtered backprojection algorithm used in transmission tomography. The algorithm operates in the spatial domain and accumulates images from many different illumination directions one at a time. This process is equivalent to Fourier reconstruction; however, interpolation onto rectangular grids (as in Fourier domain reconstruction) is no longer necessary. Merits of the spatial and frequency domain approaches have been compared in Pan, et al, [1983].

Since the classic paper by Wolf [1969], the BA and the RA have been exploited considerably in diffraction tomography. Each approximation involves very different assumptions, and therefore the domains of validity must be considered in any application [Fiddy, 1986], [Lin, et al, 1990]. The BA requires that the phase delay introduced by the object's presence be much less than one radian compared to the phase of an undisturbed wave [Slaney, et al, 1984]. In contrast, the RA requires that the change in refractive index with respect to distance be small, with no restriction placed on the object's size [Tatarski, 1961].

In Section 2, we review the scalar Green's function approach to compute the exact scattered field from a 2D inhomogeneous region. In Sections 3 and 4, we discuss the weakly scattering Born and Rytov approximations, respectively. These approximations have been used extensively in media characterization during the last 30 years.

In Sections 5 and 6, we review the exact computation of the scattered field from homogeneous cylinders and two concentric cylinders, respectively. Cylinders are the only practical 2D objects for which exact solutions to the scattered fields exist. The scattered fields are used to generate simulated data for the differential cepstral processing. Plots of the total field magnitude in the proximity of various cylinders (under plane wave illumination) are shown to demonstrate how strong scatterers perturb the incident field.

In Section 7, we exploit an alternative interpretation of the Born approximation, introduced by Slaney, et al, [1984], that allows one to define an "effective scattering potential" as a product of the scattering potential and the total field. Single-view images of the effective scattering potential are formulated in terms of the backpropagation algorithm.

In Section 8, multi-view images are generated for several strongly scattering concentric cylinders, showing the failure of the Born approximation with such objects. Then, in Section 9, a

differential cepstral filtering technique is introduced to isolate the scattering potential from single-view backpropagated images of the effective scattering potential.

In Sections 10, 11, and 12 the differential filtering technique is demonstrated on exact $V \frac{\Psi}{\Psi^i}$, single-view backpropagated $V \frac{\Psi}{\Psi^i}$, and single-view backpropagated $V \frac{\Psi}{\Psi^i}$ using *a priori* knowledge of the object support, respectively, where V is the scattering potential, Ψ is the total field, and Ψ^i is the incident field. Also, in Section 12, the effects of noise on the backpropagated image and differential cepstral filtering technique are examined. In Section 13, the differential cepstral filtering technique is applied to measured data from a square dielectric cylinder at 10 GHz. Finally, conclusions and recommendations are considered in Sections 14 and 15, respectively.

2. SCATTERED FIELD IN A TWO DIMENSIONAL INHOMOGENEOUS REGION

In this section, we consider transverse magnetic (TM) scattering from an inhomogeneous object under plane wave illumination. The incident transverse electromagnetic (TEM) wave has a z component parallel to the non-varying z axis of the object. The z component of the incident field $E_z^i(x, y)e^{-i\omega t}$ satisfies the scalar wave equation

$$\frac{\partial^2}{\partial x^2}[E_z^i(x, y)e^{-i\omega t}] + \frac{\partial^2}{\partial y^2}[E_z^i(x, y)e^{-i\omega t}] = \frac{1}{c^2} \frac{\partial^2}{\partial t^2}[E_z^i(x, y)e^{-i\omega t}] \quad (2.1)$$

where c is the speed of light in a vacuum. Equation (2.1) reduces to the Helmholtz equation

$$\left[\frac{\partial^2}{\partial x^2} + \frac{\partial^2}{\partial y^2} + k_0^2 \right] E_z^i(x, y) = 0 \quad (2.2)$$

where $k_0 = \omega / c$ is the free space wave number, ω is the radian frequency, and the quantity in brackets operates on $E_z^i(x, y)$. The time dependence $e^{-i\omega t}$ has been omitted for brevity.

The total field is defined to be

$$E_z(x, y) = E_z^i(x, y) + E_z^s(x, y) \quad (2.3)$$

where $E_z^i(x, y)$ and $E_z^s(x, y)$ are the incident and scattered field respectively.

When inhomogeneities confined to a finite support D [Lin, et al, 1990] are considered, Eq. (2.2) must be modified to account for the wave number change within the medium. The wave number inside D becomes $k(x, y) = \omega \sqrt{\mu(x, y)\epsilon(x, y)}$ where $\mu(x, y)$ and $\epsilon(x, y)$ are the

permeability and permittivity of the medium, respectively. Consider a lossless object with relative permittivity $\epsilon_r(x, y)$ and relative permeability $\mu_r(x, y) = 1$. In this case, $k^2(x, y)$ equals $k_0^2 \epsilon_r(x, y)$. The total field within the inhomogeneous region must satisfy the Helmholtz equation

$$\left[\frac{\partial^2}{\partial x^2} + \frac{\partial^2}{\partial y^2} + k_0^2 \epsilon_r(x, y) \right] E_z(x, y) = 0. \quad (2.4)$$

We define a scattering potential $V(x, y) = [\epsilon_r(x, y) - 1]$ to be the change in relative permittivity with respect to the surrounding medium (free space in this case). This quantity describes the inhomogeneities within the object and directly relates to Wolf's [1969] definition

$k_0^2 [\epsilon_r(x, y) - 1]$. Using Eqs. (2.2), (2.3) and $V(x, y)$, it is easy to show that the scattered field satisfies the differential equation

$$\left[\frac{\partial^2}{\partial x^2} + \frac{\partial^2}{\partial y^2} + k_0^2 \right] E_z^s(x, y) = -k_0^2 V(x, y) E_z(x, y). \quad (2.5)$$

The non-zero forcing term on the right hand side of Eq. (2.5) resembles the mathematical formulation that results from wave propagation in a region containing sources. We may interpret the forcing term as an equivalent polarization current [Pichot, et al, 1985] giving rise to the scattered field $E_z^s(x, y)$.

The first step in a Green's function solution to the second-order, non-homogeneous differential equation in Eq. (2.5) is to find a $G(x, y, x', y')$ that satisfies

$$\left[\frac{\partial^2}{\partial x^2} + \frac{\partial^2}{\partial y^2} + k_0^2 \right] G(x, y, x', y') = -\delta(x - x', y - y'). \quad (2.6)$$

The solution to Eq. (2.6) that represents an outward traveling wave is: [Morita, et al, 1990, p.18]

$$G(\mathbf{r}, \mathbf{r}') = -\frac{i}{4} H_0^{(1)}(k_0 |\mathbf{r} - \mathbf{r}'|), \quad (2.7)$$

where $\mathbf{r} = x\hat{x} + y\hat{y}$, $\mathbf{r}' = x'\hat{x} + y'\hat{y}$, and $H_0^{(1)}(k_0 |\mathbf{r} - \mathbf{r}'|)$ is a zero-order Hankel function of the first kind. Since the Laplacian operator is a linear operator, the final step to the solution of Eq. (2.5) is the superposition of the weighted forcing term. The scattered field from an inhomogeneous region in two dimensions becomes

$$E_z^s(\mathbf{r}) = -i \frac{k_0^2}{4} \int_D V(\mathbf{r}') E_z(\mathbf{r}') H_0^{(1)}(k_0 |\mathbf{r} - \mathbf{r}'|) d\mathbf{r}' . \quad (2.8)$$

According to Eq. (2.3), the total z component of the electric field is found from the following integral equation for scattering:

$$E_z(\mathbf{r}) = E_z^i(\mathbf{r}) - i \frac{k_0^2}{4} \int_D V(\mathbf{r}') E_z(\mathbf{r}') H_0^{(1)}(k_0 |\mathbf{r} - \mathbf{r}'|) d\mathbf{r}' . \quad (2.9)$$

Equation (2.9) is an inhomogeneous Fredholm integral equation of the first kind [Morse and Feshbach, 1953, p. 904] and also a Lippmann-Schwinger [Caorsi, et al, 1990] integral equation. This equation is difficult to solve since the desired quantity $E_z(\mathbf{r})$ appears under the integral sign.

The above analysis, could have been applied equally well to any other non-zero field component, H_x or H_y . However, only one component is necessary, namely E_z , since

Maxwell's equation $\nabla \times \mathbf{E} = -i\omega\mu\mathbf{H}$ provides the other two: $H_x(\mathbf{r}) = \frac{1}{-i\omega\mu} \frac{\partial}{\partial y} E_z(\mathbf{r})$ and

$$H_y(\mathbf{r}) = \frac{1}{i\omega\mu} \frac{\partial}{\partial x} E_z(\mathbf{r}) .$$

3. BORN APPROXIMATION

Let $\Psi(\mathbf{r})$, $\Psi^i(\mathbf{r})$, and $\Psi^s(\mathbf{r})$ represent the total, incident and scattered field of either the electric or magnetic disturbance, respectively. Then the integral equation for scattering according to Eq. (2.9) is

$$\Psi(\mathbf{r}) = \Psi^i(\mathbf{r}) - i \frac{k_0^2}{4} \int_D V(\mathbf{r}') \Psi(\mathbf{r}') H_0^{(1)}(k_0 |\mathbf{r} - \mathbf{r}'|) d\mathbf{r}' . \quad (3.1)$$

Using the method of successive approximations [Morse and Feshbach, 1953, Part II] the total field in Eq. (3.1) is written [Fiddy, 1986]

$$\Psi(\mathbf{r}) = \Psi^i(\mathbf{r}) + \Psi_1(\mathbf{r}) + \Psi_2(\mathbf{r}) + \Psi_3(\mathbf{r}) + \dots \quad (3.2)$$

where

$$\Psi_1(\mathbf{r}) = -i \frac{k_0^2}{4} \int_D V(\mathbf{r}') \Psi^i(\mathbf{r}') H_0^{(1)}(k_0 |\mathbf{r} - \mathbf{r}'|) d\mathbf{r}'$$

and

$$\Psi_n(\mathbf{r}) = -i \frac{k_0^2}{4} \int_D V(\mathbf{r}') \Psi_{n-1}(\mathbf{r}') H_0^{(1)}(k_0 |\mathbf{r} - \mathbf{r}'|) d\mathbf{r}' \quad \text{for } n = 2, 3, 4, \dots$$

The scattered field can be written as:

$$\Psi^s(\mathbf{r}) = \sum_{n=1}^N \Psi_n(\mathbf{r}). \quad (3.3)$$

Convergence proofs of the iterative solution given in Eq. (3.2) are difficult to produce and are rarely available [Butkov, 1968, p. 648]; the technique of using higher order approximations ($n > 1$) to the scattered field is not a mature one [Slaney, et al, 1984].

Under weak scattering conditions, such that $|\Psi^s(\mathbf{r})| \ll |\Psi^i(\mathbf{r})|$, it is common to adopt the first Born approximation by using $N = 1$ in Eq. (3.3) to represent the scattered field. The first Born approximation can also be derived using the method of small perturbations to the solution of the wave equation [Tartarski, 1961, p. 122]. The scattered field in the first Born approximation becomes

$$\Psi_{BA}^s(\mathbf{r}) = -i \frac{k_0^2}{4} \int_D V(\mathbf{r}') \Psi^i(\mathbf{r}') H_0^{(1)}(k_0 |\mathbf{r} - \mathbf{r}'|) d\mathbf{r}'. \quad (3.4)$$

Physically, we interpret the object $V(\mathbf{r})$ in Eq. (3.4) as being excited by the incident field $\Psi^i(\mathbf{r})$, the field that would be present if the object were nonexistent. As the scattering potential $V(\mathbf{r})$ increases, the "equivalent excitation" $V(\mathbf{r})\Psi^i(\mathbf{r})$, shown in Eq. (3.1) becomes more complex due to multiple scattering and less similar to $V(\mathbf{r})\Psi^i(\mathbf{r})$ shown in Eq. (3.4). The first Born approximation for the scattered field fails for such objects.

The first Born approximation works well for those cases where the relative change in electrical length through the object is much smaller than one radian [Ishimaru, 1991, p. 492]. Mathematically, this is written

$$|k_0 a - k a| \ll 1 \quad (3.5)$$

where a is the maximum dimension of the object. Equation (3.5) can easily be written in terms of the refractive index n as $|k_0(1-n)a| \ll 1$ or the relative permittivity as $|k_0(1-\sqrt{\epsilon_r})a| \ll 1$.

In practice, researchers have successfully used $|k_0(1-n)a| < \frac{\pi}{2}$ [Slaney, et al, 1984] and $|k_0(1-n)a| < 2$ [Fiddy, 1986] as less stringent criteria than Eq. (3.5).

4. RYTOV APPROXIMATION

Like the Born approximation, the Rytov approximation is another method used to linearize the integral equation of scattering, thus providing an equation that is solvable [Ishimaru, 1991, p. 623]. However, as we shall see, the domains of validity of the two approximations are different.

The Rytov approximation is based on the substitution:

$$\Psi(x, y) \equiv e^{\phi(x, y)} = e^{\phi^i(x, y) + \phi^s(x, y)}. \quad (4.1)$$

According to Eq. (2.5), the wave equation for an arbitrary field component $\Psi(x, y)$ in an inhomogeneous region is given by

$$[\nabla^2 + k_0^2]e^{\phi(x, y)} = -k_0^2 V(x, y)e^{\phi(x, y)}. \quad (4.2)$$

When inhomogeneities are not present $V(x, y) = 0$, and we have

$$[\nabla^2 + k_0^2]e^{\phi^i(x, y)} = 0. \quad (4.3)$$

It is straightforward to show that Eqs. (4.2) and (4.3) can be reduced to the following two Riccati equations, respectively,

$$\nabla^2 \phi(x, y) + \nabla \phi(x, y) \cdot \nabla \phi(x, y) + k_0^2 [1 + V(x, y)] = 0 \quad (4.4)$$

and

$$\nabla^2 \phi^i(x, y) + \nabla \phi^i(x, y) \cdot \nabla \phi^i(x, y) + k_0^2 = 0. \quad (4.5)$$

Subtracting Eq. (4.5) from Eq. (4.4) (recall that $\phi(x, y) = \phi^i(x, y) + \phi^s(x, y)$) gives

$$\nabla^2 \phi^s(x, y) + [\nabla \phi(x, y) \cdot \nabla \phi(x, y) - \nabla \phi^i(x, y) \cdot \nabla \phi^i(x, y)] + k_0^2 V(x, y) = 0. \quad (4.6)$$

The term in brackets in Eq. (4.6) can be written (omitting the arguments) as

$$\begin{aligned} \nabla \phi \cdot \nabla \phi - \nabla \phi^i \cdot \nabla \phi^i &= \nabla(\phi^i + \phi^s) \cdot \nabla(\phi^i + \phi^s) - \nabla \phi^i \cdot \nabla \phi^i \\ &= 2\nabla \phi^s \cdot \nabla \phi^i + \nabla \phi^s \cdot \nabla \phi^s. \end{aligned} \quad (4.7)$$

Using Eq. (4.7) in Eq. (4.6), we write

$$\nabla^2 \phi^s + 2\nabla \phi^s \cdot \nabla \phi^i = -\nabla \phi^s \cdot \nabla \phi^s - k_0^2 V. \quad (4.8)$$

Now, solving for the last two terms in the identity [Ishimaru, 1991, p. 623]

$$\nabla^2 [e^{\phi^i} \phi^s] = (\nabla^2 e^{\phi^i}) \phi^s + 2e^{\phi^i} \nabla \phi^i \cdot \nabla \phi^s + e^{\phi^i} \nabla^2 \phi^s \quad (4.9)$$

we find that

$$2e^{\phi^i} \nabla \phi^s \cdot \nabla \phi^i + e^{\phi^i} \nabla^2 \phi^s = \nabla^2 [e^{\phi^i} \phi^s] + k_0^2 e^{\phi^i} \phi^s. \quad (4.10)$$

Note that it is easy to show $\nabla^2 e^{\phi^i} = -k_0^2 e^{\phi^i}$, since $e^{\phi^i(\mathbf{r})}$ is the incident field $e^{ik_0 \hat{\mathbf{r}}_i \cdot \mathbf{r}}$. Equation (4.10) can be written as

$$\nabla^2 \phi^s + 2\nabla \phi^s \cdot \nabla \phi^i = \frac{1}{e^{\phi^i}} \left[\nabla^2 [e^{\phi^i} \phi^s] + k_0^2 e^{\phi^i} \phi^s \right]. \quad (4.11)$$

Substituting Eq. (4.11) into the left-hand side of Eq. (4.8) and rearranging, we find a non-homogeneous differential equation resembling the form of Eq. (2.5) (arguments are now included)

$$[\nabla^2 + k_0^2] e^{\phi^i(\mathbf{r})} \phi^s(\mathbf{r}) = e^{\phi^i(\mathbf{r})} [-\nabla \phi^s(\mathbf{r}) \cdot \nabla \phi^s(\mathbf{r}) - k_0^2 V(\mathbf{r})]. \quad (4.12)$$

We may neglect the term $\nabla \phi^s(\mathbf{r}) \cdot \nabla \phi^s(\mathbf{r})$ for those cases where $|\nabla \phi^s(\mathbf{r})| \ll |\nabla \phi^i(\mathbf{r})|$ [Tatarski, 1961, p. 125]. This implies that $|\nabla \phi^s(\mathbf{r})| \ll \frac{2\pi}{\lambda}$ since $|\nabla \phi^i(\mathbf{r})| = |\nabla (ik_0 \hat{\mathbf{r}}_i \cdot \mathbf{r})| = k_0$.

Physically, $\nabla \phi^s(\mathbf{r})$ cannot change quickly over the distance of a wavelength - the scale at which $V(\mathbf{r})$ fluctuates should be larger than the wavelength for the Rytov approximation to be valid.

Using Rytov's approximation, Eq. (4.12) is written

$$[\nabla^2 + k_0^2] e^{\phi^i(\mathbf{r})} \phi^s(\mathbf{r}) = -k_0^2 V(\mathbf{r}) e^{\phi^i(\mathbf{r})}. \quad (4.13)$$

According to the Green's function solution (Eq. (2.7)), Rytov's first approximation to the unknown phase $\phi^s(\mathbf{r})$ is

$$\phi^s(\mathbf{r}) = -\frac{ik_0^2}{4} \frac{1}{e^{\phi^i(\mathbf{r})}} \int_D e^{\phi^i(\mathbf{r}')} V(\mathbf{r}') H_0^{(1)}(k_0|\mathbf{r} - \mathbf{r}'|) d\mathbf{r}'. \quad (4.14)$$

In Eq. (4.14), we recognize the integral as the first Born approximation to the scattered field, and, using Eq. (3.4), one can show the following relationship

$$\phi^s(\mathbf{r}) = \frac{\Psi_{BA}^s(\mathbf{r})}{e^{\phi^i(\mathbf{r})}}. \quad (4.15)$$

Although there is a simple relationship between the first Born approximation to the scattered field and Rytov's approximation to the scattered phase, the domains of validity of the two approximations are quite different [Devaney, 1981], [Lin, et al, 1992]. The Born approximation requires that the phase delay introduced by the object's presence be much less than one radian compared to the phase of an undisturbed wave. In contrast, the Rytov approximation requires that the change in refractive index with respect to distance be small on the scale of the wavelength, with no restriction placed on the object's size.

5. FAR-FIELD TRANSVERSE MAGNETIC (TM) SCATTERING FROM A CIRCULAR CYLINDER

In Section 2, we considered scattering from a nonhomogeneous region and showed how the integral equation of scattering (2.9) was developed. In general, it is difficult to solve Eq. (2.9) for the scattered field since the scattered field is also contained within the integral. Exact solutions to the scattered field from any object would be beneficial in providing input data to inversion algorithms. In this section, we summarize the procedure for obtaining the scattered field from a circular cylinder under plane wave illumination for which an exact solution does exist [Ishimaru, 1991], [Ruck, 1970], [Jones, 1964]. In Section 9, we use the scattered field data as input to our image reconstruction algorithm.

Consider a circular dielectric cylinder with radius a and wavenumber k_a , as shown in Figure 1, illuminated by the plane wave $\Psi^i(x, y) = e^{ik_0 \hat{\mathbf{r}}_i \cdot \mathbf{r}}$. Assume that the wave travels in the $\hat{\mathbf{r}}_i = -\hat{x}$ direction. The total field in each region is a linear combination of cylindrical wave eigenfunctions and is described by the following equations [Harrington, 1961, p. 233] ($e^{-i\omega t}$ time convention assumed)

$$\Psi(\rho, \phi) = \sum_{n=-\infty}^{\infty} (-i)^n [J_n(k_0 \rho) + a_n H_n^{(1)}(k_0 \rho)] e^{in\phi} \quad \text{for } \rho > a \quad (5.1)$$

and

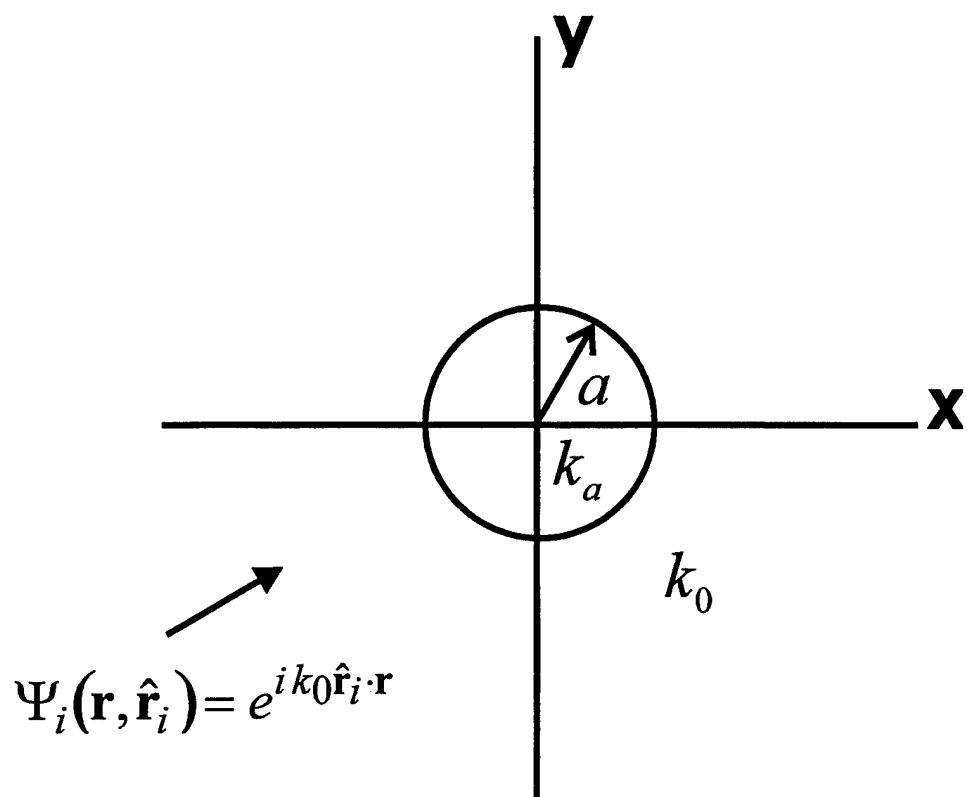


Figure 1 Cross section of homogeneous dielectric cylinder of radius a .

$$\Psi_a(\rho, \phi) = \sum_{n=-\infty}^{\infty} (-i)^n [c_n J_n(k_a \rho)] e^{in\phi} \quad \text{for } \rho \leq a. \quad (5.2)$$

The first term in Eq. (5.1) represents a wave transformation [Harrington, 1961, p. 230] of the incident field $e^{-ik_0 x}$ and the second term represents outward traveling waves. In Eq. (5.2), Bessel functions of the first kind are used so that the field remains finite at $\rho = 0$. The unknown coefficients a_n and c_n are found by applying the appropriate boundary conditions.

Continuity of the electric and magnetic fields at the boundary implies that the field and its normal derivative are continuous at the boundary. Continuity of the fields, $\Psi(\rho, \phi) = \Psi_a(\rho, \phi)$, at $\rho = a$ yields

$$a_n = \frac{c_n J_n(k_a a) - J_n(k_0 a)}{H_n^{(1)}(k_0 a)} \quad (5.3)$$

and continuity of the normal derivative, $\frac{\delta}{\delta \rho} \Psi(\rho, \phi) = \frac{\delta}{\delta \rho} \Psi_a(\rho, \phi)$, at $\rho = a$ yields

$$c_n = \frac{k_0}{k_a} \left[\frac{J_n'(k_0 a) + a_n H_n^{(1)'}(k_0 a)}{J_n'(k_a a)} \right], \quad (5.4)$$

where the prime denotes a derivative with respect to ρ . The simultaneous solution for c_n from Eqs. (5.3) and (5.4) gives

$$c_n = - \frac{k_a J_n(k_0 a) J_n'(k_a a) + k_0 J_n'(k_0 a) J_n(k_a a)}{k_a H_n^{(1)}(k_0 a) J_n'(k_a a) - k_0 H_n^{(1)'}(k_0 a) J_n(k_a a)}. \quad (5.5)$$

Using $J_{-n}(z) = (-1)^n J_n(z)$ and $(e^{i\phi} + e^{-i\phi})/2 = \cos \phi$, we recognize that $c_n = c_{-n}$ [McGahan, 1992]. Therefore the total field in each region can be written

$$\Psi(\rho, \phi) = \sum_{n=0}^{\infty} (-i)^n \varepsilon_n [J_n(k_0 \rho) + a_n H_n^{(1)}(k_0 \rho)] \cos(n\phi) \quad \text{for } \rho > a \quad (5.6)$$

and

$$\Psi_a(\rho, \phi) = \sum_{n=0}^{\infty} (-i)^n \varepsilon_n [c_n J_n(k_a \rho)] \cos(n\phi) \quad \text{for } \rho \leq a, \quad (5.7)$$

where

$$\varepsilon_n \equiv \begin{cases} 2 & n = 0 \\ 1 & n = 1, 2, 3, \dots \end{cases}$$

and c_n and a_n are given in Eqs. (5.5) and (5.3), respectively. Note that for $\rho > a$, numerical computation of the total field converges much faster when the incident field is replaced by its simpler form

$$\Psi(\rho, \phi) = e^{-ik_0 x} + \sum_{n=0}^{\infty} (-i)^n \varepsilon_n a_n H_n^{(1)}(k_0 \rho) \cos(n\phi) \quad \text{for } \rho > a. \quad (5.8)$$

The second term in Eq. (5.8) represents the scattered field and may be used as input to the inversion algorithm described in Section 7.

Equations (5.7) and (5.8) are used to calculate the total field at 10 GHz in the interior and exterior regions of several homogeneous cylinders of radius 4.25 cm under plane wave illumination. Figures 2-11 show the magnitude of the total field for relative permittivities between 1.01 and 10.0 with the field incident from the top of the page.

The gray scale range is held constant for each plot in all figures so that the field magnitudes are relative. Consequently, the perturbation in total field due to the cylinder with relative permittivity 1.01 as shown in Figure 2 is undetectable. As the relative permittivity increases, focusing effects and shadow regions can be identified in the figures. Also, the diameter of the cylinder becomes more clearly defined.

According to the criterion established in Section 3, the Born approximation, in these examples, is violated for $\varepsilon_r > 1.2$.

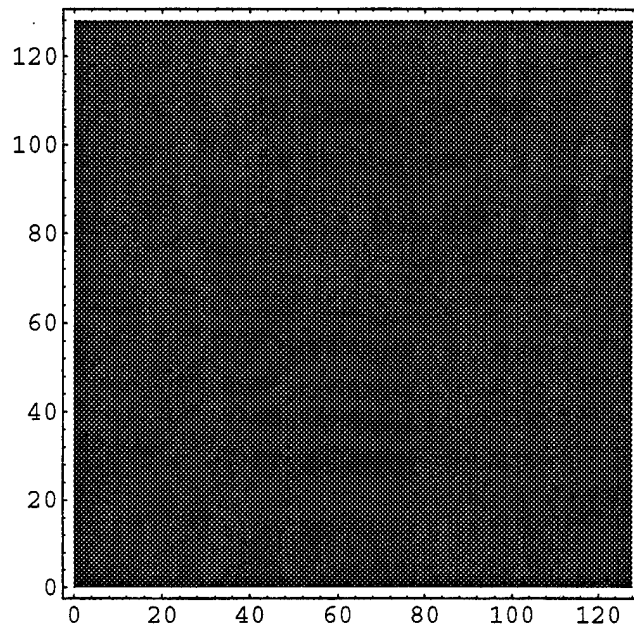


Figure 2 Total field intensity internal and external to a homogeneous dielectric cylinder of radius 0.0425 m and relative permittivity $\epsilon_r = 1.0$ under plane wave illumination at 10 GHz. Field-of-view is 0.1984 m on each side.

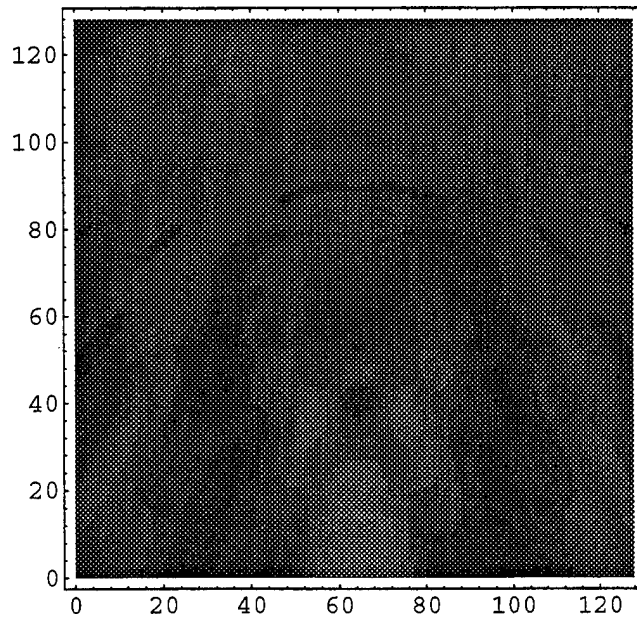


Figure 3 Total field intensity internal and external to a homogeneous dielectric cylinder of radius 0.0425 m and relative permittivity $\epsilon_r = 1.1$ under plane wave illumination at 10 GHz. Field-of-view is 0.1984 m on each side.

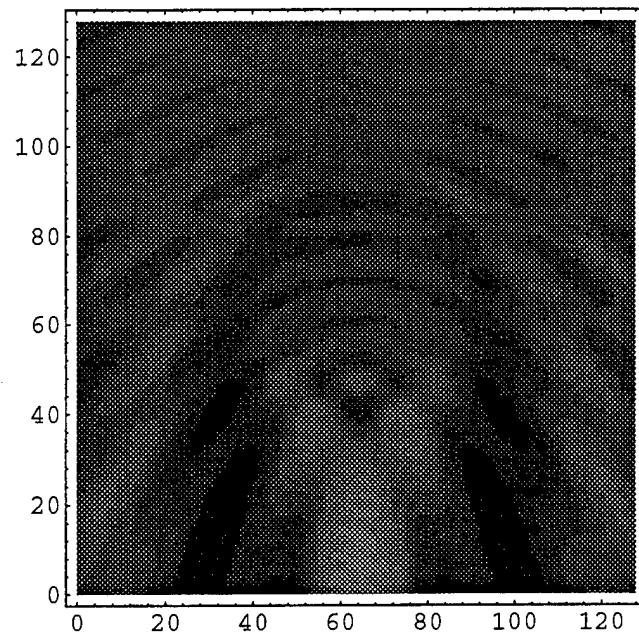


Figure 4 Total field intensity internal and external to a homogeneous dielectric cylinder of radius 0.0425 m and relative permittivity $\epsilon_r = 1.2$ under plane wave illumination at 10 GHz. Field-of-view is 0.1984 m on each side.

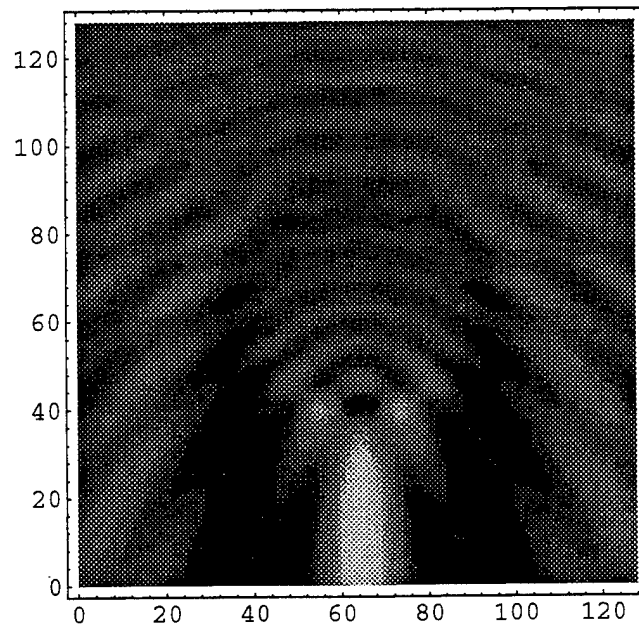


Figure 5 Total field intensity internal and external to a homogeneous dielectric cylinder of radius 0.0425 m and relative permittivity $\epsilon_r = 1.4$ under plane wave illumination at 10 GHz. Field-of-view is 0.1984 m on each side.

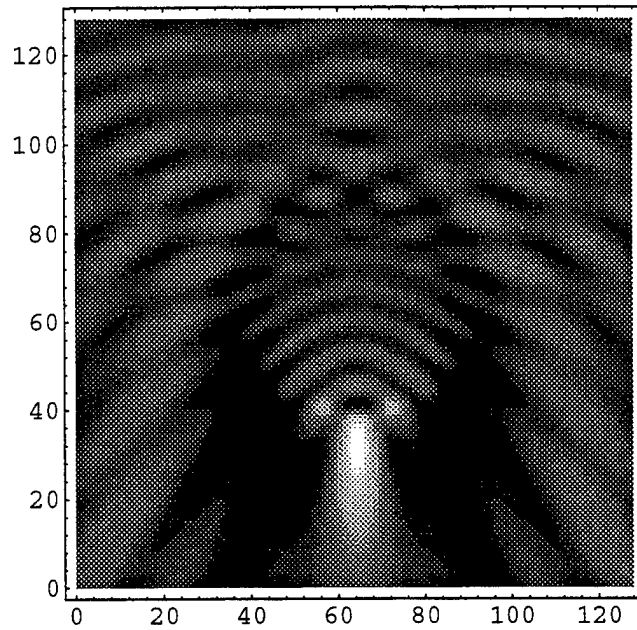


Figure 6 Total field intensity internal and external to a homogeneous dielectric cylinder of radius 0.0425 m and relative permittivity $\epsilon_r = 1.8$ under plane wave illumination at 10 GHz. Field-of-view is 0.1984 m on each side.

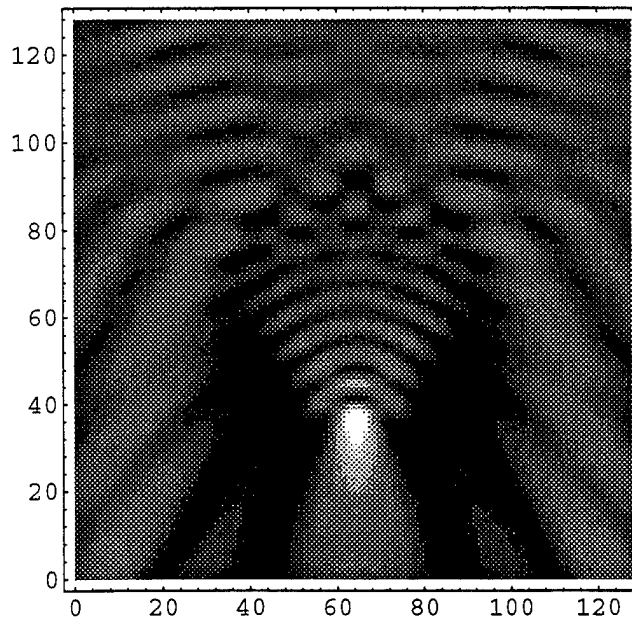


Figure 7 Total field intensity internal and external to a homogeneous dielectric cylinder of radius 0.0425 m and relative permittivity $\epsilon_r = 2.2$ under plane wave illumination at 10 GHz. Field-of-view is 0.1984 m on each side.

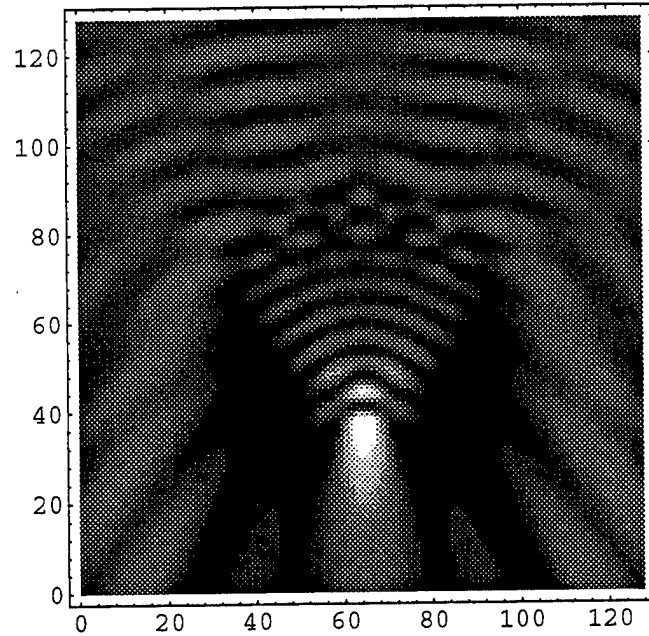


Figure 8 Total field intensity internal and external to a homogeneous dielectric cylinder of radius 0.0425 m and relative permittivity $\epsilon_r = 2.56$ under plane wave illumination at 10 GHz. Field-of-view is 0.1984 m on each side.

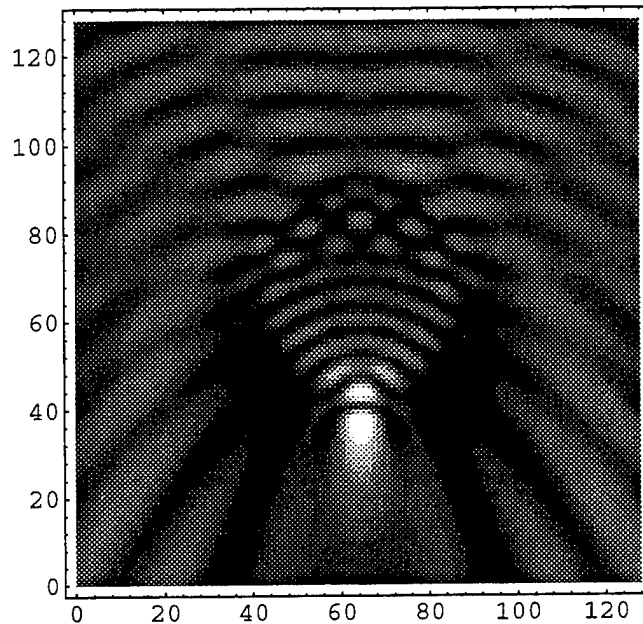


Figure 9 Total field intensity internal and external to a homogeneous dielectric cylinder of radius 0.0425 m and relative permittivity $\epsilon_r = 3.0$ under plane wave illumination at 10 GHz. Field-of-view is 0.1984 m on each side.

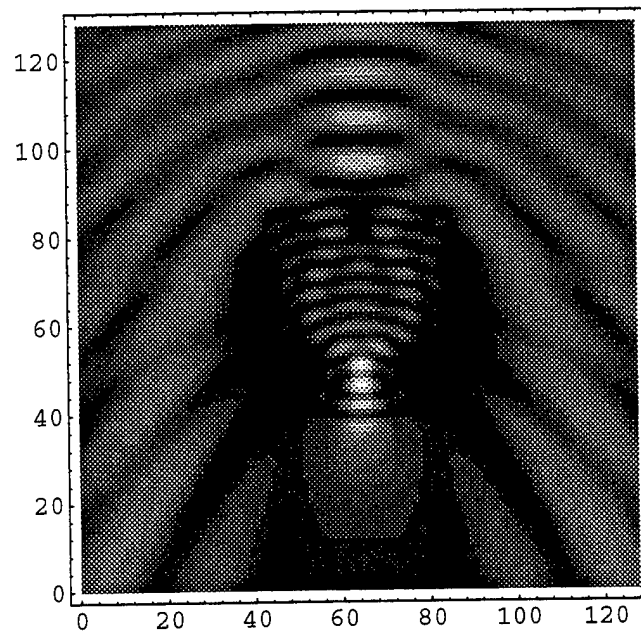


Figure 10 Total field intensity internal and external to a homogeneous dielectric cylinder of radius 0.0425 m and relative permittivity $\epsilon_r = 5.0$ under plane wave illumination at 10 GHz. Field-of-view is 0.1984 m on each side.

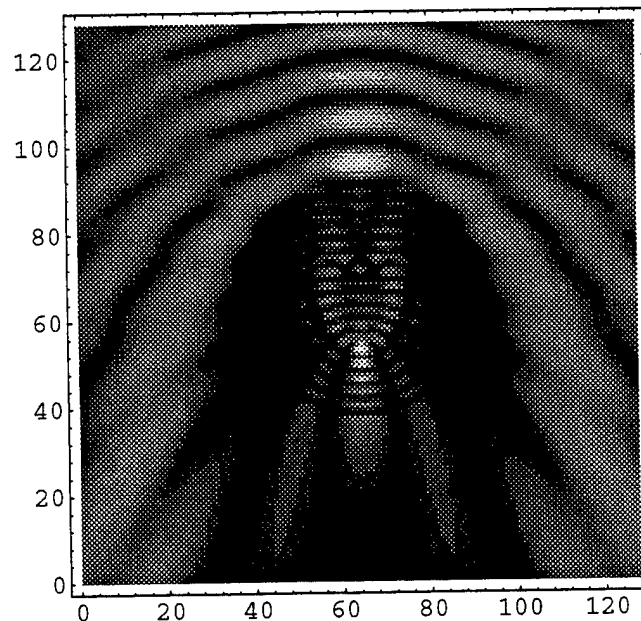


Figure 11 Total field intensity internal and external to a homogeneous dielectric cylinder of radius 0.0425 m and relative permittivity $\epsilon_r = 10.0$ under plane wave illumination at 10 GHz. Field-of-view is 0.1984 m on each side.

6. FAR-FIELD TRANSVERSE MAGNETIC (TM) SCATTERING FROM TWO CONCENTRIC CYLINDERS

In this section, the procedure for obtaining the scattered field from two concentric circular cylinders under plane wave illumination for which an exact solution does exist is summarized [Tang, 1957], [Ruck, 1970]. Later, we use this scattered field data as input to our image reconstruction algorithm.

Consider a cross section of two concentric cylinders with inner radius a and outer radius b with respective wavenumbers as shown in Figure 12. The field in each region is a linear combination of cylindrical wave eigenfunctions and is described by the equations

$$\Psi(\rho, \phi) = \sum_{n=-\infty}^{\infty} (-i)^n [J_n(k_0 \rho) + a_n H_n^{(1)}(k_0 \rho)] e^{in\phi} \quad \text{for } \rho > b \quad (6.1)$$

$$\Psi_b(\rho, \phi) = \sum_{n=-\infty}^{\infty} (-i)^n [b_n H_n^{(2)}(k_b \rho) + c_n H_n^{(1)}(k_b \rho)] e^{in\phi} \quad \text{for } a < \rho \leq b \quad (6.2)$$

and

$$\Psi_a(\rho, \phi) = \sum_{n=-\infty}^{\infty} (-i)^n [d_n J_n(k_a \rho)] e^{in\phi} \quad \text{for } \rho \leq a. \quad (6.3)$$

The first term in Eq. (6.1) represents a wave transformation of the incident field $e^{-ik_0 x}$ and the second term represents outward traveling waves. Equation (6.2) combines outgoing $H_n^{(1)}$ and incoming $H_n^{(2)}$ cylindrical waves (recall that an $e^{-i\omega t}$ time convention is assumed). Bessel functions of the first kind are used in Eq. (6.3) so that the field remains finite at $\rho = 0$. The unknown coefficients a_n, b_n, c_n , and d_n are found by applying appropriate boundary conditions.

Continuity of the fields at $\rho = a$ and $\rho = b$ gives

$$b_n H_n^{(2)}(k_b a) + c_n H_n^{(1)}(k_b a) = d_n J_n(k_a a) \quad (6.4)$$

and

$$J_n(k_0 b) + a_n H_n^{(1)}(k_0 b) = b_n H_n^{(2)}(k_b b) + c_n H_n^{(1)}(k_b b). \quad (6.5)$$

Continuity of the normal derivatives of the fields at $\rho = a$ and $\rho = b$ gives

$$k_b b_n H_n^{(2)'}(k_b a) + k_b c_n H_n^{(1)'}(k_b a) = k_a d_n J_n'(k_a a) \quad (6.6)$$

and

$$k_0 J_n'(k_0 b) + k_0 a_n H_n^{(1)'}(k_0 b) = k_b b_n H_n^{(2)'}(k_b b) + k_b c_n H_n^{(1)'}(k_b b) \quad (6.7)$$

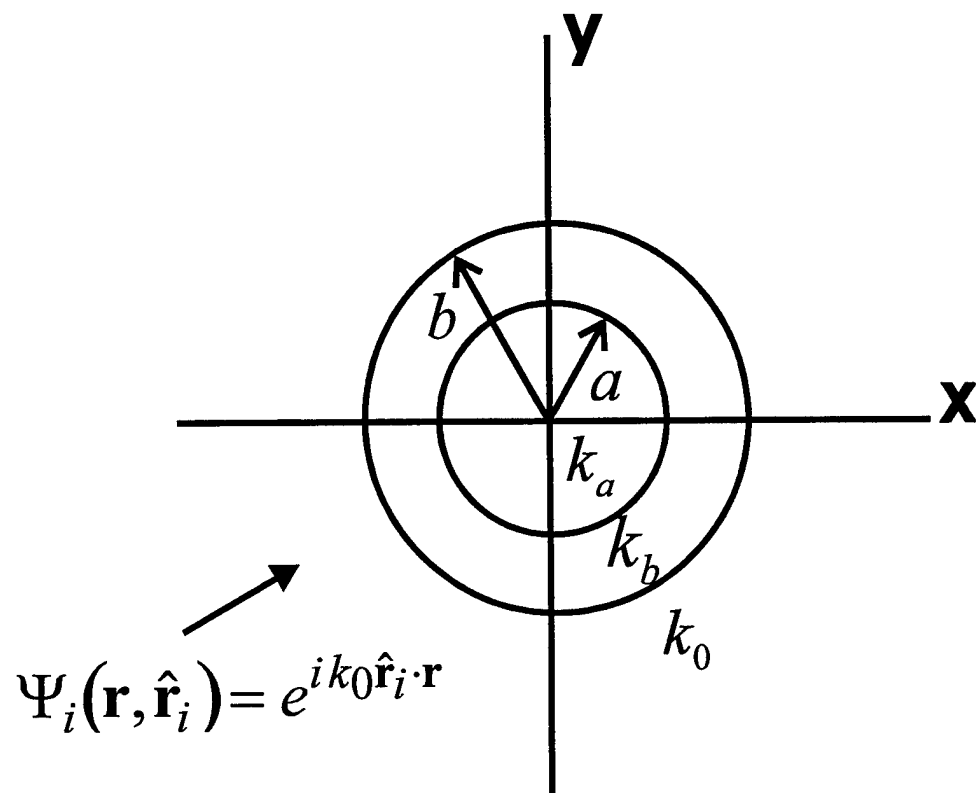


Figure 12 Cross section of two concentric cylinders of inner radius a and outer radius b .

where the prime denotes derivative with respect to ρ . The simultaneous solution of Eqs. (6.4), (6.5), (6.6) and (6.7) provides the unknown coefficients a_n, b_n, c_n and d_n . We find that

$$c_n = \frac{X}{Y + Z} \quad (6.8)$$

where,

$$\begin{aligned} X &= \left[k_a H_n^{(2)}(k_b a) J_n'(k_a a) - k_b H_n^{(2)'}(k_b a) J_n(k_a a) \right] \left[J_n'(k_0 b) H_n^{(1)}(k_0 b) - J_n(k_0 b) H_n^{(1)'}(k_0 b) \right] \\ Y &= \left[k_b H_n^{(1)'}(k_b a) J_n(k_a a) - k_a H_n^{(1)}(k_b a) J_n'(k_a a) \right] \left[\frac{k_b}{k_0} H_n^{(2)'}(k_b b) H_n^{(1)}(k_0 b) - H_n^{(2)}(k_b b) H_n^{(1)'}(k_0 b) \right] \\ Z &= \left[k_a H_n^{(2)}(k_b a) J_n'(k_a a) - k_b H_n^{(2)'}(k_b a) J_n(k_a a) \right] \left[\frac{k_b}{k_0} H_n^{(1)'}(k_b b) H_n^{(1)}(k_0 b) - H_n^{(1)}(k_b b) H_n^{(1)'}(k_0 b) \right] \end{aligned}$$

$$b_n = c_n \left[\frac{k_b J_n(k_a a) H_n^{(1)'}(k_b a) - k_a J_n'(k_a a) H_n^{(1)}(k_b a)}{k_a J_n'(k_a a) H_n^{(2)}(k_b a) - k_b J_n(k_a a) H_n^{(2)'}(k_b a)} \right] \quad (6.9)$$

$$d_n = \frac{k_b b_n H_n^{(2)'}(k_b a) + k_b c_n H_n^{(1)'}(k_b a)}{k_a J_n'(k_a a)} \quad (6.10)$$

$$a_n = \frac{k_b b_n H_n^{(2)'}(k_b b) + k_b c_n H_n^{(1)'}(k_b b) - k_0 J_n'(k_0 b)}{k_0 H_n^{(1)'}(k_0 b)} \quad (6.11)$$

The only coefficient given explicitly is c_n ; other coefficients are found through back substitution.

As described in Section 5, the $+n$ and $-n$ terms may be grouped to describe the fields $\Psi(\rho, \phi)$, $\Psi_b(\rho, \phi)$, and $\Psi_a(\rho, \phi)$ in a more simple form. Therefore, we may write the fields as a summation from $n = 0$ to $n = \infty$

$$\Psi(\rho, \phi) = \sum_{n=0}^{\infty} \varepsilon_n (-i)^n [J_n(k_0 \rho) + a_n H_n^{(1)}(k_0 \rho)] \cos(n\phi) \quad \text{for } \rho > b. \quad (6.12)$$

$$\Psi_b(\rho, \phi) = \sum_{n=0}^{\infty} \varepsilon_n (-i)^n [b_n H_n^{(2)}(k_b \rho) + c_n H_n^{(1)}(k_b \rho)] \cos(n\phi) \quad \text{for } a < \rho \leq b. \quad (6.13)$$

$$\Psi_a(\rho, \phi) = \sum_{n=0}^{\infty} \varepsilon_n (-i)^n [d_n J_n(k_a \rho)] \cos(n\phi) \quad \text{for } \rho \leq a, \quad (6.14)$$

where

$$\varepsilon_n \equiv \begin{cases} 2 & n = 0 \\ 1 & n = 1, 2, 3, \dots \end{cases}$$

Use of Eqs. (6.12), (6.13), and (6.14) allows one to calculate the total field at any point internal or external to the object. In practice, the infinite summations in the above equations are truncated once an established convergence criterion is met. Again, numerical computation of the field for $\rho > b$ is found by replacing the incident field by its simpler form

$$\Psi(\rho, \phi) = e^{-ik_0 x} + \sum_{n=0}^{\infty} \varepsilon_n (-i)^n a_n H_n^{(1)}(k_0 \rho) \cos(n\phi) . \quad (6.15)$$

The second term in Eq. (6.15) represents the scattered field ($\rho > b$) and is used as input to the inverse algorithm.

Equations (6.13), (6.14), and (6.15) are used to compute the total field at 10 GHz in the interior and exterior regions of several concentric cylinders. For each example considered, the inner permittivity was fixed at $\varepsilon_r = 2.2$, and the inner and outer radii were held constant at 2.15 cm and 4.25 cm, respectively.

In Figures 13 through 22 we plot the magnitude of the total field as the relative permittivity of the outer annulus increases from 1.01 to 10.0 (field incident from the top of the page). Again, the gray scale range is the same for each plot in Figures 13 through 22 so that the values remain relative.

The outer cylinder is undetectable until $\varepsilon_r = 1.4$ as shown in Figure 16. As the permittivity increases, focusing effects and shadow regions become more prominent. All examples shown in Figures 13 through 22 violate the criterion established in Section 3 for the weakly scattering approximation.

7. IMAGE RECONSTRUCTION ALGORITHM

In this section, we first demonstrate the Fourier transform relationship between the scattering potential and the scattered far-fields valid for weakly scattering objects [Wolf, 1969], [Devaney, 1977], [Chew, 1990], [Lin, et al, 1990]. Next, the problem associated with the Fourier inversion technique as it applies to strongly scattering objects is described. Lastly, image reconstruction using the single-view backpropagation algorithm is shown to be valid for arbitrary scatterers (weak or strong).

Recall the Green's function solution to the scattered field $\Psi^s(\mathbf{r}, \hat{\mathbf{r}}_i)$ given in Eq. (2.8)

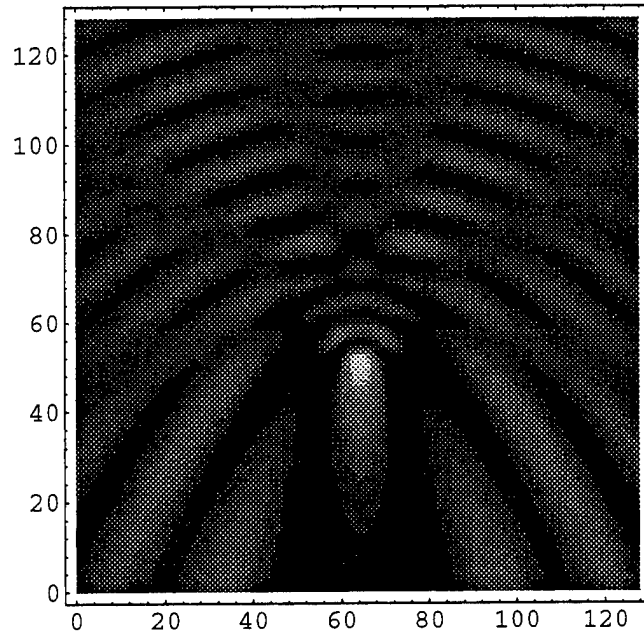


Figure 13 Total field intensity internal and external to two concentric dielectric cylinders (inner radius 0.0215 m and outer radius 0.0425 m) under plane wave illumination at 10 GHz. Relative permittivity of inner cylinder is fixed at $\epsilon_r = 2.2$ and relative permittivity of outer annulus is $\epsilon_r = 1.0$ Field-of-view is 0.1984 m on each side.

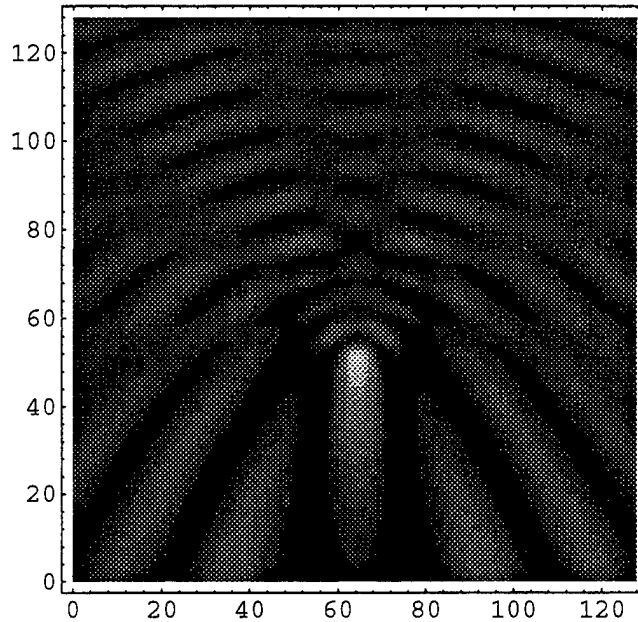


Figure 14 Total field intensity internal and external to two concentric dielectric cylinders (inner radius 0.0215 m and outer radius 0.0425 m) under plane wave illumination at 10 GHz. Relative permittivity of inner cylinder is fixed at $\epsilon_r = 2.2$ and relative permittivity of outer annulus is $\epsilon_r = 1.1$ Field-of-view is 0.1984 m on each side.

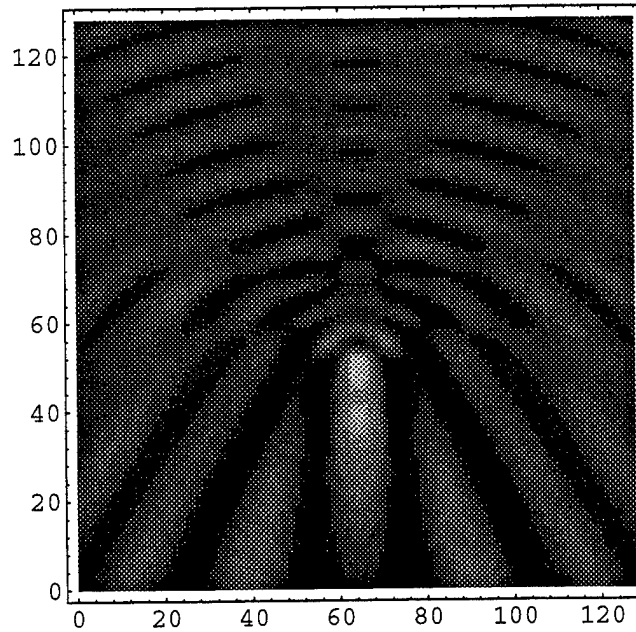


Figure 15 Total field intensity internal and external to two concentric dielectric cylinders (inner radius 0.0215 m and outer radius 0.0425 m) under plane wave illumination at 10 GHz. Relative permittivity of inner cylinder is fixed at $\epsilon_r = 2.2$ and relative permittivity of outer annulus is $\epsilon_r = 1.2$ Field-of-view is 0.1984 m on each side.

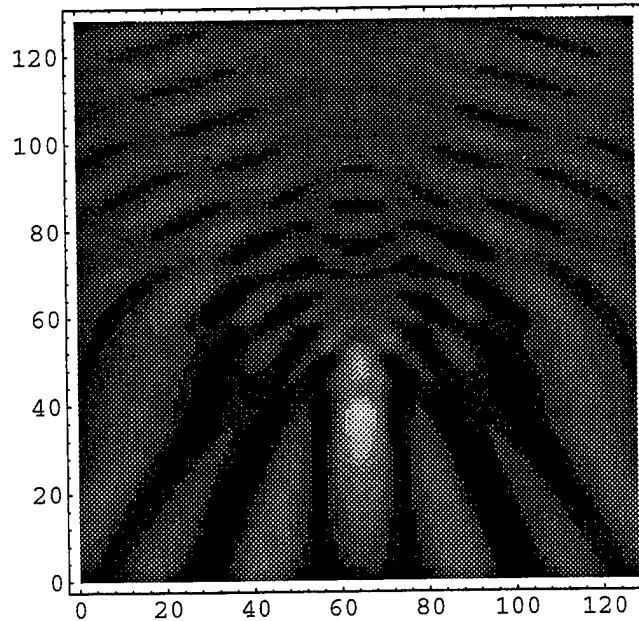


Figure 16 Total field intensity internal and external to two concentric dielectric cylinders (inner radius 0.0215 m and outer radius 0.0425 m) under plane wave illumination at 10 GHz. Relative permittivity of inner cylinder is fixed at $\epsilon_r = 2.2$ and relative permittivity of outer annulus is $\epsilon_r = 1.4$ Field-of-view is 0.1984 m on each side.

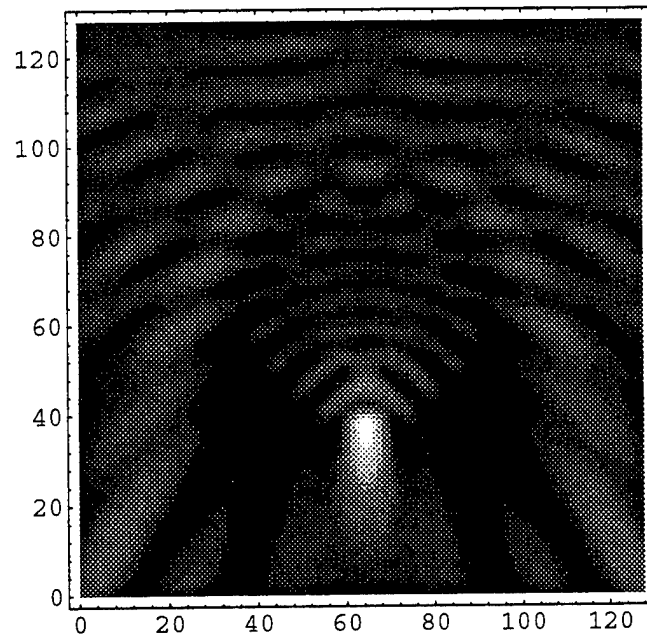


Figure 17 Total field intensity internal and external to two concentric dielectric cylinders (inner radius 0.0215 m and outer radius 0.0425 m) under plane wave illumination at 10 GHz. Relative permittivity of inner cylinder is fixed at $\epsilon_r = 2.2$ and relative permittivity of outer annulus is $\epsilon_r = 1.8$ Field-of-view is 0.1984 m on each side.

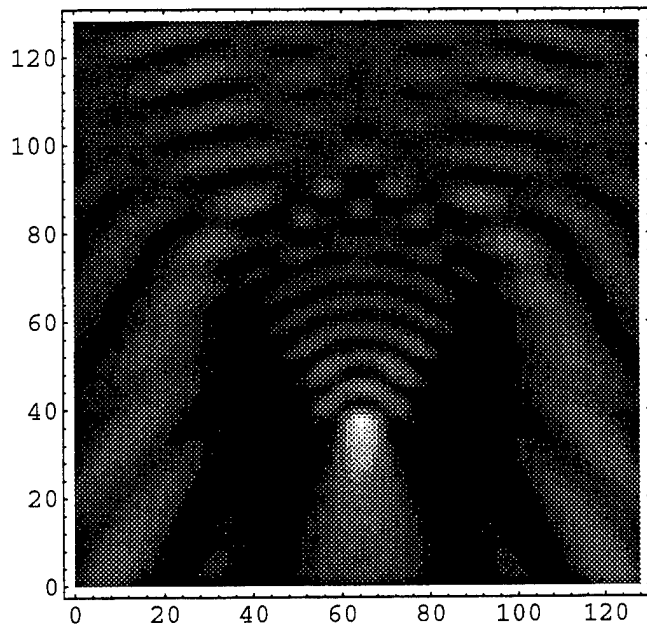


Figure 18 Total field intensity internal and external to two concentric dielectric cylinders (inner radius 0.0215 m and outer radius 0.0425 m) under plane wave illumination at 10 GHz. Relative permittivity of inner cylinder is fixed at $\epsilon_r = 2.2$ and relative permittivity of outer annulus is $\epsilon_r = 2.2$ Field-of-view is 0.1984 m on each side.

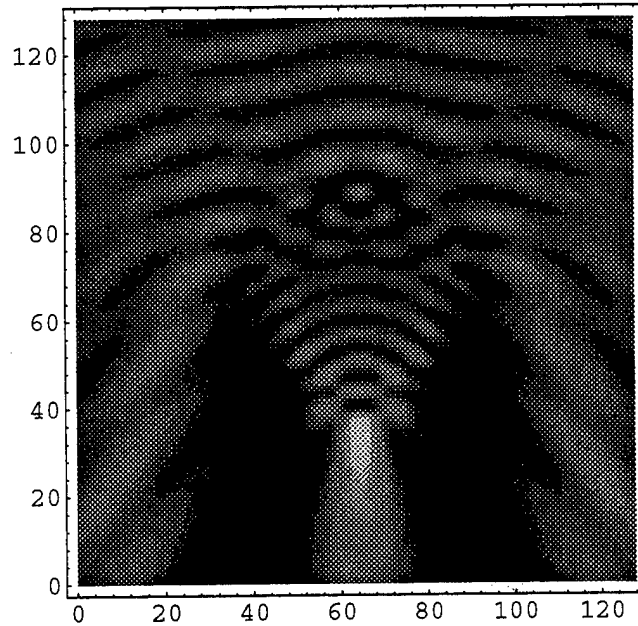


Figure 19 Total field intensity internal and external to two concentric dielectric cylinders (inner radius 0.0215 m and outer radius 0.0425 m) under plane wave illumination at 10 GHz. Relative permittivity of inner cylinder is fixed at $\epsilon_r = 2.2$ and relative permittivity of outer annulus is $\epsilon_r = 2.56$ Field-of-view is 0.1984 m on each side.

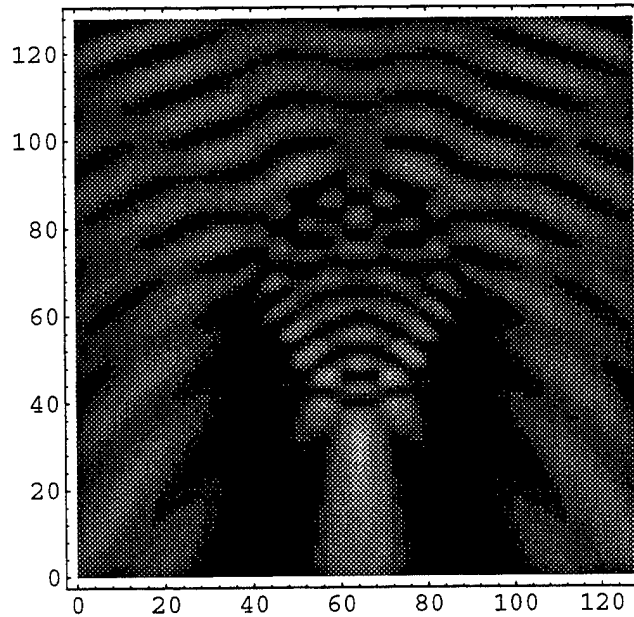


Figure 20 Total field intensity internal and external to two concentric dielectric cylinders (inner radius 0.0215 m and outer radius 0.0425 m) under plane wave illumination at 10 GHz. Relative permittivity of inner cylinder is fixed at $\epsilon_r = 2.2$ and relative permittivity of outer annulus is $\epsilon_r = 3.0$ Field-of-view is 0.1984 m on each side.

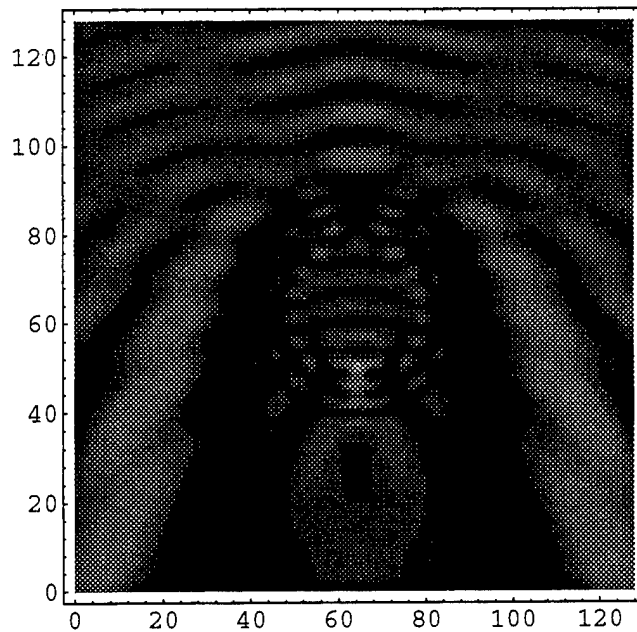


Figure 21 Total field intensity internal and external to two concentric dielectric cylinders (inner radius 0.0215 m and outer radius 0.0425 m) under plane wave illumination at 10 GHz. Relative permittivity of inner cylinder is fixed at $\epsilon_r = 2.2$ and relative permittivity of outer annulus is $\epsilon_r = 5.0$ Field-of-view is 0.1984 m on each side.

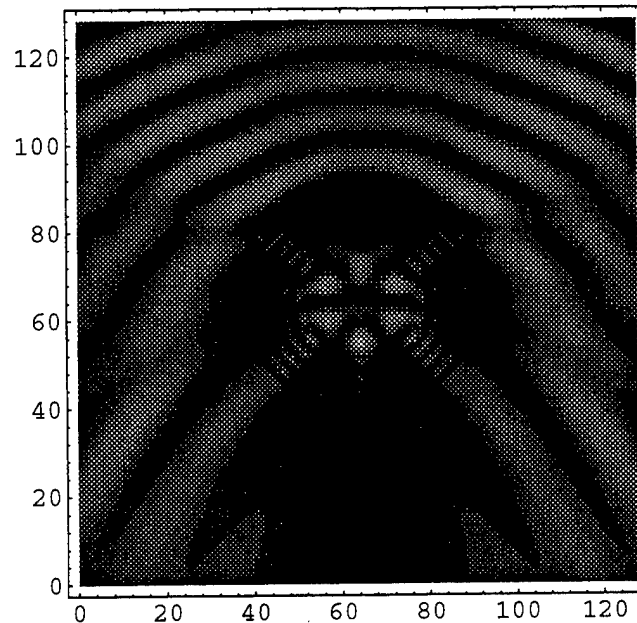


Figure 22 Total field intensity internal and external to two concentric dielectric cylinders (inner radius 0.0215 m and outer radius 0.0425 m) under plane wave illumination at 10 GHz. Relative permittivity of inner cylinder is fixed at $\epsilon_r = 2.2$ and relative permittivity of outer annulus is $\epsilon_r = 10.0$ Field-of-view is 0.1984 m on each side.

$$\Psi^s(\mathbf{r}, \hat{\mathbf{r}}_i) = k_0^2 \int_D V(\mathbf{r}') \Psi(\mathbf{r}', \hat{\mathbf{r}}_i) G(\mathbf{r}, \mathbf{r}') d\mathbf{r}', \quad (7.1)$$

where $\Psi^s(\mathbf{r}, \hat{\mathbf{r}}_i)$ is the scattered field, k_0 is the free space wavenumber, $V(\mathbf{r})$ is the scattering potential, and $G(\mathbf{r}, \mathbf{r}')$ is the Green's function. Assume that a plane wave is incident on the object from direction $\hat{\mathbf{r}}_i$ such that $\Psi(\mathbf{r}, \hat{\mathbf{r}}_i) = e^{ik_0 \hat{\mathbf{r}}_i \cdot \mathbf{r}} + \Psi^s(\mathbf{r}, \hat{\mathbf{r}}_i)$. Note that the field dependence on $\hat{\mathbf{r}}_i$ is shown explicitly in Eq. (7.1). Substituting for $\Psi(\mathbf{r}, \hat{\mathbf{r}}_i)$ and using Eq. (2.7) in Eq. (7.1) yields

$$\Psi^s(\mathbf{r}, \hat{\mathbf{r}}_i) = -i \frac{k_0^2}{4} \int_D V(\mathbf{r}') [e^{ik_0 \hat{\mathbf{r}}_i \cdot \mathbf{r}'} + \Psi^s(\mathbf{r}', \hat{\mathbf{r}}_i)] H_0^{(1)}(k_0 |\mathbf{r} - \mathbf{r}'|) d\mathbf{r}'. \quad (7.2)$$

The frequency dependence of $\Psi^s(\mathbf{r}, \hat{\mathbf{r}}_i)$ is not shown within the arguments since a single frequency is used throughout. In the far field, $H_0^{(1)}(k_0 |\mathbf{r} - \mathbf{r}'|)$ can be approximated [Morita, et al, 1990] by

$$H_0^{(1)}(k_0 |\mathbf{r} - \mathbf{r}'|) \cong \sqrt{\frac{2}{\pi k_0 |\mathbf{r} - \mathbf{r}'|}} e^{i(k_0 |\mathbf{r} - \mathbf{r}'| - \pi/4)}. \quad (7.3)$$

In addition, $|\mathbf{r} - \mathbf{r}'|$ may be approximated by $r - \mathbf{r}' \cdot \hat{\mathbf{r}}$ for phase terms (Appendix A) and by r for amplitude terms. Therefore, the far-field approximation of $H_0^{(1)}(k_0 |\mathbf{r} - \mathbf{r}'|)$ becomes

$$\begin{aligned} H_0^{(1)}(k_0 |\mathbf{r} - \mathbf{r}'|) &\cong \sqrt{\frac{2}{\pi k_0 r}} e^{i(k_0(r - \mathbf{r}' \cdot \hat{\mathbf{r}}) - \pi/4)} \\ &= \frac{4}{i} \sqrt{\frac{2}{16\pi k_0 r}} e^{i\pi/2} e^{ik_0 r} e^{-i\pi/4} e^{-ik_0 \mathbf{r}' \cdot \hat{\mathbf{r}}} \\ &= \frac{4}{i} \sqrt{\frac{1}{8\pi k_0 r}} e^{i(k_0 r + \pi/4)} e^{-ik_0 \mathbf{r}' \cdot \hat{\mathbf{r}}}. \end{aligned} \quad (7.4)$$

Upon substitution of Eq. (7.4) into Eq. (7.2), the scattered far field becomes

$$\Psi_{ff}^s(\mathbf{r}, \hat{\mathbf{r}}_i) = -\sqrt{\frac{k_0^3}{8\pi r}} e^{i(k_0 r + \pi/4)} \int_D V(\mathbf{r}') [e^{ik_0 \hat{\mathbf{r}}_i \cdot \mathbf{r}'} + \Psi^s(\mathbf{r}', \hat{\mathbf{r}}_i)] e^{-ik_0 \mathbf{r}' \cdot \hat{\mathbf{r}}} d\mathbf{r}'. \quad (7.5)$$

Equation (7.5) can be written in terms of a scattering amplitude $F(\mathbf{r}, \hat{\mathbf{r}}_i)$

$$F(\mathbf{r}, \hat{\mathbf{r}}_i) \equiv \frac{1}{4\pi^2} \int_D V(\mathbf{r}') [e^{ik_0 \hat{\mathbf{r}}_i \cdot \mathbf{r}'} + \Psi^s(\mathbf{r}', \hat{\mathbf{r}}_i)] e^{-ik_0 \mathbf{r}' \cdot \hat{\mathbf{r}}} d\mathbf{r}', \quad (7.6)$$

where

$$F(\mathbf{r}, \hat{\mathbf{r}}_i) = -\sqrt{\frac{r}{2\pi^3 k_0^3}} e^{-i(k_0 r + \pi/4)} \Psi_{ff}^s(\mathbf{r}, \hat{\mathbf{r}}_i). \quad (7.7)$$

Recall that for weakly scattering objects $|\Psi^s(\mathbf{r}, \hat{\mathbf{r}}_i)| \ll |\Psi^i(\mathbf{r}, \hat{\mathbf{r}}_i)|$ and $\Psi^s(\mathbf{r}, \hat{\mathbf{r}}_i)$ may be neglected under the integral in Eq. (7.6) (Section 3). In this case,

$$F^{BA}(\mathbf{r}, \hat{\mathbf{r}}_i) = \frac{1}{4\pi^2} \int_D V(\mathbf{r}') e^{-ik_0(\hat{\mathbf{r}} - \hat{\mathbf{r}}_i) \cdot \mathbf{r}'} d\mathbf{r}', \quad (7.8)$$

and the Fourier transform of the scattering potential is defined as

$$\tilde{V}(\mathbf{k}) \equiv \frac{1}{4\pi^2} \int_{-\infty}^{\infty} V(\mathbf{r}') e^{-i\mathbf{k} \cdot \mathbf{r}'} d\mathbf{r}'. \quad (7.9)$$

$F^{BA}(\mathbf{r}, \hat{\mathbf{r}}_i)$ specifies the Fourier transform of the scattering potential at $\mathbf{k} = k_0(\hat{\mathbf{r}} - \hat{\mathbf{r}}_i)$. In Cartesian coordinates, we may write

$$\tilde{V}(K_x, K_y) = \frac{1}{4\pi^2} \int_{-\infty}^{\infty} \int_{-\infty}^{\infty} V(x', y') e^{-i(K_x x' + K_y y')} dx' dy'. \quad (7.10)$$

As indicated in Eq. (7.8), the accessible range of Fourier values \mathbf{k} is limited to $k_0(\hat{\mathbf{r}} - \hat{\mathbf{r}}_i)$, or $K_x = k_0(\cos\phi_s - \cos\phi_i)$ and $K_y = k_0(\sin\phi_s - \sin\phi_i)$ in Cartesian coordinates.

With the angle of illumination ϕ_i constant, variation of the observation angle ϕ_s traces a circle of radius k_0 tangent to the origin of $K_x K_y$ space. More complete Fourier data are accumulated by selecting a new angle of incidence and again varying the observation angle ϕ_s . An inverse Fourier transform of the scattering amplitude data appropriately placed in $K_x K_y$ space produces an estimate of $V(x, y)$. The image is a low-pass filtered version of the original scattering potential since spatial frequencies higher than $|2k_0|$ generate evanescent waves whose contribution is essentially zero in the object's far field. Mathematically, the low-pass reconstruction of a weakly scattering object is written

$$V(x, y) ** h(x, y) = \frac{1}{4\pi^2} \int_{-\infty}^{\infty} \int_{-\infty}^{\infty} \tilde{V}(K_x, K_y) H(K_x, K_y) e^{i(K_x x' + K_y y')} dK_x dK_y \quad (7.11)$$

where ** represents two-dimensional convolution. Also, $h(x, y)$ is known as the point spread function (PSF) and its Fourier transform $H(K_x, K_y)$ is a frequency space "window" whose value is one for $\sqrt{K_x^2 + K_y^2} \leq 2k_0$ and zero otherwise. The PSF has $\lambda_0/2$ resolution (-3dB), a first side lobe level approximately -17.5 dB, and in practice, its effect has been largely neglected [Pan et al, 1983].

When imaging objects violate the Born approximation, Ho and Carter [1976] noticed that the image of the scattering potential was perturbed by the incident field. Slaney, Kak, and Larsen [1984] then proposed an alternative interpretation of the Born approximation that can be described as follows. Equation (7.6) can be written in the form

$$F(\mathbf{r}, \hat{\mathbf{r}}_i) = \frac{1}{4\pi^2} \int_D V(\mathbf{r}') \Psi(\mathbf{r}', \hat{\mathbf{r}}_i) \left[\frac{\Psi^i(\mathbf{r}', \hat{\mathbf{r}}_i)}{\Psi^i(\mathbf{r}', \hat{\mathbf{r}}_i)} \right] e^{-ik_0 \mathbf{r}' \cdot \hat{\mathbf{r}}} d\mathbf{r}' \quad (7.12)$$

where the total field $\Psi(\mathbf{r}, \hat{\mathbf{r}}_i)$ is written for $e^{ik_0 \hat{\mathbf{r}}_i \cdot \mathbf{r}} + \Psi^s(\mathbf{r}, \hat{\mathbf{r}}_i)$ and the term in brackets (unity) is introduced. Since $\Psi^i(\mathbf{r}, \hat{\mathbf{r}}_i) = e^{ik_0 \hat{\mathbf{r}}_i \cdot \mathbf{r}}$, we may write (7.12) as

$$F(\mathbf{r}, \hat{\mathbf{r}}_i) = \frac{1}{4\pi^2} \int_D V'(\mathbf{r}', \hat{\mathbf{r}}_i) e^{-ik_0 (\hat{\mathbf{r}} - \hat{\mathbf{r}}_i) \cdot \mathbf{r}'} d\mathbf{r}', \quad (7.13)$$

where the effective scattering potential is

$$V'(\mathbf{r}, \hat{\mathbf{r}}_i) \equiv \frac{V(\mathbf{r}) \Psi(\mathbf{r}, \hat{\mathbf{r}}_i)}{\Psi^i(\mathbf{r}, \hat{\mathbf{r}}_i)} \quad (7.14)$$

and its Fourier transform is defined by

$$\tilde{V}'(\mathbf{k}) \equiv \frac{1}{4\pi^2} \int_{-\infty}^{\infty} V'(\mathbf{r}', \hat{\mathbf{r}}_i) e^{-i\mathbf{k} \cdot \mathbf{r}'} d\mathbf{r}'. \quad (7.15)$$

$F(\mathbf{r}, \hat{\mathbf{r}}_i)$ determines the Fourier transform of the effective scattering potential at $\mathbf{k} = k_0(\hat{\mathbf{r}} - \hat{\mathbf{r}}_i)$. In effect, blindly applying the Born approximation will provide Fourier data on $V'(\mathbf{r}, \hat{\mathbf{r}}_i)$. Equation (7.13) is used as the basis of an inversion algorithm for strongly scattering objects - those objects that violate the Born approximation. Of course, Eq. (7.13) reduces to Eq. (7.8)

when the Born approximation is valid. Equation (7.13) represents an alternative interpretation of the integral equation of scattering and we shall discuss limitations that arise when objects are strong scatterers.

In Cartesian coordinates Eq. (7.15) is written

$$\tilde{V}'(K_x, K_y) = \frac{1}{4\pi^2} \int_{-\infty}^{\infty} \int_{-\infty}^{\infty} V'(x', y', \phi_i) e^{-i(K_x x' + K_y y')} dx' dy'. \quad (7.16)$$

In an attempt to recover $V'(x, y, \phi_i)$ one might try the inverse Fourier transform, by multiplying both sides of Eq. (7.16) by $e^{i(K_x x + K_y y)}$ and integrating over all K_x and K_y as shown in an analogous example in Appendix B. However, $V'(x, y, \phi_i)$ cannot be removed from the innermost two integrals that result, as shown in Appendix B, since $V'(x, y, \phi_i)$ depends on the Fourier variables K_x and K_y . Therefore, simple Fourier inversion (using all K_x and K_y space) is not appropriate to recover $V'(x, y, \phi_i)$ for strongly scattering objects.

Dechene, et al, [1985] implemented a reconstruction algorithm that did not require first-order Born or Rytov approximations to be valid. They simply applied the weak scattering Fourier algorithm using data acquired from more strongly scattering objects. The qualitative images obtained could not be related to the object function of concern. The authors did admit that the technique had problems related to the appropriateness of image reconstruction by Fourier inversion when the objects violated the Born or Rytov approximation.

To avoid the problems mentioned above, we utilize the backpropagation algorithm [Devaney, 1982] using a single illumination direction. In this case, ϕ_i remains constant and Fourier inversion of Eq. (7.16) is valid for arbitrary scatterers.

The backpropagation algorithm was originally developed for those objects that satisfy Born or Rytov approximations and can be written as

$$V(\mathbf{r}') ** h(\mathbf{r}') = \frac{k_0^2}{2} \int_{-\pi}^{\pi} \int_{-\pi}^{\pi} F(\mathbf{r}, \hat{\mathbf{r}}_i) e^{ik_0(\hat{\mathbf{r}} - \hat{\mathbf{r}}_i) \cdot \mathbf{r}'} \sqrt{1 - \cos^2(\phi_s - \phi_i)} d\phi_s d\phi_i, \quad (7.17)$$

where $h(\mathbf{r}')$ is the PSF described earlier. Equation (7.17) is equivalent to the inverse 2D Fourier transform of $F(\mathbf{r}, \hat{\mathbf{r}}_i)$ with a change in variables from (K_x, K_y) to (ϕ_s, ϕ_i) . The square root factor arises from the Jacobian [Grossman, 1986, p. 389] of the transformation such that

$$\begin{vmatrix} \frac{\partial K_x}{\partial \phi_s} & \frac{\partial K_x}{\partial \phi_i} \\ \frac{\partial K_y}{\partial \phi_s} & \frac{\partial K_y}{\partial \phi_i} \end{vmatrix} = \begin{vmatrix} -k_0 \sin \phi_s & k_0 \sin \phi_i \\ k_0 \cos \phi_s & -k_0 \cos \phi_i \end{vmatrix} = k_0^2 \sqrt{1 - \cos^2(\phi_s - \phi_i)}. \quad (7.18)$$

Also, a factor of 1/2 is included in Eq. (7.17) since the Fourier domain is covered twice by this change in variables.

It was mentioned previously that backpropagation is not appropriate to recover $V'(\mathbf{r}', \hat{\mathbf{r}}_i)$, that is

$$V'(\mathbf{r}', \hat{\mathbf{r}}_i) ** h(\mathbf{r}') \neq \frac{k_0^2}{2} \int_{-\pi-\pi}^{\pi} \int_{-\pi-\pi}^{\pi} F(\mathbf{r}, \hat{\mathbf{r}}_i) e^{ik_0(\hat{\mathbf{r}}-\hat{\mathbf{r}}_i) \cdot \mathbf{r}'} \sqrt{1 - \cos^2(\phi_s - \phi_i)} d\phi_s d\phi_i. \quad (7.19)$$

However, by specifying ϕ_i to be constant, we may formulate a single-view (sv) image of $V'(\mathbf{r}', \hat{\mathbf{r}}_i)$

$$V'(\mathbf{r}', \hat{\mathbf{r}}_i) ** h_{sv}(\mathbf{r}', \hat{\mathbf{r}}_i) = \frac{k_0^2}{2} \int_{-\pi}^{\pi} F(\mathbf{r}, \hat{\mathbf{r}}_i) e^{ik_0(\hat{\mathbf{r}}-\hat{\mathbf{r}}_i) \cdot \mathbf{r}'} \sqrt{1 - \cos^2(\phi_s - \phi_i)} d\phi_s. \quad (7.20)$$

The image of $V'(\mathbf{r}', \hat{\mathbf{r}}_i)$ is convolved with $h_{sv}(\mathbf{r}', \hat{\mathbf{r}}_i)$ since Fourier data on $V'(\mathbf{r}', \hat{\mathbf{r}}_i)$ is limited, in this case, to the frequency space circle $k_0(\hat{\mathbf{r}} - \hat{\mathbf{r}}_i)$ with ϕ_i constant. Here $h_{sv}(\mathbf{r}', \hat{\mathbf{r}}_i)$ is the inverse Fourier transform of the frequency space window, which has the weighted value

$\sqrt{1 - \cos^2(\phi_s - \phi_i)}$ on the Fourier coordinates $k_0(\hat{\mathbf{r}} - \hat{\mathbf{r}}_i)$, and zero otherwise. Recall that the weighting was introduced from the change in variables in the inverse Fourier transform and was necessary to combine multiview data as in Eq. (7.17). Equation (7.20) represents a single-view reconstructed image of $V'(\mathbf{r}', \hat{\mathbf{r}}_i)$ convolved with $h_{sv}(\mathbf{r}', \hat{\mathbf{r}}_i)$. In Section 11, there is a discussion of a nonlinear filtering technique that attempts to recover the scattering potential $V(x, y)$ from the image produced by Eq. (7.20) for various simulated scattered fields. Note that uniqueness in the reconstruction of $V'(\mathbf{r}', \hat{\mathbf{r}}_i)$ cannot be guaranteed [Devaney, 1978].

8. BORN RECONSTRUCTIONS

In Section 7, images reconstructed according to the backpropagation algorithm of Eq. (7.17) provided a low-pass estimate of the scattering potential $V(\mathbf{r})$. In this section, we reconstruct multiview images using the exact scattering amplitude from several strongly scattering objects without regard to the appropriateness of doing so. Images of the objects are expected to deteriorate as the Born approximation becomes less valid. Duchene, et al, [1985] implemented a similar procedure and found difficulty in relating multiview images to quantitative descriptions of the object's scattering potential.

The objects used in this study are concentric cylinders since they are strongly scattering 2D objects and an exact solution to the scattered field was given in Section 6. We examine five concentric cylinders with outer/inner relative permittivities of 1.1/1.03, 1.03/1.1, 4/4, 4/2, and 2/4. A one-dimensional profile through the various cylinders is shown in Figure 23. Hereafter, these objects will be referred to as obj_1.1/1.03, obj_1.03/1.1, obj_4/4, obj_4/2, and obj_2/4 as

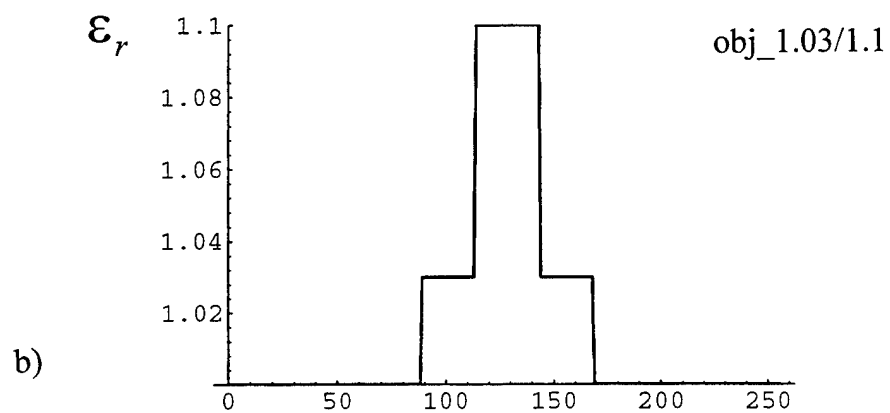
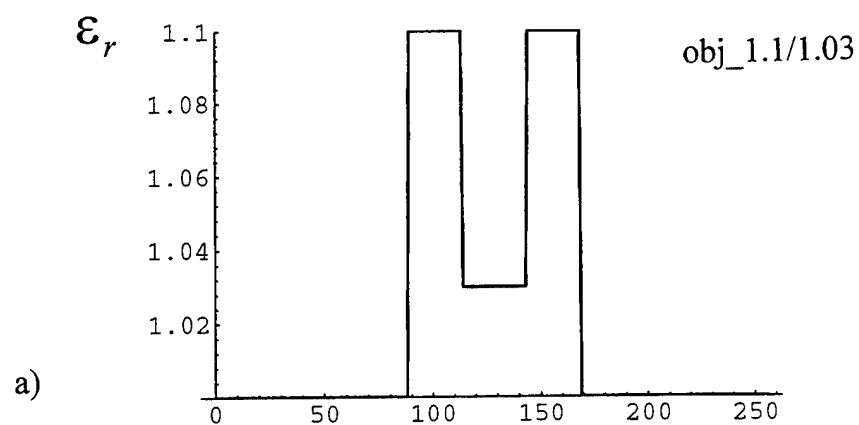


Figure 23 Radial cuts in relative permittivity for various cylinders under investigation
a) obj_1.1/1.03 b) obj_1.03/1.1 c) obj_4/4 d) obj_4/2 e) obj_2/4.

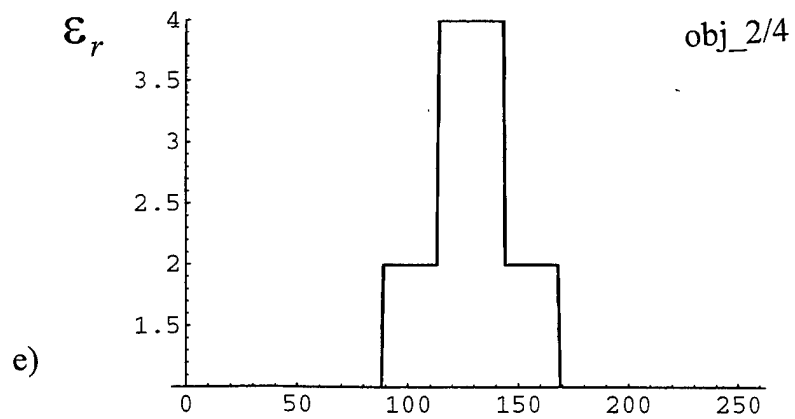
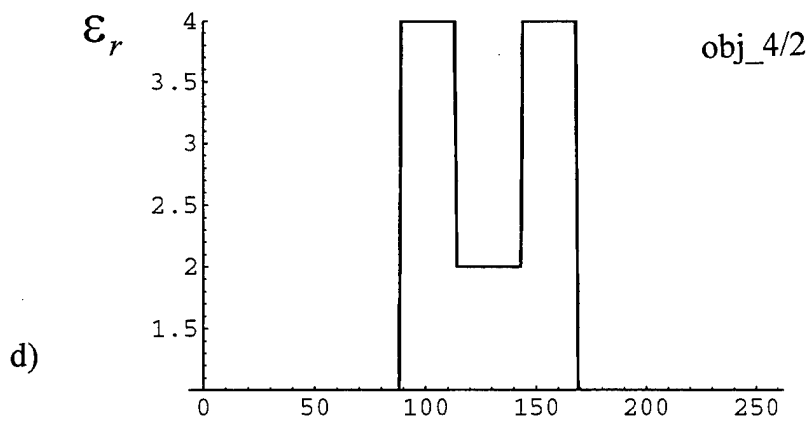
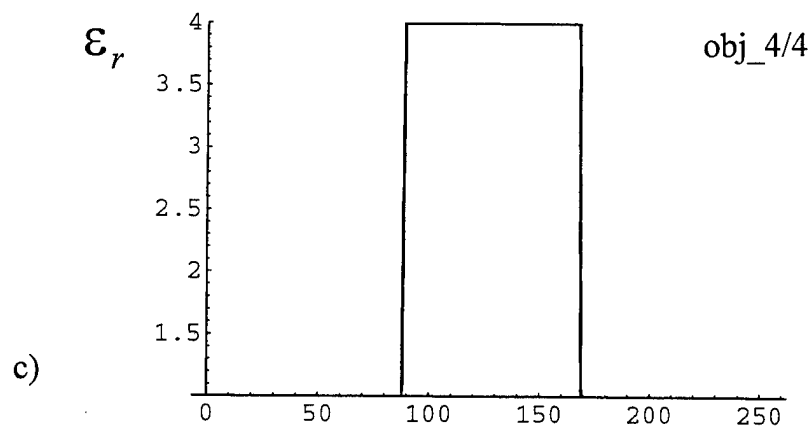


Figure 23 (cont.) Radial cuts in relative permittivity for various cylinders under investigation a) obj_1.1/1.03 b) obj_1.03/1.1 c) obj_4/4 d) obj_4/2 e) obj_2/4.

indicated in Figure 23. For each concentric cylinder the inner radius is 3.6 cm and the outer radius is 9.9 cm. The abscissa index of all plots shown in Figure 23 spans a field of view of 64 cm; that is, each abscissa unit in Figure 23 represents 0.25 cm.

Recall that the Born approximation requires that the phase delay introduced by the object's presence be small compared to the phase accumulated in the absence of the object, as mentioned in Section 3. Mathematically, $|k_0(1 - \sqrt{\epsilon_r})a|$ should be less than 2 radians [Fiddy, 1986]. Using the cylinder's diameter for a , we find that $|k_0(1 - \sqrt{\epsilon_r})a|$ ranges from approximately 2 for obj_1.1/1.03 and obj_1.03/1.1 to 41 for obj_4/4, obj_4/2, and obj_2/4. The first two cylinders shown in Figure 23 a) and b) may be considered weakly scattering objects. However, the cylinders shown in Figures 23 c), d), and e) clearly violate Eq. (3.5) and are considered strongly scattering objects.

In what follows, we backpropagate the exact scattered field data using the objects shown in Figure 23. Fifteen equally spaced illumination directions or views were processed for each object. Again, images reconstructed from more strongly scattering objects using this multiview technique are expected to be poor since they violate the Born approximation.

Figures 24, 25, and 26 show the real part, the imaginary part, and the magnitude, respectively, of the equivalent Born reconstruction for obj_1.1/1.03. In Figure 27, we see a one dimensional slice through the two dimensional image of Figure 26. The magnitude of the resultant image is similar to the original profile shown in Figure 23 a).

Figures 28, 29, and 30 show the real part, the imaginary part, and the magnitude, respectively, of the equivalent Born reconstruction for obj_1.03/1.1. A one dimensional slice through the two dimensional image of Figure 30 is shown in Figure 31. Again the magnitude of the image agrees with the original profile shown in Figure 23 b).

Similar plots for the more strongly scattering objects are shown in the remaining figures. Specifically, Figures 32 through 35 correspond to obj_4/4, Figures 36 through 39 correspond to obj_4/2, and Figures 40 through 43 correspond to obj_2/4. Although the equivalent Born reconstruction does identify the edges well, the structure of the scattering potential is not recovered for these more strongly scattering objects as shown in Figures 35, 39, and 43.

9. DIFFERENTIAL CEPSTRAL FILTERING

Two signals combined by additive "superposition" can be separated through linear filtering in the spectral domain, as long as their spectra do not overlap. However, linear filtering cannot be applied to two signals that are combined through multiplicative or convolutional "superposition" because their spectra are convolved and multiplied, respectively, [Oppenheim, et al, 1968, 1975]. Oppenheim [1965] generalized the theory of superposition to include those signals combined through addition, multiplication, convolution, etc. The combined signals were transformed into an additive space, which could be treated with a simple linear filter, then inverted to the original data space. In this section, we desire to separate the scattering potential

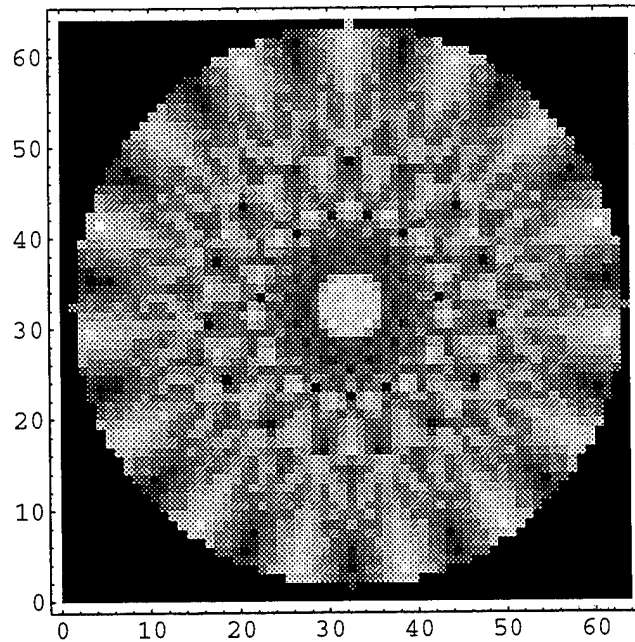


Figure 24 Real part of equivalent Born reconstruction of obj_1.1/1.03 using 15 equally spaced illumination directions. Field-of-view $64 \times 64 \text{ cm}^2$.

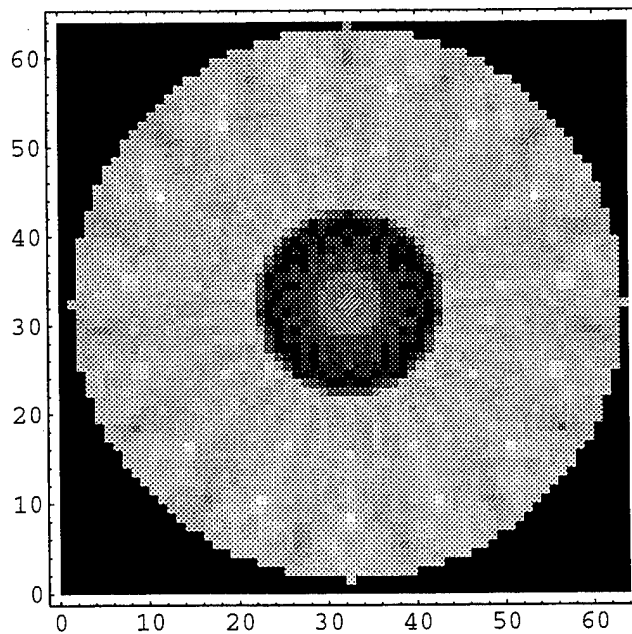


Figure 25 Imaginary part of equivalent Born reconstruction of obj_1.1/1.03 using 15 equally spaced illumination directions. Field-of-view $64 \times 64 \text{ cm}^2$.

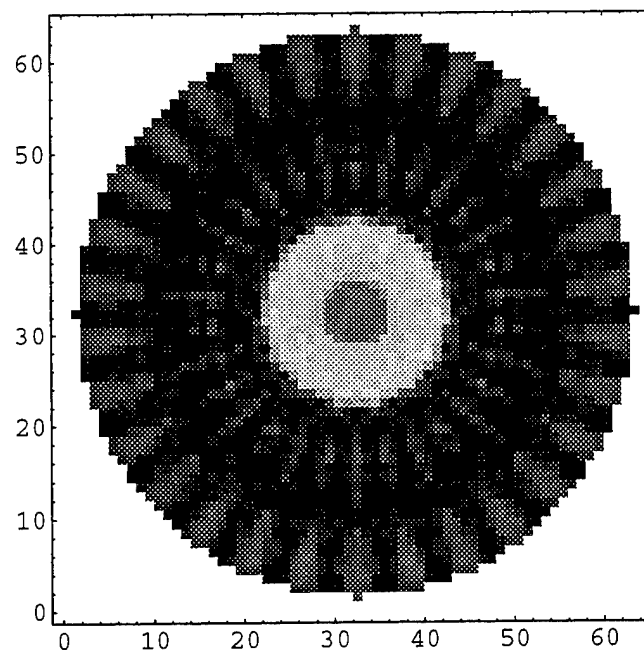


Figure 26 Magnitude of equivalent Born reconstruction of obj_1.1/1.03 using 15 equally spaced illumination directions. Field-of-view $64 \times 64 \text{ cm}^2$.

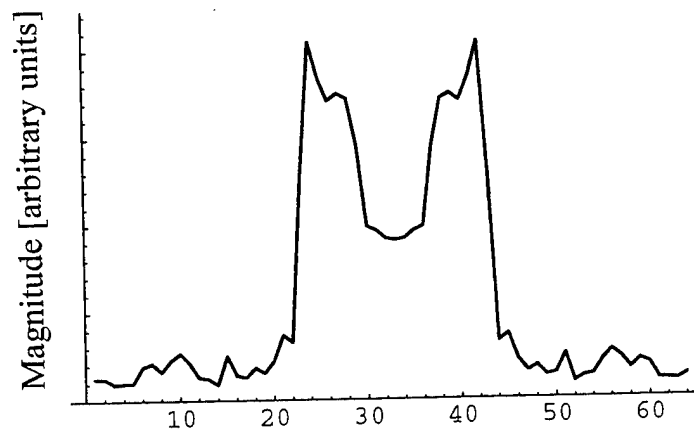


Figure 27 One dimensional slice through the center of Figure 26. Length of slice is 64cm.

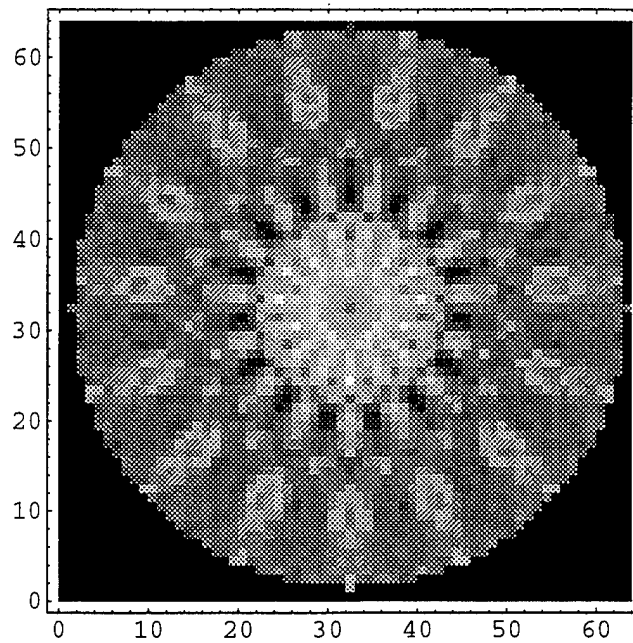


Figure 28 Real part of equivalent Born reconstruction of obj_1.03/1.1 using 15 equally spaced illumination directions. Field-of-view $64 \times 64 \text{ cm}^2$.

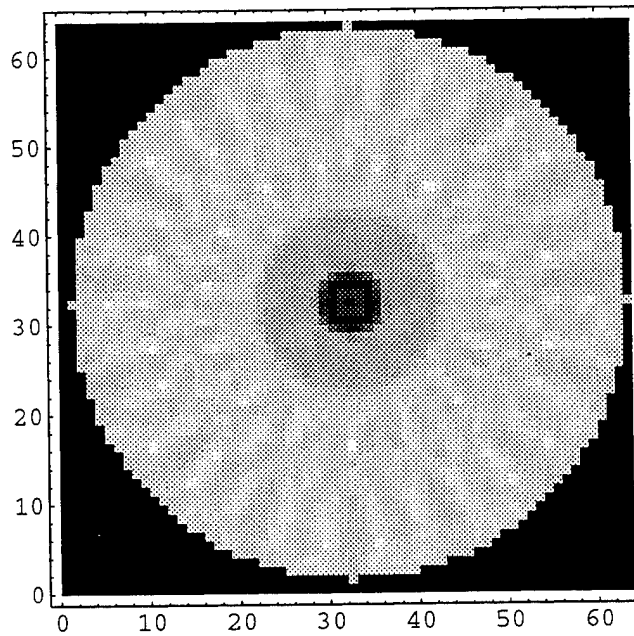


Figure 29 Imaginary part of equivalent Born reconstruction of obj_1.03/1.1 using 15 equally spaced illumination directions. Field-of-view $64 \times 64 \text{ cm}^2$.

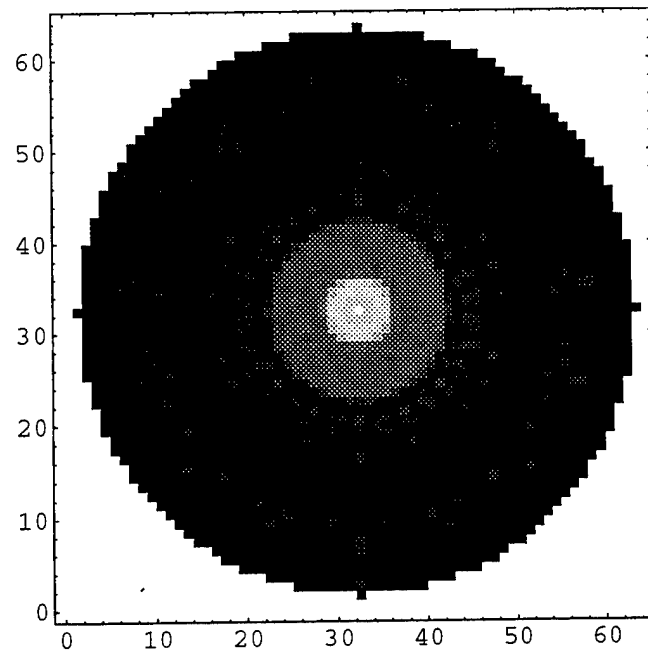


Figure 30 Magnitude of equivalent Born reconstruction of obj_1.03/1.1 using 15 equally spaced illumination directions. Field-of-view $64 \times 64 \text{ cm}^2$.

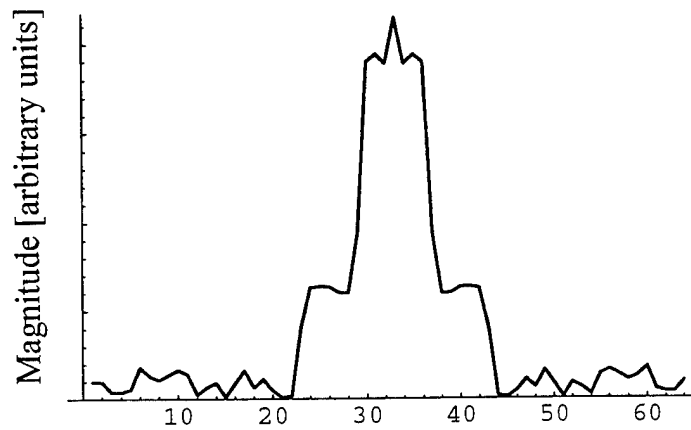


Figure 31 One dimensional slice through the center of Figure 30. Length of slice is 64cm.

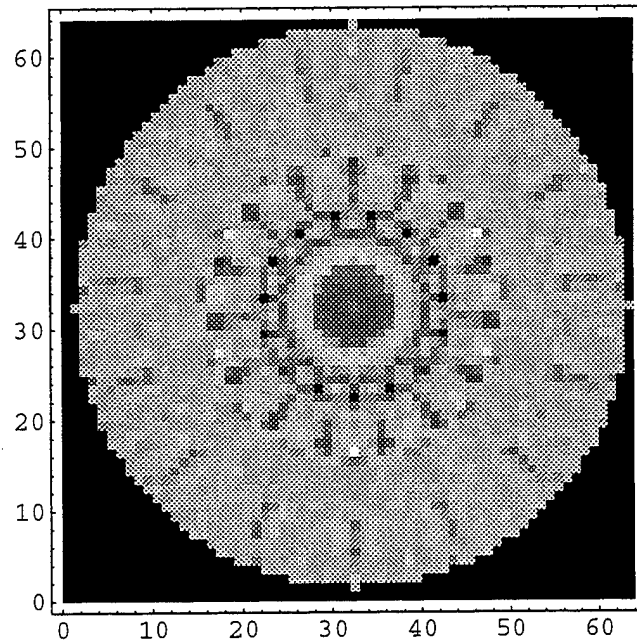


Figure 32 Real part of equivalent Born reconstruction of obj_4/4 using 15 equally spaced illumination directions. Field-of-view $64 \times 64 \text{ cm}^2$.

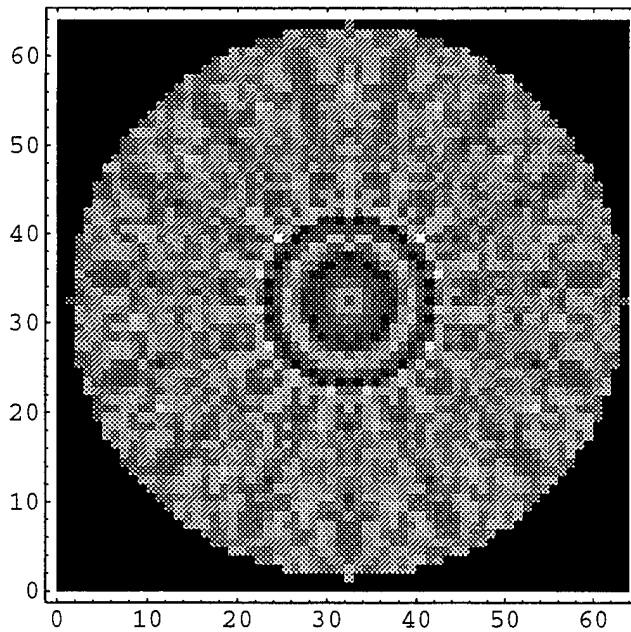


Figure 33 Imaginary part of equivalent Born reconstruction of obj_4/4 using 15 equally spaced illumination directions. Field-of-view $64 \times 64 \text{ cm}^2$.

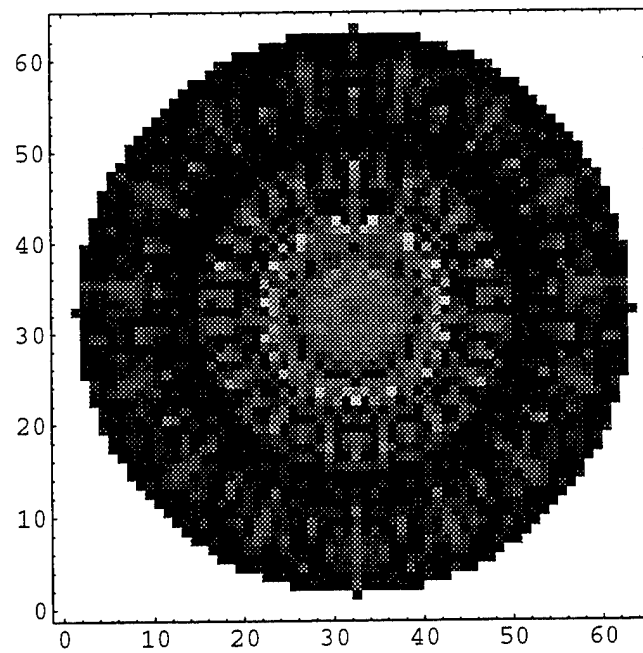


Figure 34 Magnitude of equivalent Born reconstruction of obj_4/4 using 15 equally spaced illumination directions. Field-of-view $64 \times 64 \text{ cm}^2$.

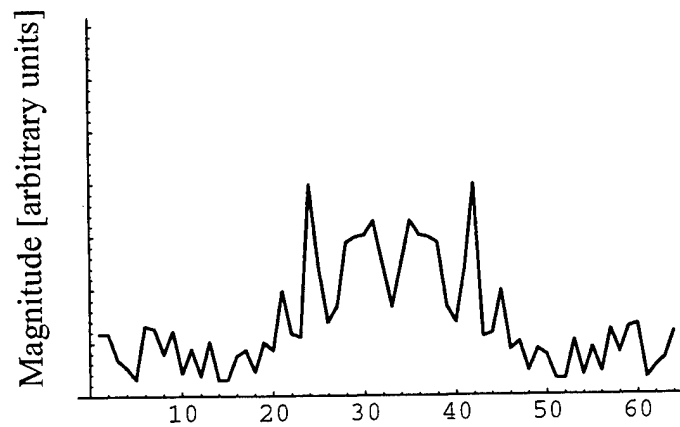


Figure 35 One dimensional slice through the center of Figure 34. Field-of-view 64cm.

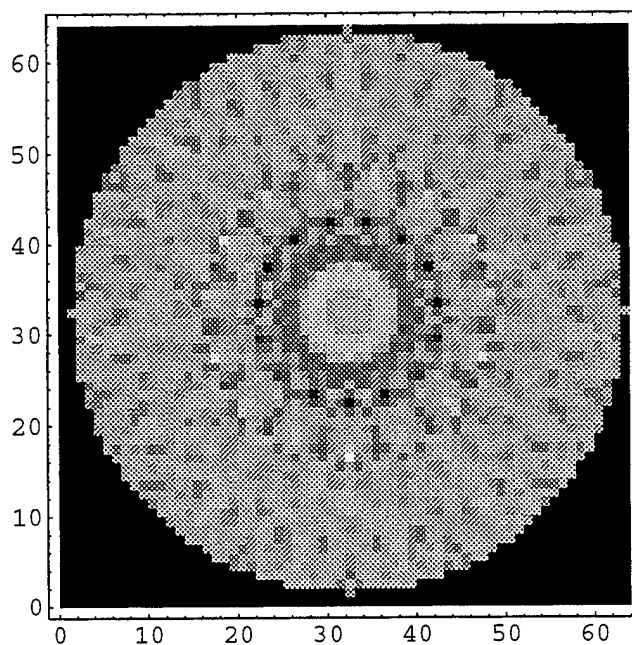


Figure 36 Real part of equivalent Born reconstruction of obj_4/2 using 15 equally spaced illumination directions. Field-of-view $64 \times 64 \text{ cm}^2$.

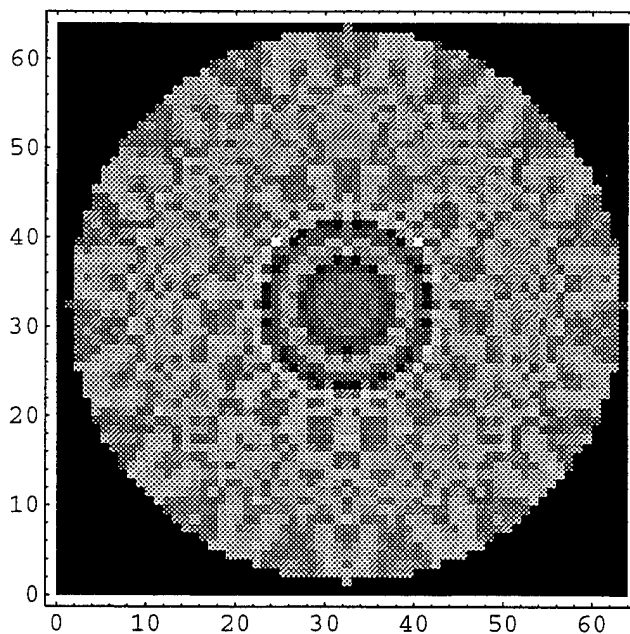


Figure 37 Imaginary part of equivalent Born reconstruction of obj_4/2 using 15 equally spaced illumination directions. Field-of-view $64 \times 64 \text{ cm}^2$.

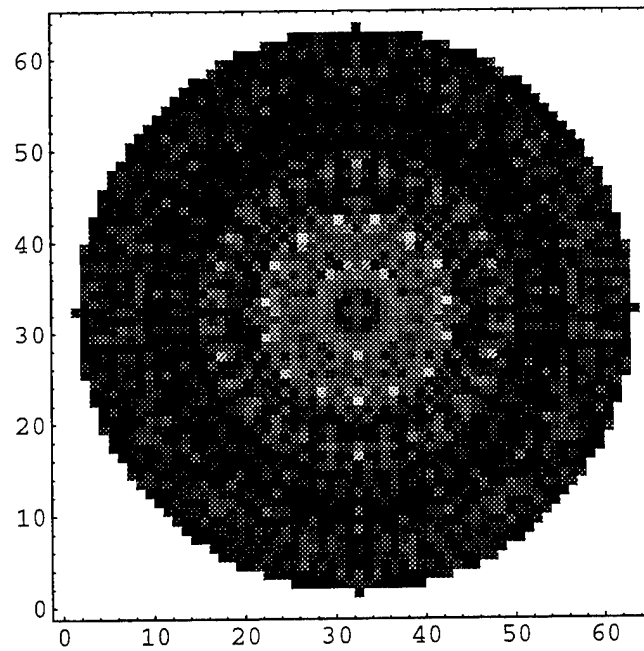


Figure 38 Magnitude of equivalent Born reconstruction of obj_4/2 using 15 equally spaced illumination directions. Field-of-view $64 \times 64 \text{ cm}^2$.

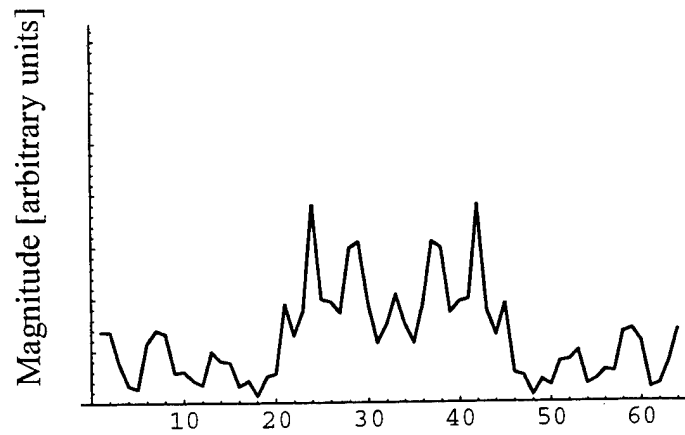


Figure 39 One dimensional slice through the center of Figure 38. Length of slice is 64cm.

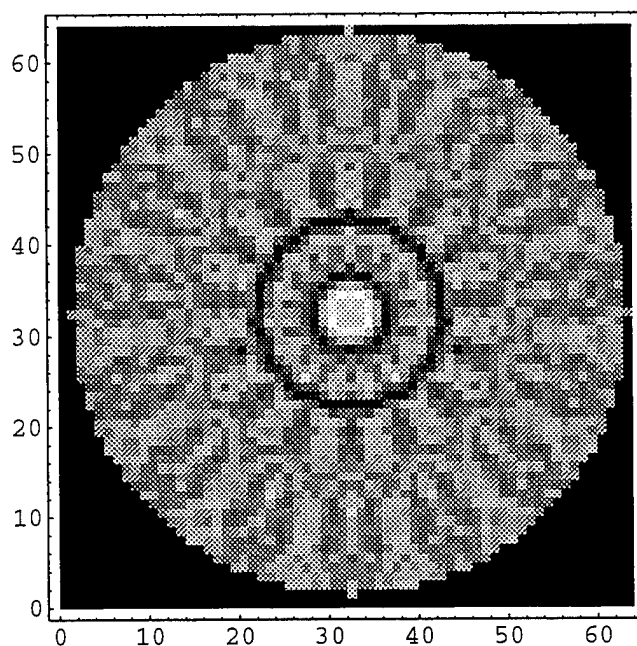


Figure 40 Real part of equivalent Born reconstruction of obj_2/4 using 15 equally spaced illumination directions. Field-of-view $64 \times 64 \text{ cm}^2$.

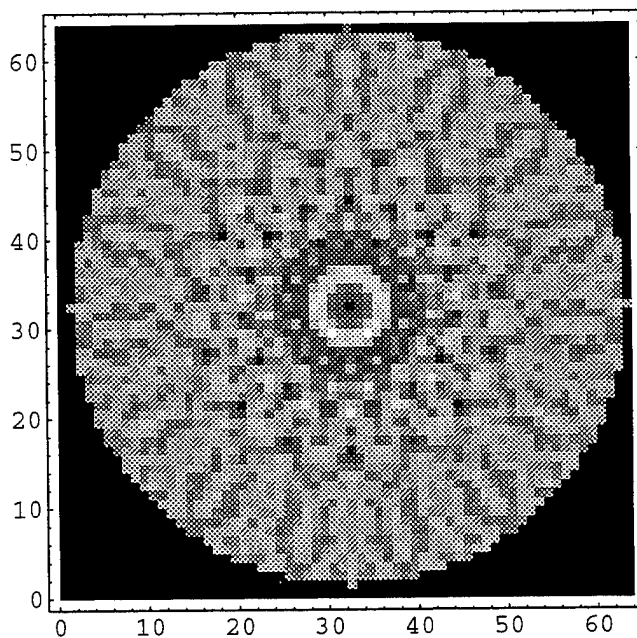


Figure 41 Imaginary part of equivalent Born reconstruction of obj_2/4 using 15 equally spaced illumination directions. Field-of-view $64 \times 64 \text{ cm}^2$.

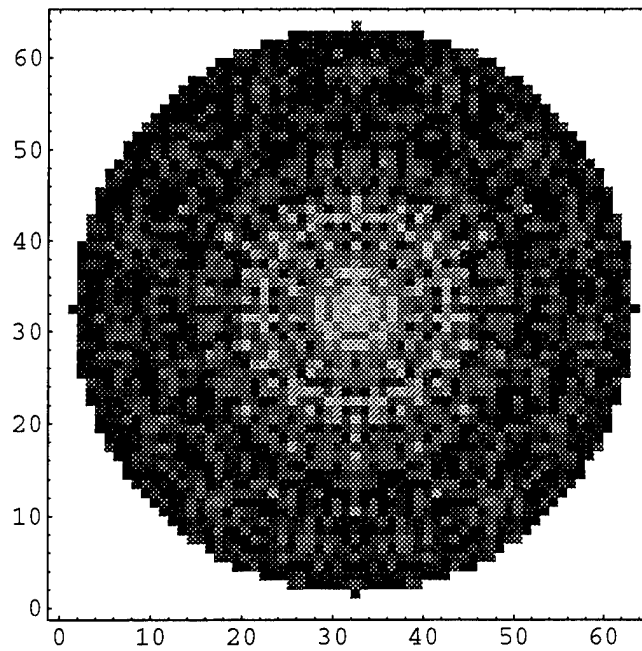


Figure 42 Magnitude of equivalent Born reconstruction of obj_2/4 using 15 equally spaced illumination directions. Field-of-view 64x64 cm².

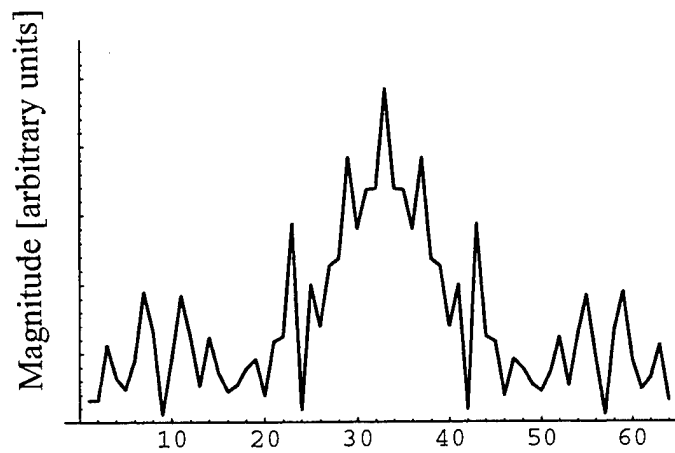


Figure 43 One dimensional slice through the center of Figure 42. Length of slice is 64cm.

$V(\mathbf{r})$ from the backpropagated image $V(\mathbf{r}) \frac{\Psi(\mathbf{r}, \hat{\mathbf{r}}_i)}{\Psi^i(\mathbf{r}, \hat{\mathbf{r}}_i)} ** h_{sv}(\mathbf{r})$. Note that uniqueness in the reconstruction of $V(\mathbf{r})$ cannot be guaranteed [Devaney, 1978]. The width of the point spread function $h_{sv}(\mathbf{r})$ is assumed to be smaller than the scale of the inhomogeneities and is neglected unless noted otherwise. This is a case of multiplicative superposition and requires the application of a nonlinear process known as differential cepstral filtering (described later).

Homomorphic systems are systems represented by algebraically linear transformation between input and output vector spaces [Oppenheim, 1975]. Use of the term "homomorphic" was motivated by the algebraic definition of a homomorphic mapping between vector spaces [Oppenheim, 1965]. Homomorphic filtering has been successfully applied to separating signals that have been combined through multiplication and convolution.

In our application, we are given the multiplicative input $V(\mathbf{r}) \frac{\Psi(\mathbf{r}, \hat{\mathbf{r}}_i)}{\Psi^i(\mathbf{r}, \hat{\mathbf{r}}_i)}$ and wish to apply the nonlinear homomorphic filtering technique to remove the factor $\frac{\Psi(\mathbf{r}, \hat{\mathbf{r}}_i)}{\Psi^i(\mathbf{r}, \hat{\mathbf{r}}_i)}$. The transformation that converts this multiplicative relationship to an additive relationship is the logarithmic operator, since $\log(ab) = \log a + \log b$. A linear filter applied to the spectrum of

$$\log \left[V(\mathbf{r}) \frac{\Psi(\mathbf{r}, \hat{\mathbf{r}}_i)}{\Psi^i(\mathbf{r}, \hat{\mathbf{r}}_i)} \right] = \log |V(\mathbf{r})| + \log \left| \frac{\Psi(\mathbf{r}, \hat{\mathbf{r}}_i)}{\Psi^i(\mathbf{r}, \hat{\mathbf{r}}_i)} \right| + i \left\{ \arg[V(\mathbf{r})] + \arg \left[\frac{\Psi(\mathbf{r}, \hat{\mathbf{r}}_i)}{\Psi^i(\mathbf{r}, \hat{\mathbf{r}}_i)} \right] + 2\pi k \right\}, \quad k = 0, 1, 2, \dots \quad (9.1)$$

is sought to isolate $V(\mathbf{r})$ from $V(\mathbf{r}) \frac{\Psi(\mathbf{r}, \hat{\mathbf{r}}_i)}{\Psi^i(\mathbf{r}, \hat{\mathbf{r}}_i)}$. The spectrum of Eq. (9.1) is known as the cepstrum (pronounced "kep-strum") [Bogert, et al, 1963]. For most objects of practical interest, numerical computation of Eq. (9.1) produces a phase term that is wrapped between 0 and 2π . This phase ambiguity leads to artifacts in the cepstrum that complicate the filtering process. To remove these artifacts, phase unwrapping techniques in one-dimensional problems have been introduced [Tribolet, 1977]; however, two-dimensional phase unwrapping remains a formidable problem [Scivier, et al, 1985].

A particular transformation that avoids the phase wrapping problem mentioned above is found by computing the derivative of the logarithm of the function [Polydoros, et al, 1981]. The essential point is that the mathematical equivalent to the derivative of the logarithm

$$\frac{\frac{\delta}{\delta x} \left[V(x, y) \frac{\Psi(x, y, \phi_i)}{\Psi^i(x, y, \phi_i)} \right]}{\left[V(x, y) \frac{\Psi(x, y, \phi_i)}{\Psi^i(x, y, \phi_i)} \right]} = \frac{\frac{\delta}{\delta x} V(x, y)}{V(x, y)} + \frac{\frac{\delta}{\delta x} \frac{\Psi(x, y, \phi_i)}{\Psi^i(x, y, \phi_i)}}{\frac{\Psi(x, y, \phi_i)}{\Psi^i(x, y, \phi_i)}} \quad (9.2)$$

does not include the logarithmic operator in its definition and therefore avoids the phase ambiguity shown in Eq. (9.1).

The spectrum of Eq. (9.2) is known as the differential cepstrum and has been discussed in one dimension [Polydoros, et al, 1981], two dimensions [Raghuramireddy, et al, Oct. 1985], and multiple dimensions [Raghuramireddy, et al, Dec. 1985]. Raghuramireddy and Unbehauen [Oct. 1985] define the two-dimensional differential cepstrum as the spectrum of

$$\frac{\frac{\delta}{\delta x} \left[V(x, y) \frac{\Psi(x, y, \phi_i)}{\Psi^i(x, y, \phi_i)} \right] + \frac{\delta}{\delta y} \left[V(x, y) \frac{\Psi(x, y, \phi_i)}{\Psi^i(x, y, \phi_i)} \right]}{\left[V(x, y) \frac{\Psi(x, y, \phi_i)}{\Psi^i(x, y, \phi_i)} \right]} \quad (9.3)$$

and comment that if one desires only to avoid the phase ambiguity one can define the differential cepstrum as the spectrum of Eq. (9.2). To avoid the phase ambiguity and to simplify the inverse transformation, we define the two-dimensional differential cepstrum $dc(f_x, f_y, \phi_i)$ as the Fourier transform of Eq. (9.2)

$$dc(f_x, f_y, \phi_i) = \int_{-\infty}^{\infty} \int_{-\infty}^{\infty} \frac{\frac{\delta}{\delta x} \left[V(x, y) \frac{\Psi(x, y, \phi_i)}{\Psi^i(x, y, \phi_i)} \right]}{\left[V(x, y) \frac{\Psi(x, y, \phi_i)}{\Psi^i(x, y, \phi_i)} \right]} e^{-i [2\pi f_x x + 2\pi f_y y]} dx dy. \quad (9.4)$$

Equation (9.4) can be evaluated by using properties of Fourier transforms [Bracewell, 1965] where

$$\frac{\delta}{\delta x} \left[V(x, y) \frac{\Psi(x, y, \phi_i)}{\Psi^i(x, y, \phi_i)} \right] = \int_{-\infty}^{\infty} \int_{-\infty}^{\infty} 2\pi i f_x \tilde{V}'(f_x, f_y, \phi_i) e^{+i [2\pi f_x x + 2\pi f_y y]} df_x df_y \quad (9.5)$$

and

$$\tilde{V}'(f_x, f_y, \phi_i) \equiv \int_{-\infty}^{\infty} \int_{-\infty}^{\infty} V(x, y) \frac{\Psi(x, y, \phi_i)}{\Psi^i(x, y, \phi_i)} e^{-i [2\pi f_x x + 2\pi f_y y]} dx dy . \quad (9.6)$$

A regularization procedure is used in the computation of Eq. (9.4) because Eq. (9.2) is ill-conditioned. Specifically, zero values of $V(\mathbf{r}) \frac{\Psi(\mathbf{r}, \hat{\mathbf{r}}_i)}{\Psi^i(\mathbf{r}, \hat{\mathbf{r}}_i)}$ cause the derivative of the log shown in Eq. (9.2) to approach infinity. The regularization procedure, also known as Wiener filtering, modifies Eq. (9.2) by first multiplying both the numerator and denominator by the complex conjugate of $V(\mathbf{r}) \frac{\Psi(\mathbf{r}, \hat{\mathbf{r}}_i)}{\Psi^i(\mathbf{r}, \hat{\mathbf{r}}_i)}$

$$\frac{\frac{\delta}{\delta x} \left[V(x, y) \frac{\Psi(x, y, \phi_i)}{\Psi^i(x, y, \phi_i)} \right] \left[V(x, y) \frac{\Psi(x, y, \phi_i)}{\Psi^i(x, y, \phi_i)} \right]^*}{\left[V(x, y) \frac{\Psi(x, y, \phi_i)}{\Psi^i(x, y, \phi_i)} \right] \left[V(x, y) \frac{\Psi(x, y, \phi_i)}{\Psi^i(x, y, \phi_i)} \right]^*}, \quad (9.7)$$

where * denotes complex conjugate. Then, a small regularization parameter δ is added to the denominator yielding the regularized version of Eq. (9.2)

$$\frac{\frac{\delta}{\delta x} \left[V(x, y) \frac{\Psi(x, y, \phi_i)}{\Psi^i(x, y, \phi_i)} \right] \left[V(x, y) \frac{\Psi(x, y, \phi_i)}{\Psi^i(x, y, \phi_i)} \right]^*}{\left| V(x, y) \frac{\Psi(x, y, \phi_i)}{\Psi^i(x, y, \phi_i)} \right|^2 + \delta}. \quad (9.8)$$

The regularization parameter δ is chosen to be a small fraction of the maximum of $\left| V(x, y) \frac{\Psi(x, y, \phi_i)}{\Psi^i(x, y, \phi_i)} \right|^2$. The differential cepstrum is found to be insensitive to a wide range of values for δ .

A linear filter $L(f_x, f_y)$ is chosen to pass those frequency components associated with

$\frac{\delta}{\delta x} V(x, y, \phi_i)$ and to reject those associated with $\frac{\delta}{\delta x} \frac{\Psi(x, y, \phi_i)}{\Psi^i(x, y, \phi_i)} / \frac{\Psi(x, y, \phi_i)}{\Psi^i(x, y, \phi_i)}$. Inversion of the transformation requires the filtered differential cepstrum to be inverse Fourier transformed, integrated, and exponentiated. This inversion produces an estimate for $V(x, y)$, due to the effects of $L(f_x, f_y)$, and is written succinctly as

$$V^{est}(x, y, \phi_i) = \exp\left[\int_{-\infty}^{\infty} \int_{-\infty}^{\infty} \frac{1}{2\pi i f_x} dc(f_x, f_y, \phi_i) L(f_x, f_y) e^{+i[2\pi f_x x + 2\pi f_y y]} df_x df_y\right] \quad (9.9)$$

Successful image reconstruction depends on how well the spectra of $\frac{\delta}{\delta x} V(x, y, \phi_i)$ and $\frac{\delta}{\delta x} \frac{\Psi(x, y, \phi_i)}{\Psi^i(x, y, \phi_i)}$ separate within the differential cepstral domain. Our assumption

is that as the scattering strength increases, $\frac{\Psi(x, y, \phi_i)}{\Psi^i(x, y, \phi_i)}$ internal to the object becomes increasingly oscillatory (that is, noise-like) in all directions, but it necessarily retains a characteristic correlation length (that is, periodicity) proportional to the effective wavelength in the medium. In such cases, the spectrum of $\frac{\delta}{\delta x} \frac{\Psi(x, y, \phi_i)}{\Psi^i(x, y, \phi_i)} / \frac{\Psi(x, y, \phi_i)}{\Psi^i(x, y, \phi_i)}$ would manifest itself within a distinct annular ring in the differential cepstrum. Later, in Section 10, we use an ad-hoc procedure to choose $L(f_x, f_y)$. A more automated procedure to choose $L(f_x, f_y)$ might be devised given knowledge of the mean permittivity within the object.

10. DIFFERENTIAL CEPSTRAL FILTERING APPLIED TO EXACT $V \frac{\Psi}{\Psi^i}$

In this section, we apply differential cepstral filtering to $V(\mathbf{r}) \frac{\Psi(\mathbf{r}, \hat{\mathbf{r}}_i)}{\Psi^i(\mathbf{r}, \hat{\mathbf{r}}_i)}$ for the various cylinders shown in Figure 23, under plane wave illumination at 10 GHz. The exact field value was computed for each cylinder according to Eqs. (6.13), (6.14), and (6.15). Input $(V(\mathbf{r}) \frac{\Psi(\mathbf{r}, \hat{\mathbf{r}}_i)}{\Psi^i(\mathbf{r}, \hat{\mathbf{r}}_i)})$ to the nonlinear filter, in each case, is pristine data, free from the convolutional effects introduced by limited Fourier data.

Figure 44 shows the magnitude of $V(\mathbf{r}) \frac{\Psi(\mathbf{r}, \hat{\mathbf{r}}_i)}{\Psi^i(\mathbf{r}, \hat{\mathbf{r}}_i)}$ for obj_1.1/1.03. The radii of the inner and outer cylinders are clearly visible (the region outside the cylinder is black in Figure 44 since $V(\mathbf{r})$ is zero in free space). Note that the multiplicative factor $\frac{\Psi(\mathbf{r}, \hat{\mathbf{r}}_i)}{\Psi^i(\mathbf{r}, \hat{\mathbf{r}}_i)}$ produces the non-uniform structure shown in Figure 44. Figures 45 and 46 show the magnitude of the differential cepstrum of $V(\mathbf{r}) \frac{\Psi(\mathbf{r}, \hat{\mathbf{r}}_i)}{\Psi^i(\mathbf{r}, \hat{\mathbf{r}}_i)}$ and of $V(\mathbf{r})$, respectively, for obj_1.1/1.03. After low-pass filtering

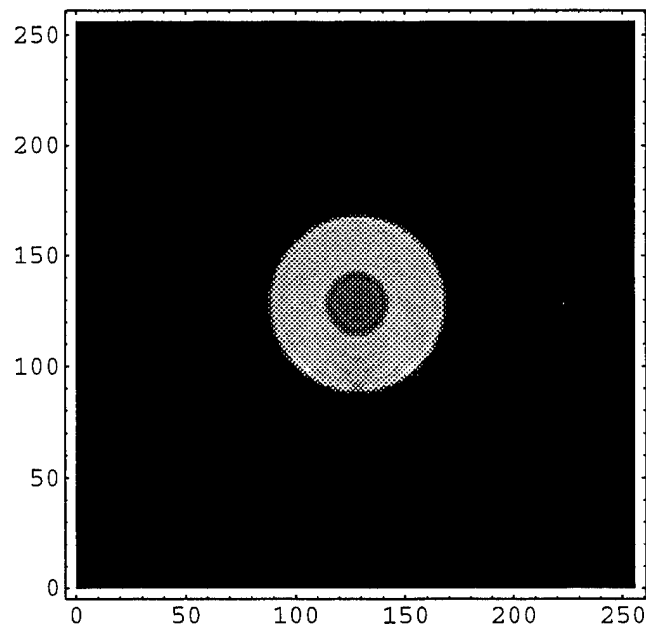


Figure 44 Exact computation of $\left| \frac{\nabla^2 \Psi}{\Psi_i} \right|$ for obj_1.1/1.03 at 10 GHz. Inner radius 3.6 cm, outer radius 9.9 cm, Field-of-view 64x64 cm².

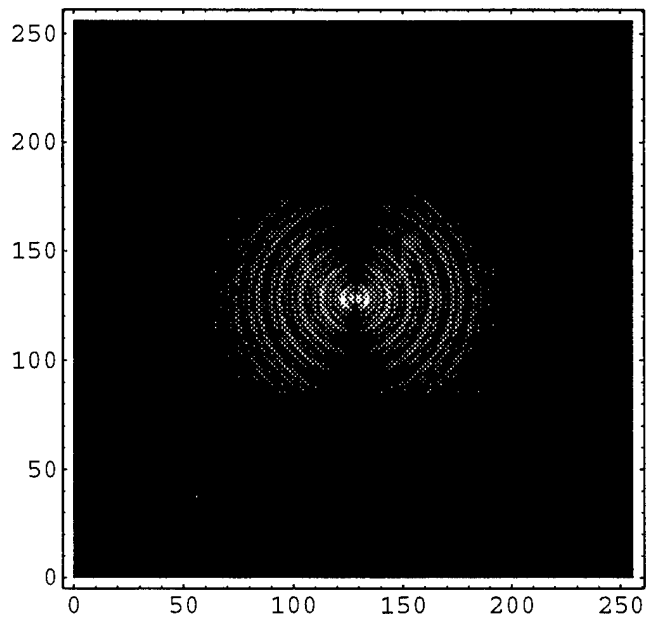


Figure 45 Magnitude of the differential cepstrum of $\frac{\nabla^2 \Psi}{\Psi_i}$ for obj_1.1/1.03.

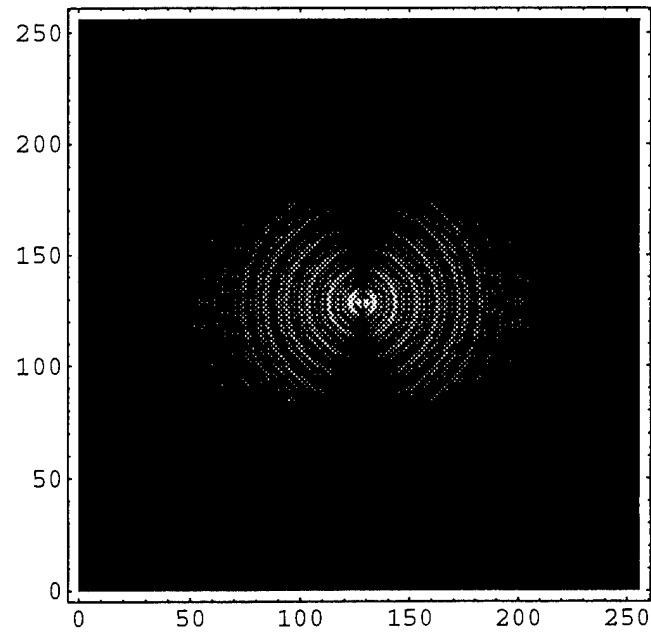


Figure 46 Magnitude of the differential cepstrum of V for obj_1.1/1.03.

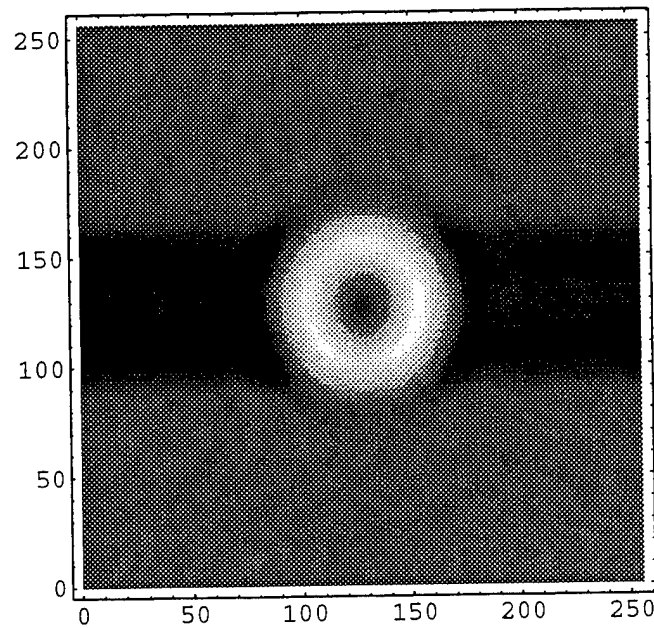


Figure 47 Magnitude of the reconstructed image of V after low pass filtering in the differential cepstral domain of obj_1.1/1.03. Field-of-view $64 \times 64 \text{ cm}^2$.

in the differential cepstrum of $V(\mathbf{r}) \frac{\Psi(\mathbf{r}, \hat{\mathbf{r}}_i)}{\Psi^i(\mathbf{r}, \hat{\mathbf{r}}_i)}$, integrating, and exponentiating, the magnitude of the reconstructed image is shown in Figure 47. Figures 48 through 51 show a similar series of plots for obj_1.03/1.1.

Isolating $V(\mathbf{r})$ from $V(\mathbf{r}) \frac{\Psi(\mathbf{r}, \hat{\mathbf{r}}_i)}{\Psi^i(\mathbf{r}, \hat{\mathbf{r}}_i)}$, in these examples, is much like the problem of finding the spatial window function $V(\mathbf{r})$ given weighted data $V(\mathbf{r}) \frac{\Psi(\mathbf{r}, \hat{\mathbf{r}}_i)}{\Psi^i(\mathbf{r}, \hat{\mathbf{r}}_i)}$. The reconstructed images in Figures 47 and 51 reveal good estimates of the data window in each case.

In Figure 52, the outer diameter of the homogeneous cylinder obj_4/4 is not clearly defined. Figures 53 and 54 show the magnitude of the differential cepstrum of $V(\mathbf{r}) \frac{\Psi(\mathbf{r}, \hat{\mathbf{r}}_i)}{\Psi^i(\mathbf{r}, \hat{\mathbf{r}}_i)}$ and $V(\mathbf{r})$, respectively, for obj_4/4. The field within the dielectric cylinder is focused in some regions and is quite small in others. The data in Figure 52 could have been generated by some other $V'(\mathbf{r}) \frac{\Psi'(\mathbf{r}, \hat{\mathbf{r}}_i)}{\Psi'^i(\mathbf{r}, \hat{\mathbf{r}}_i)}$ such that $V(\mathbf{r}) \neq V'(\mathbf{r})$ and $\frac{\Psi(\mathbf{r}, \hat{\mathbf{r}}_i)}{\Psi^i(\mathbf{r}, \hat{\mathbf{r}}_i)} \neq \frac{\Psi'(\mathbf{r}, \hat{\mathbf{r}}_i)}{\Psi'^i(\mathbf{r}, \hat{\mathbf{r}}_i)}$. Therefore, the inverse problem of finding $V(\mathbf{r})$ cannot have a unique solution. Nevertheless, after low-pass filtering in the differential cepstral domain of $V(\mathbf{r}) \frac{\Psi(\mathbf{r}, \hat{\mathbf{r}}_i)}{\Psi^i(\mathbf{r}, \hat{\mathbf{r}}_i)}$, integrating, and exponentiating, the reconstructed image of $V(\mathbf{r})$ is shown in Figure 55.

A sequence of similar plots is shown for obj_4/2 and obj_2/4 in Figures 56 through 63. Although a unique reconstruction of $V(\mathbf{r})$ cannot be guaranteed in each case, the preceding examples do recover a good estimate of the spatial window function.

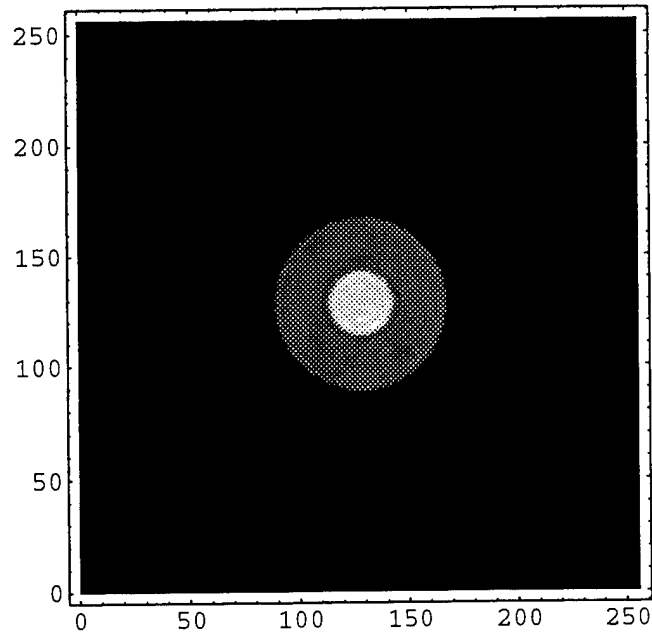


Figure 48 Exact computation of $\left| \frac{\nabla^2 \Psi}{\Psi_i} \right|$ for obj_1.03/1.1 at 10 GHz. Inner radius 3.6 cm, outer radius 9.9 cm, Field-of-view 64x64 cm².

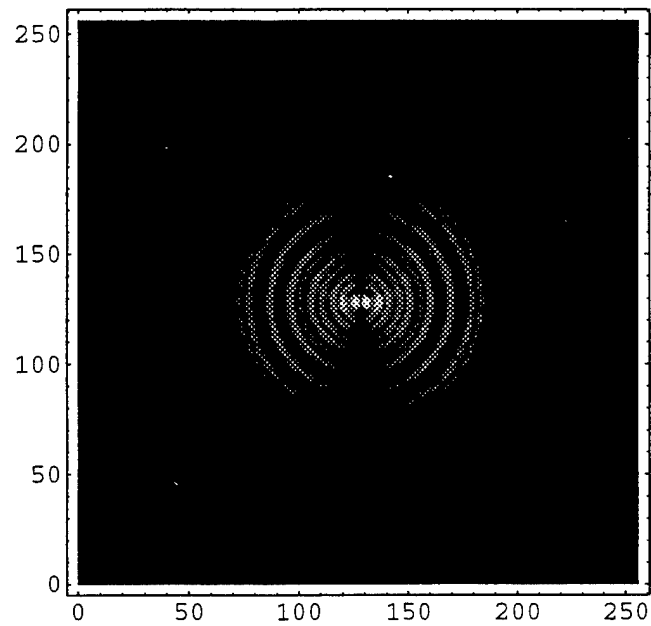


Figure 49 Magnitude of the differential cepstrum of $\frac{\nabla^2 \Psi}{\Psi_i}$ for obj_1.03/1.1.

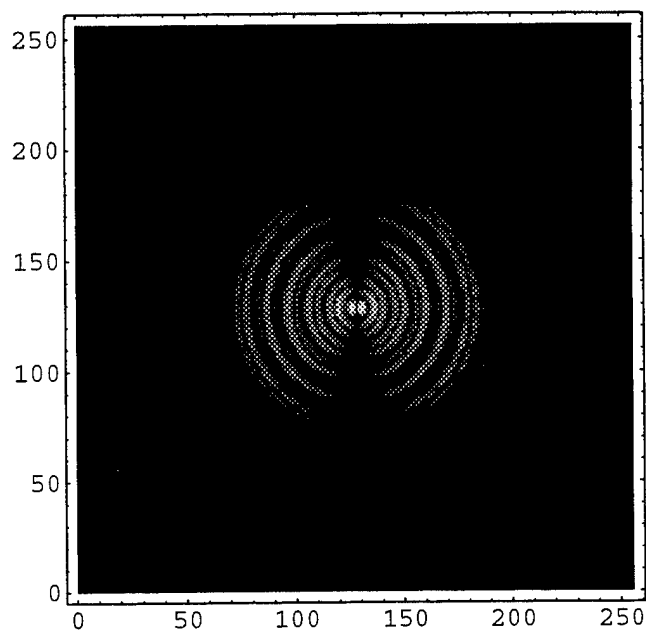


Figure 50 Magnitude of the differential cepstrum of V for obj_1.03/1.1.

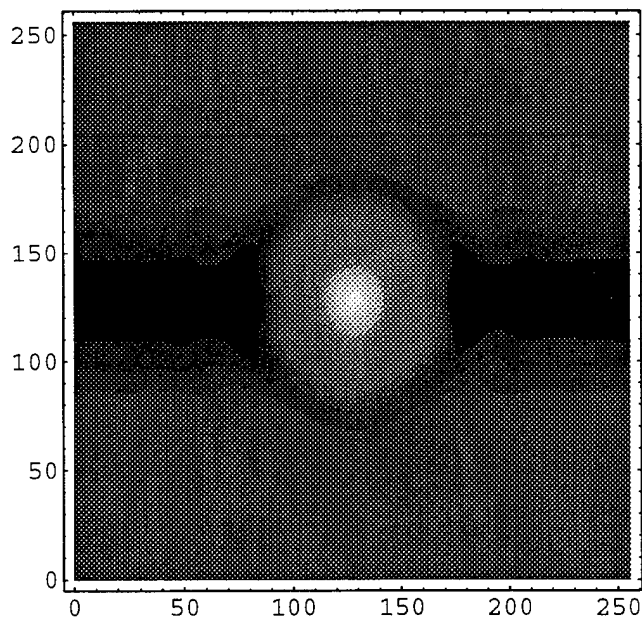


Figure 51 Magnitude of the reconstructed image of V after low pass filtering in the differential cepstral domain of obj_1.03/1.1. Field-of-view $64 \times 64 \text{ cm}^2$.

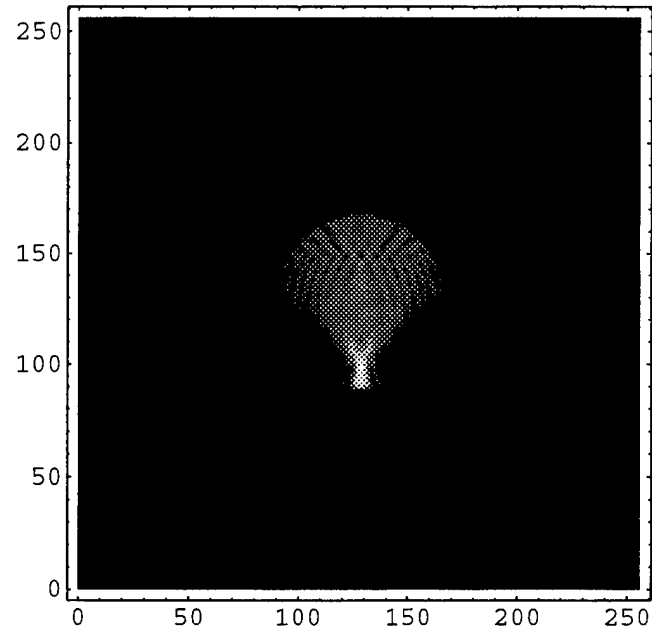


Figure 52 Exact computation of $\left| \frac{\nabla^2 \Psi}{\Psi_i} \right|$ for obj_4/4 at 10 GHz. Inner radius 3.6 cm, outer radius 9.9 cm, Field-of-view 64x64 cm².

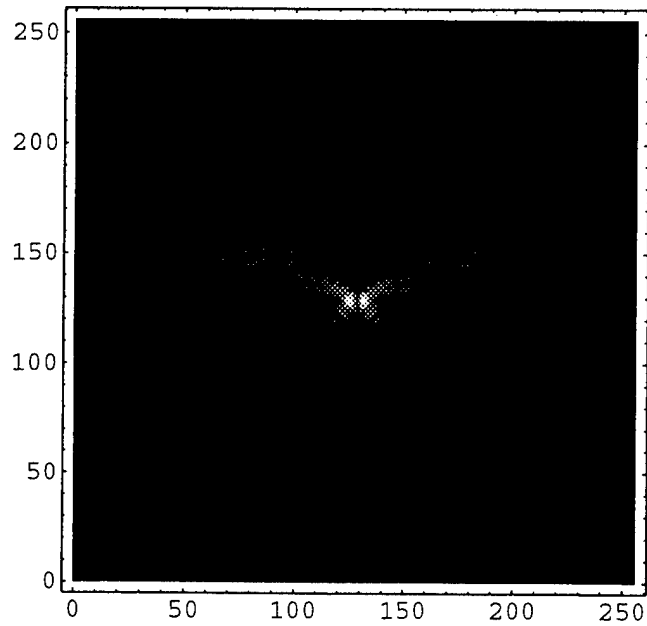


Figure 53 Magnitude of the differential cepstrum of $\frac{\nabla^2 \Psi}{\Psi_i}$ for obj_4/4.

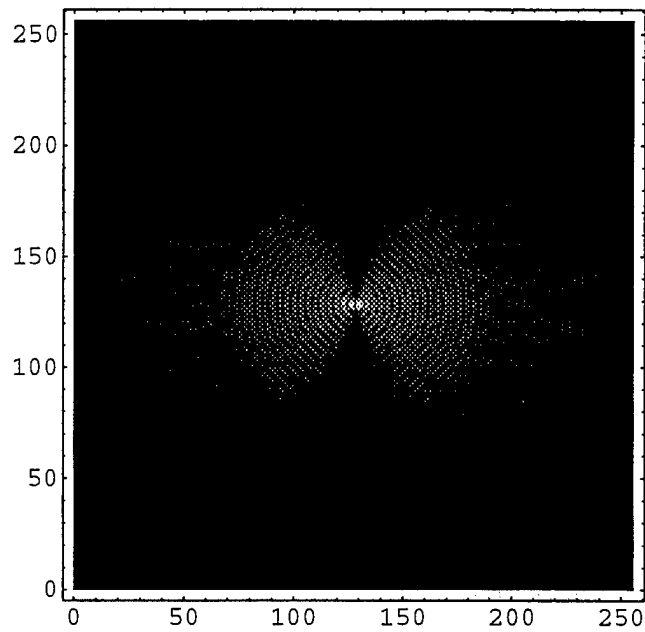


Figure 54 Magnitude of the differential cepstrum of V for obj_4/4.

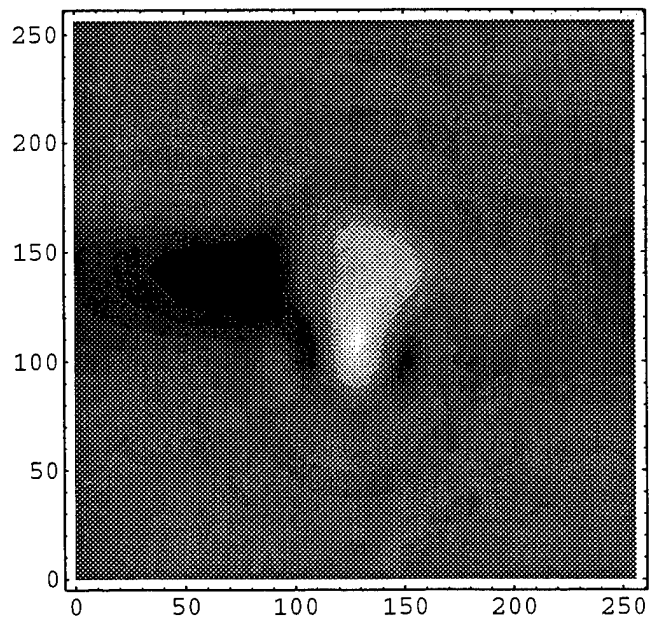


Figure 55 Magnitude of the reconstructed image of V after low pass filtering in the differential cepstral domain of obj_4/4. Field-of-view $64 \times 64 \text{ cm}^2$.

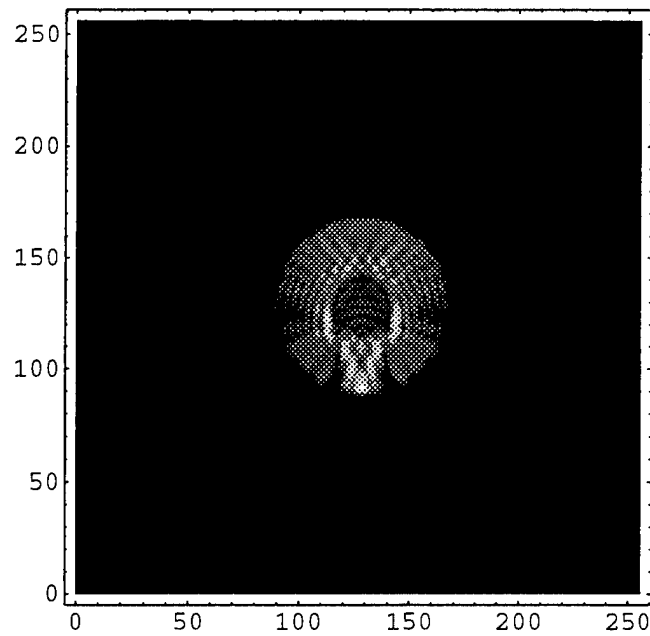


Figure 56 Exact computation of $\left| \frac{\nabla^2 \Psi}{\Psi_i} \right|$ for obj_4/2 at 10 GHz. Inner radius 3.6 cm, outer radius 9.9 cm, Field-of-view 64x64 cm².

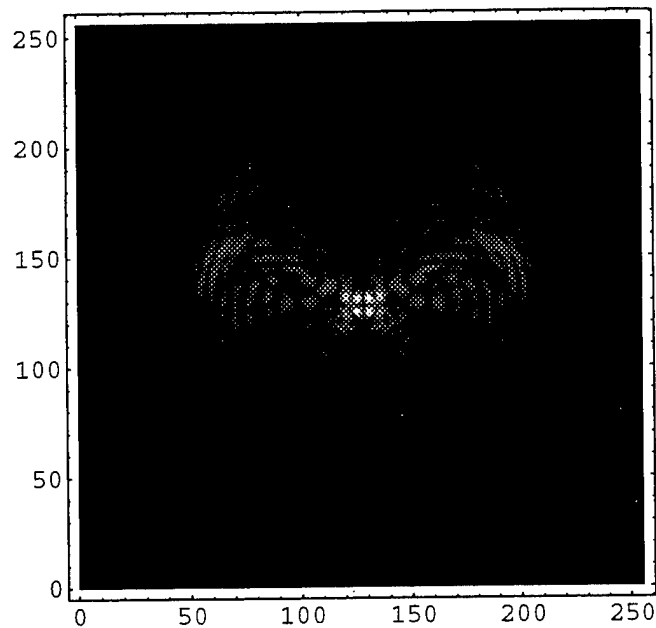


Figure 57 Magnitude of the differential cepstrum of $\frac{\nabla^2 \Psi}{\Psi_i}$ for obj_4/2.

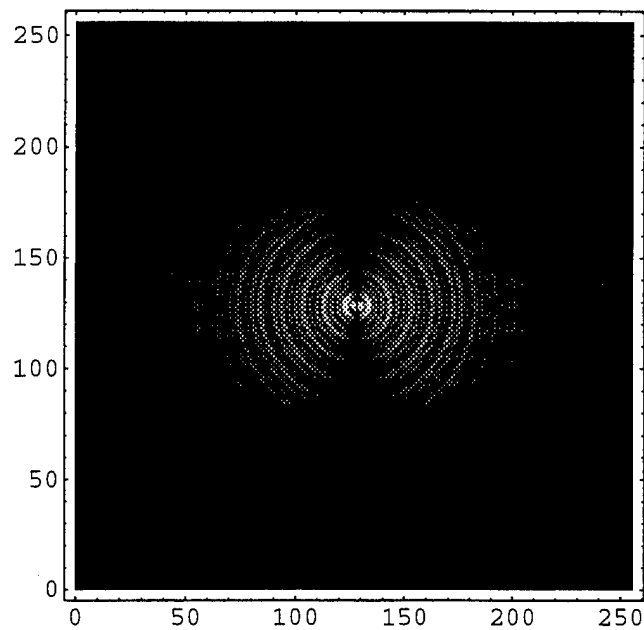


Figure 58 Magnitude of the differential cepstrum of V for obj_4/2.

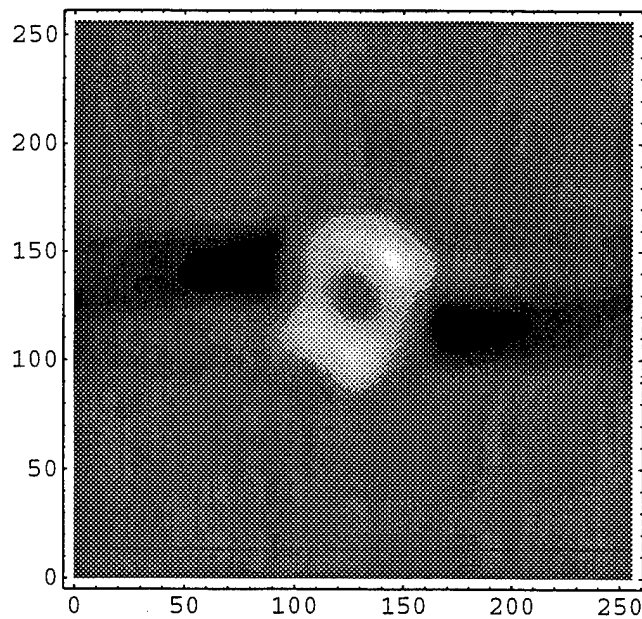


Figure 59 Magnitude of the reconstructed image of V after low pass filtering in the differential cepstral domain of obj_4/2. Field-of-view $64 \times 64 \text{ cm}^2$.

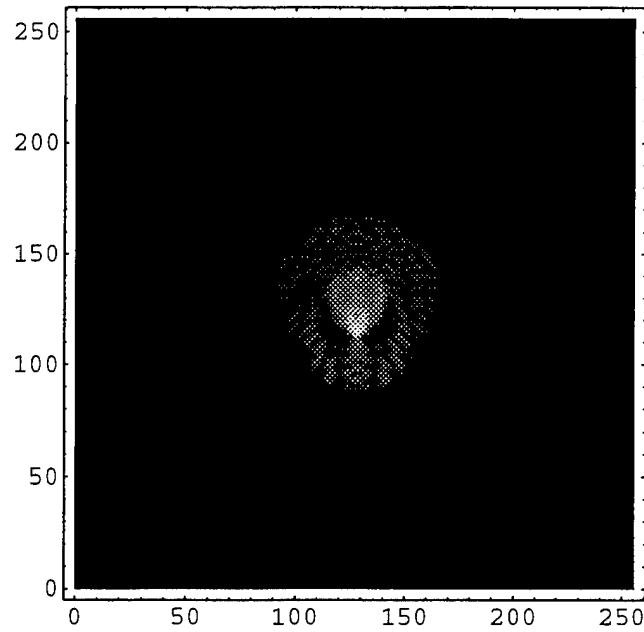


Figure 60 Exact computation of $\left| \frac{\nabla^2 \Psi}{\Psi_i} \right|$ for obj_2/4 at 10 GHz. Inner radius 3.6 cm, outer radius 9.9 cm, Field-of-view 64x64 cm².

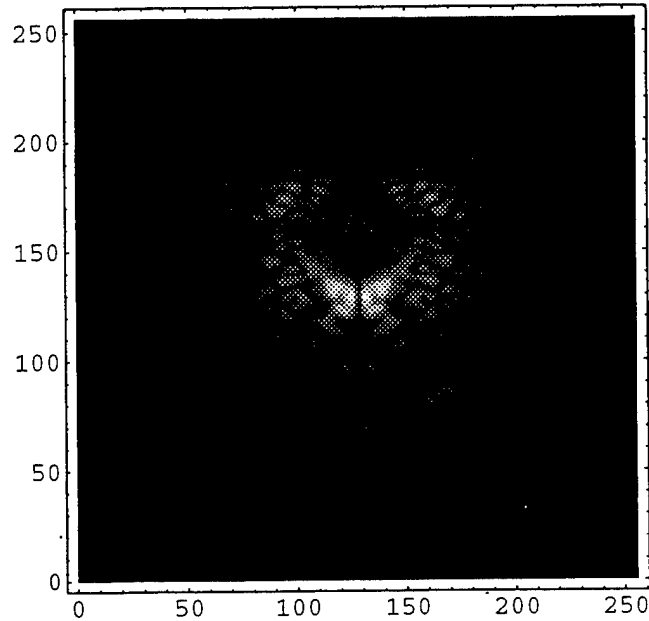


Figure 61 Magnitude of the differential cepstrum of $\frac{\nabla^2 \Psi}{\Psi_i}$ for obj_2/4.

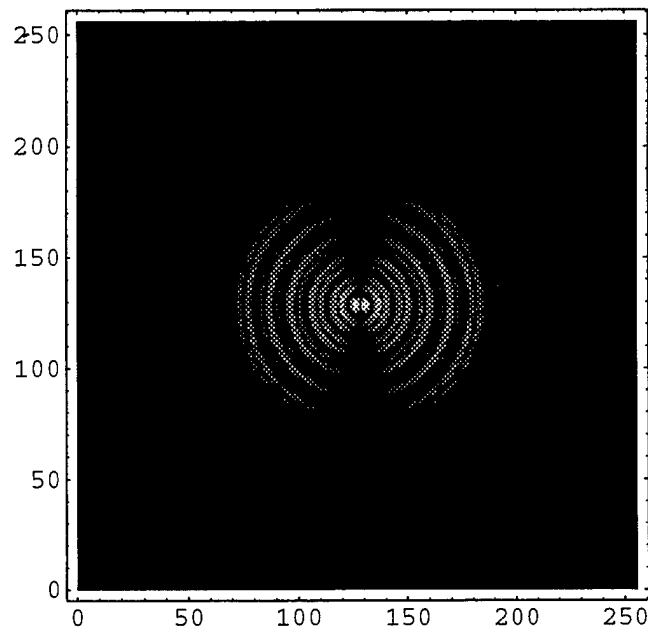


Figure 62 Magnitude of the differential cepstrum of V for obj_2/4.

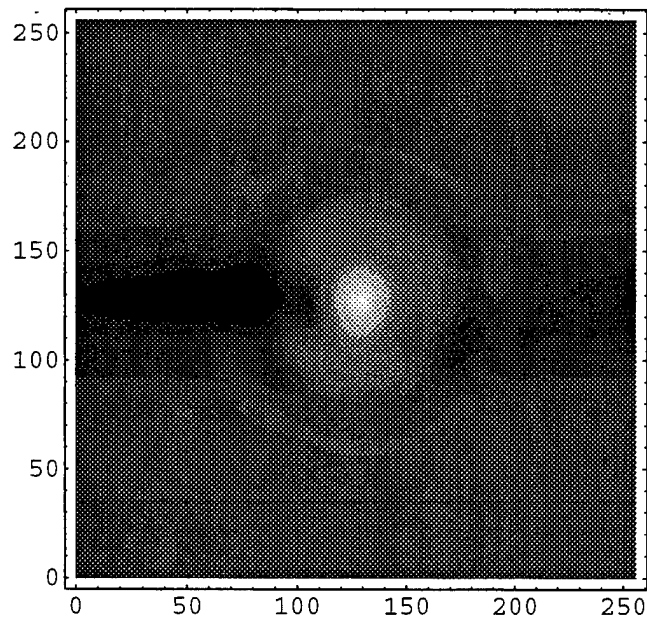


Figure 63 Magnitude of the reconstructed image of V after low pass filtering in the differential cepstral domain of obj_2/4. Field-of-view $64 \times 64 \text{ cm}^2$.

11. DIFFERENTIAL CEPSTRAL FILTERING APPLIED TO SINGLE-VIEW

BACKPROPAGATED $V \frac{\Psi}{\Psi^i} ** h_{sv}$

In this section, the differential cepstral filtering technique is applied to single-view backpropagated images of $V(\mathbf{r}) \frac{\Psi(\mathbf{r}, \hat{\mathbf{r}}_i)}{\Psi^i(\mathbf{r}, \hat{\mathbf{r}}_i)} ** h_{sv}(\mathbf{r}, \hat{\mathbf{r}}_i)$ for the five concentric cylinders shown in Figure 23. All cylinders are illuminated with a 10 GHz plane wave.

Figure 64 shows the magnitude of the single-view backpropagated image for obj_1.1/1.03. Comparing it to Figure 44, we see that the point spread function $h_{sv}(\mathbf{r}, \hat{\mathbf{r}}_i)$ has a dramatic effect on the backpropagated image shown in Figure 64. The image extends well beyond the cylinder boundary due to the side lobes associated with $h_{sv}(\mathbf{r}, \hat{\mathbf{r}}_i)$. The magnitude of the differential cepstrum of $V(\mathbf{r}) \frac{\Psi(\mathbf{r}, \hat{\mathbf{r}}_i)}{\Psi^i(\mathbf{r}, \hat{\mathbf{r}}_i)} ** h_{sv}(\mathbf{r}, \hat{\mathbf{r}}_i)$ for obj_1.1/1.03 is shown in Figure 65.

The reconstructed image after low-pass filtering in the differential cepstrum of

$V(\mathbf{r}) \frac{\Psi(\mathbf{r}, \hat{\mathbf{r}}_i)}{\Psi^i(\mathbf{r}, \hat{\mathbf{r}}_i)} ** h_{sv}(\mathbf{r}, \hat{\mathbf{r}}_i)$, integration, and exponentiation is shown in Figure 66. The

combination of 15 equally spaced filtered images is displayed in Figure 67; to speed the computation, the data were thinned by taking one point of each four. Figures 68 through 71 show a similar set of plots for obj_1.03/1.1.

Results for the more strongly scattering objects (obj_4/4, obj_4/2, and obj_2/4) are shown in Figures 72 through 83. For each single-view backpropagated image, a low-pass filter was applied in the differential cepstral domain. Although the reconstructed images for obj_1.1/1.03, obj_1.03/1.1, and obj_4/2 bear some resemblance to their original scattering potentials, the results for obj_4/4 and obj_2/4 show that a simple low-pass filter in the differential cepstral domain is not always adequate for isolating $V(\mathbf{r})$ from single-view backpropagated images of

$V(\mathbf{r}) \frac{\Psi(\mathbf{r}, \hat{\mathbf{r}}_i)}{\Psi^i(\mathbf{r}, \hat{\mathbf{r}}_i)} ** h_{sv}(\mathbf{r}, \hat{\mathbf{r}}_i)$ for strongly scattering objects.

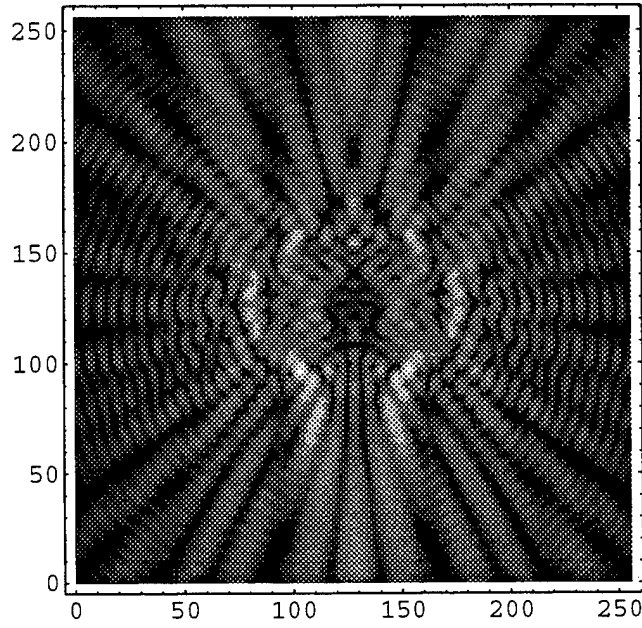


Figure 64 Magnitude of single-view backpropagated image $\left(\frac{\nabla\Psi}{\Psi^i} ** h\right)$ for obj_1.1/1.03. Field-of-view 64x64 cm².

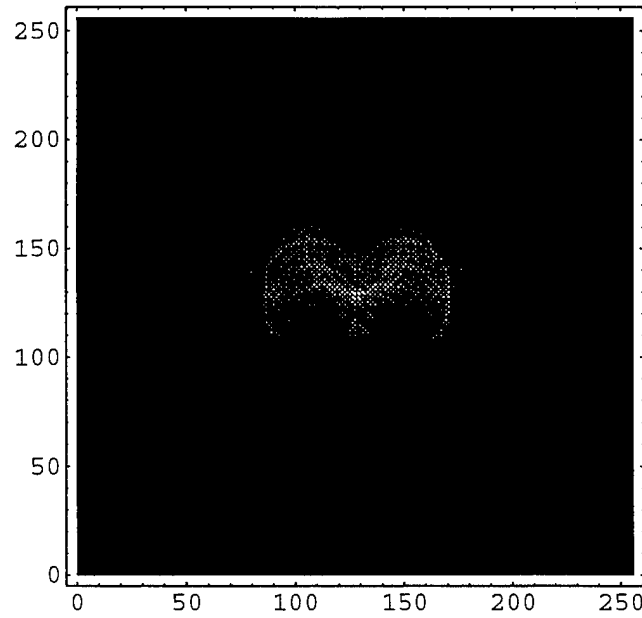


Figure 65 Magnitude of the differential cepstrum of $\frac{\nabla\Psi}{\Psi^i} ** h$ for obj_1.1/1.03.

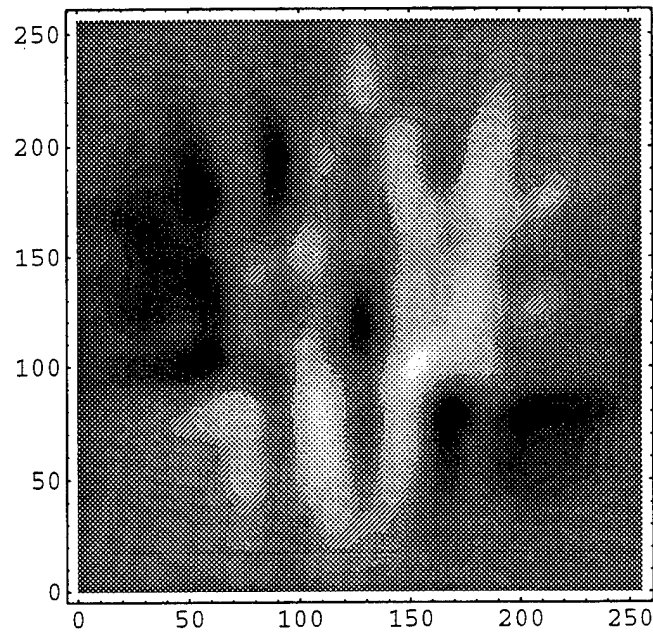


Figure 66 Magnitude of the reconstructed image of V after low pass filtering in the differential cepstral domain of obj_1.1/1.03. Field-of-view $64 \times 64 \text{ cm}^2$.

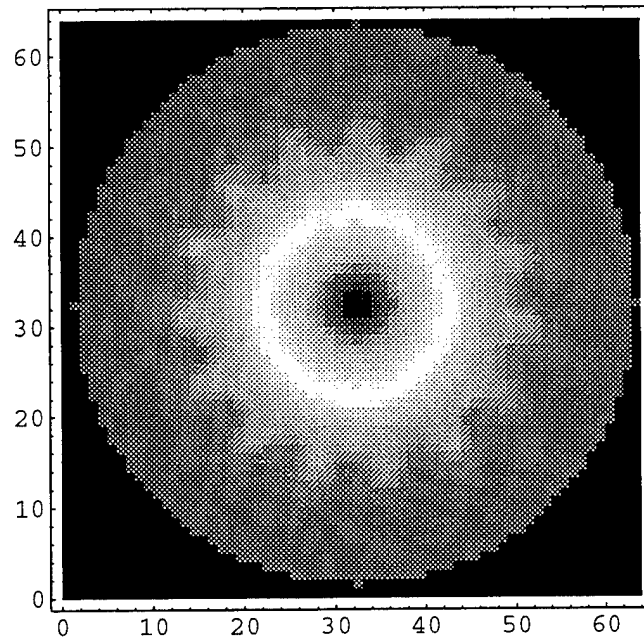


Figure 67 Magnitude of the image in Figure 66 averaged over 15 equally spaced views. Field-of-view $64 \times 64 \text{ cm}^2$.

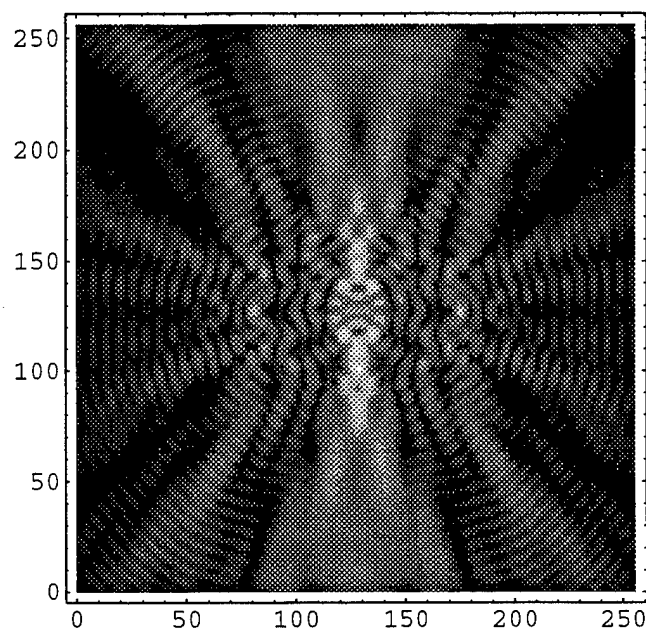


Figure 68 Magnitude of single-view backpropagated image $\left(\frac{\nabla\Psi}{\Psi^i} ** h\right)$ for obj_1.03/1.1. Field-of-view 64x64 m².

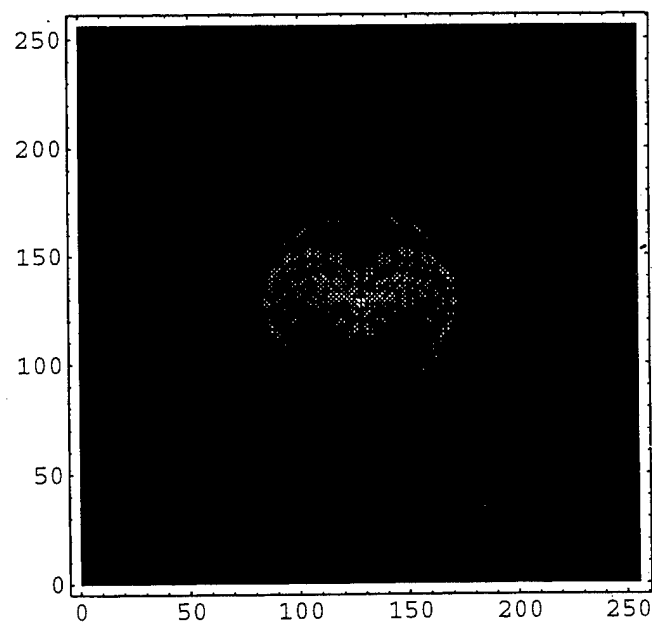


Figure 69 Magnitude of the differential cepstrum of $\frac{\nabla\Psi}{\Psi^i} ** h$ for obj_1.03/1.1.

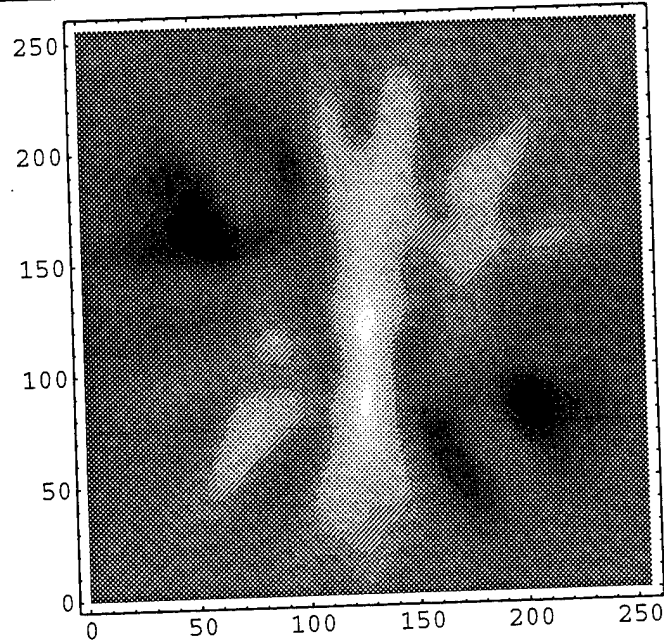


Figure 70 Magnitude of the reconstructed image of V after low pass filtering in the differential cepstral domain of obj_1.03/1.1. Field-of-view $64 \times 64 \text{ cm}^2$.

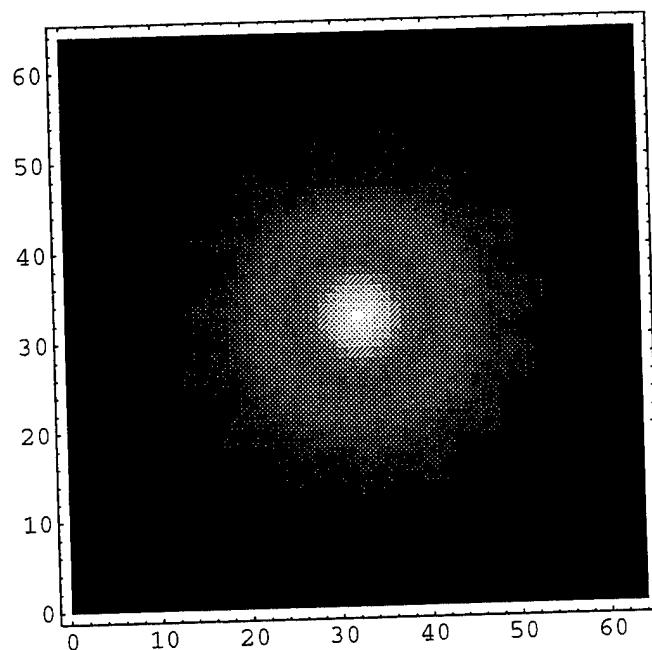


Figure 71 Magnitude of the image in Figure 70 averaged over 15 equally spaced views. Field-of-view $64 \times 64 \text{ cm}^2$.

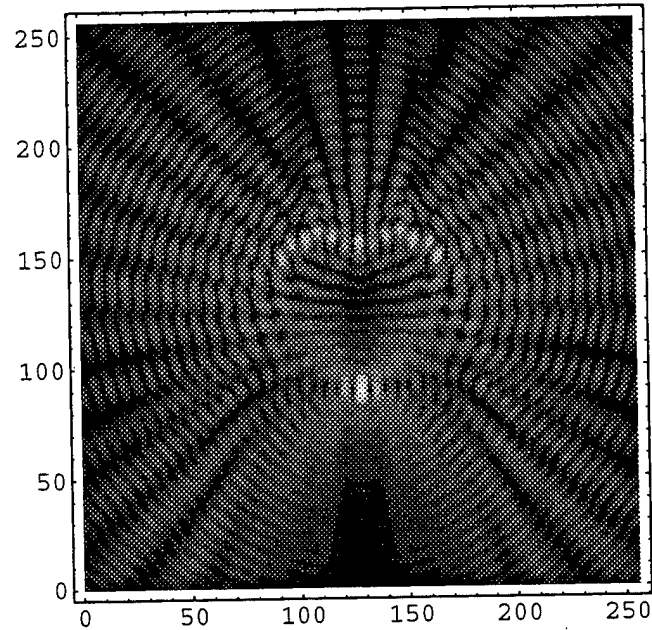


Figure 72 Magnitude of single-view backpropagated image $\left(\frac{\nabla\Psi}{\Psi^i} ** h\right)$ for obj_4/4.
Field-of-view 64x64 cm².

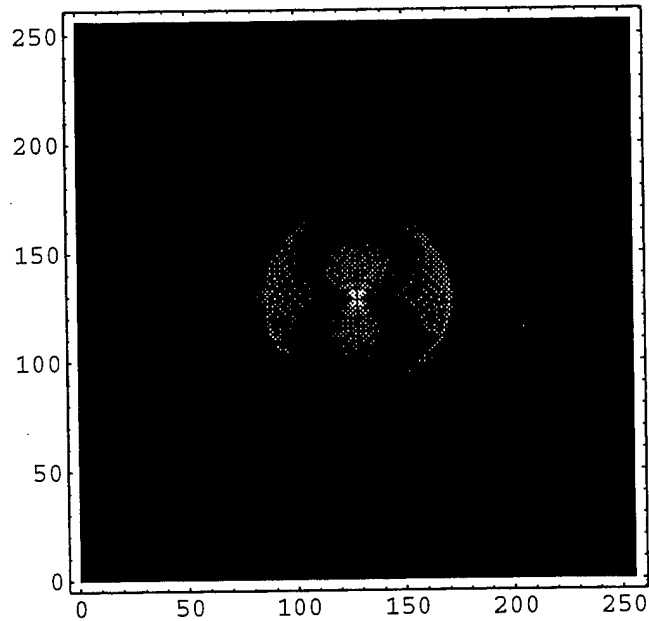


Figure 73 Magnitude of the differential cepstrum of $\frac{\nabla\Psi}{\Psi^i} ** h$ for obj_4/4.

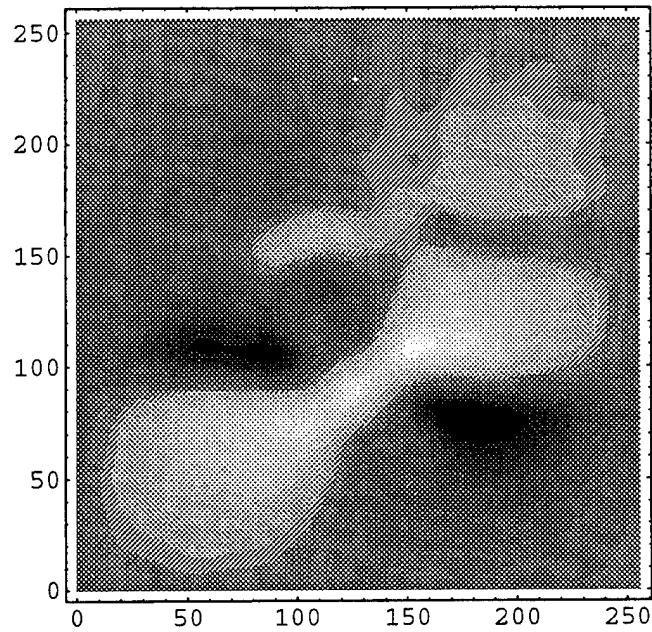


Figure 74 Magnitude of the reconstructed image of V after low pass filtering in the differential cepstral domain of obj_4/4. Field-of-view $64 \times 64 \text{ cm}^2$.

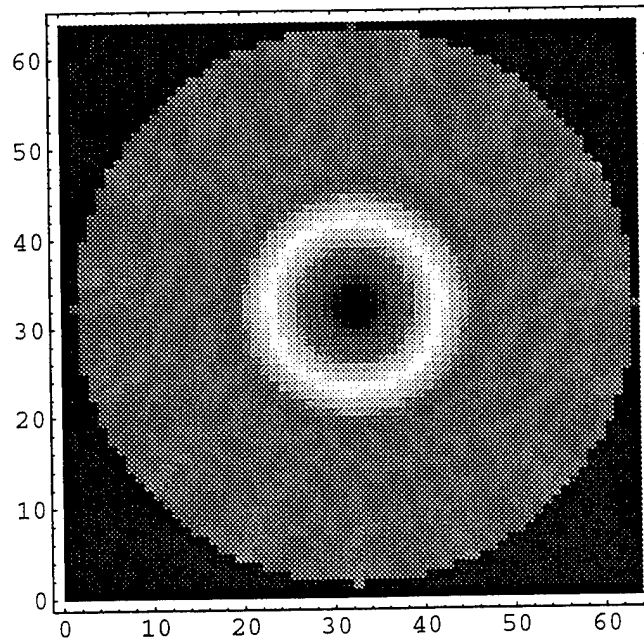


Figure 75 Magnitude of the image in Figure 74 averaged over 15 equally spaced views. Field-of-view $64 \times 64 \text{ cm}^2$.

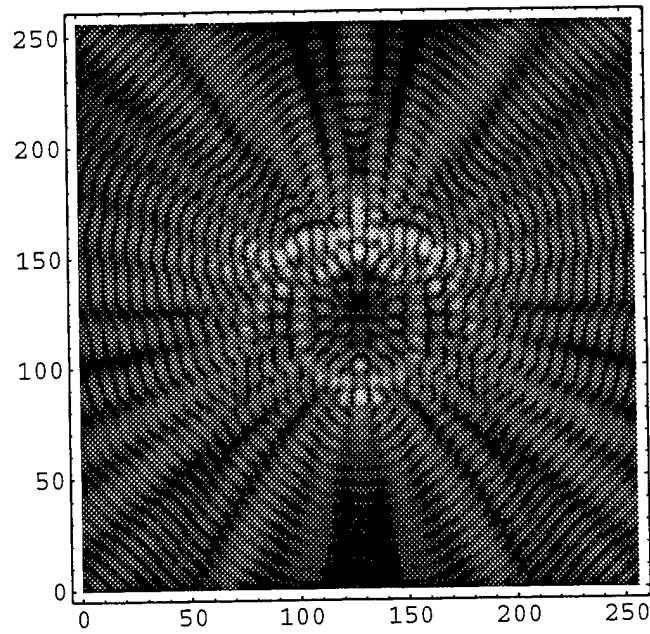


Figure 76 Magnitude of single-view backpropagated image $\left(\frac{\nabla\Psi}{\Psi^i} ** h\right)$ for obj_4/2.
Field-of-view 64x64 cm².

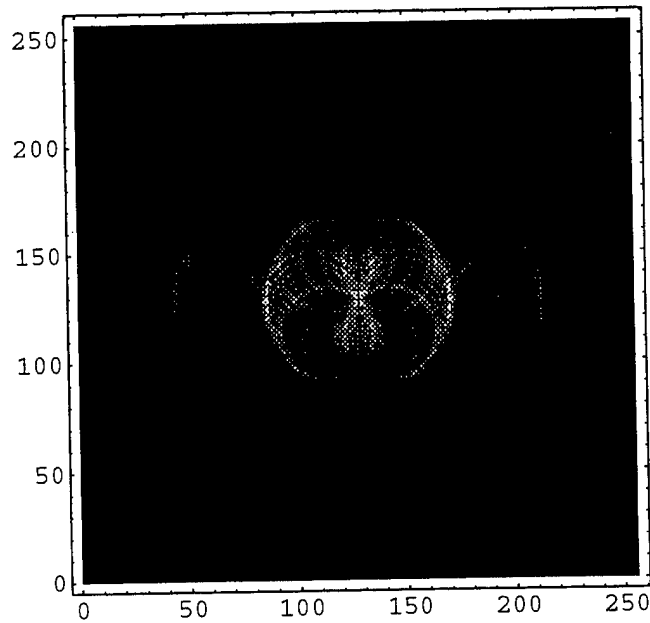


Figure 77 Magnitude of the differential cepstrum of $\frac{\nabla\Psi}{\Psi^i} ** h$ for obj_4/2.

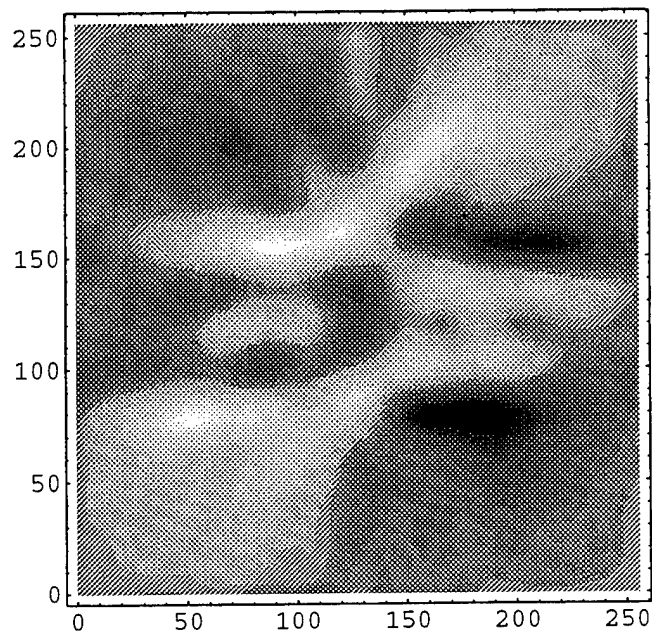


Figure 78 Magnitude of the reconstructed image of V after low pass filtering in the differential cepstral domain of obj_4/2. Field-of-view $64 \times 64 \text{ cm}^2$.

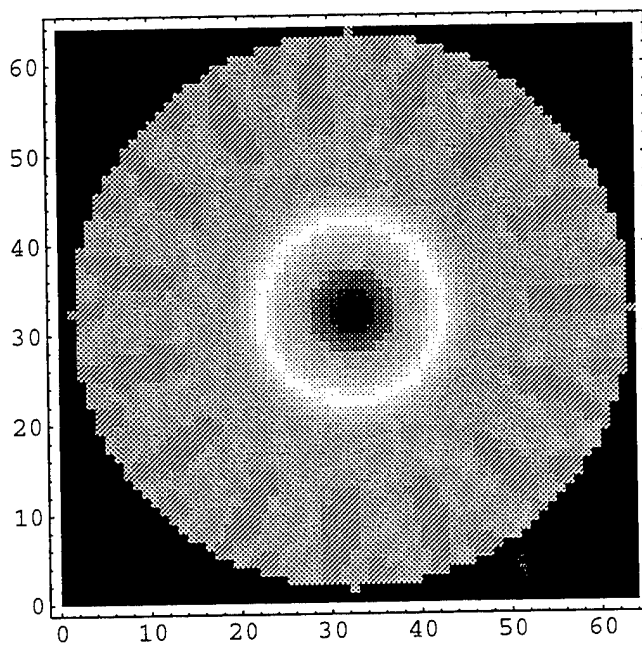


Figure 79 Magnitude of the image in Figure 78 averaged over 15 equally spaced views. Field-of-view $64 \times 64 \text{ cm}^2$.

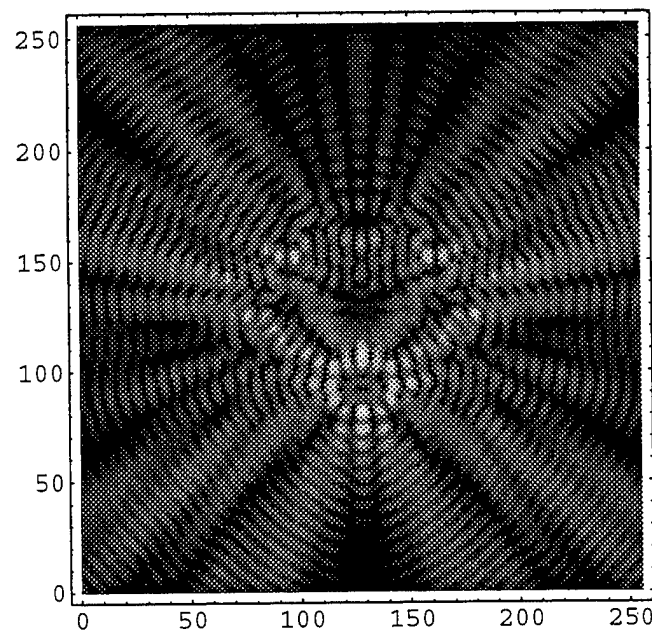


Figure 80 Magnitude of single-view backpropagated image $\left(\frac{\nabla\Psi}{\Psi^i} ** h\right)$ for obj_2/4.
Field-of-view 64x64 cm².

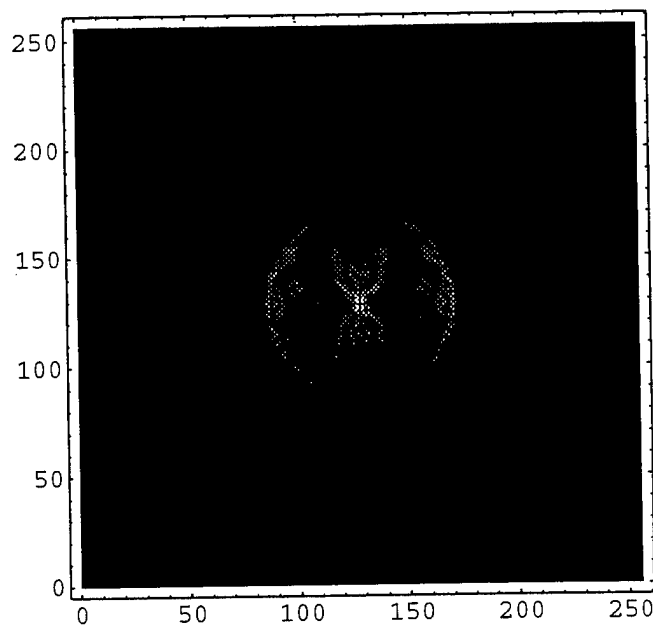


Figure 81 Magnitude of the differential cepstrum of $\frac{\nabla\Psi}{\Psi^i} ** h$ for obj_2/4.

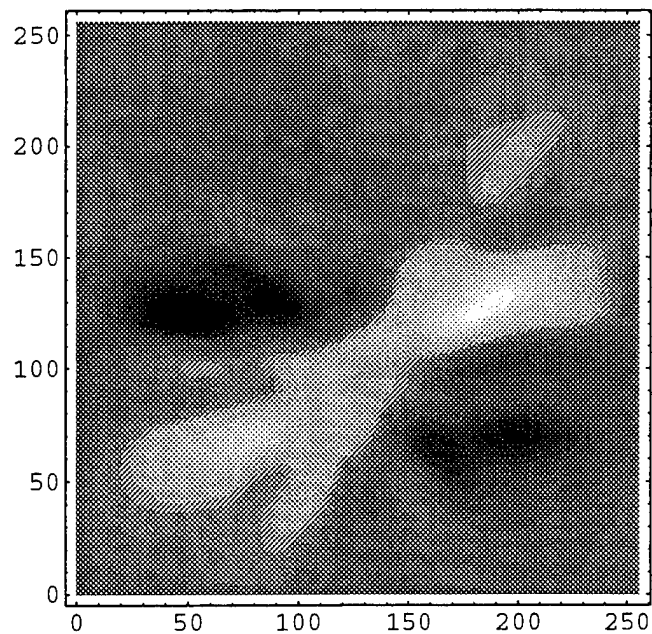


Figure 82 Magnitude of the reconstructed image of V after low pass filtering in the differential cepstral domain of obj_2/4. Field-of-view $64 \times 64 \text{ cm}^2$.

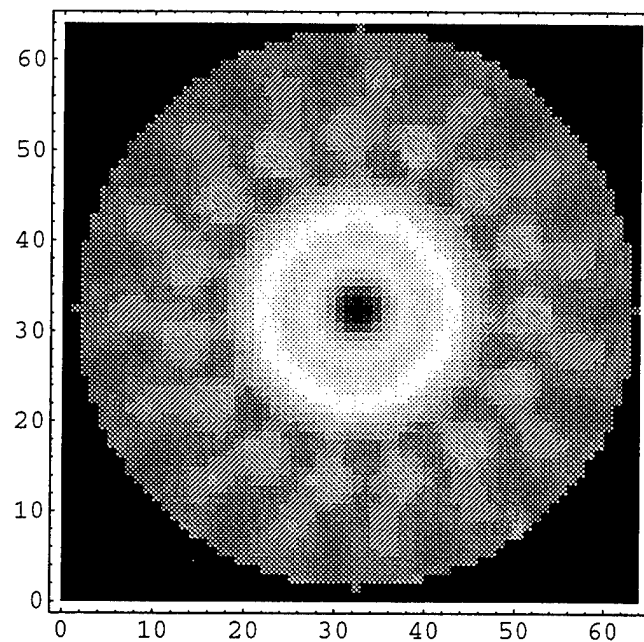


Figure 83 Magnitude of the image in Figure 82 averaged over 15 equally spaced views. Field-of-view $64 \times 64 \text{ cm}^2$.

12. DIFFERENTIAL CEPSTRAL FILTERING APPLIED TO SINGLE-VIEW BACKPROPAGATED $V \frac{\Psi}{\Psi^i}$ USING A PRIORI KNOWLEDGE OF THE OBJECT'S SUPPORT

In this section, the differential cepstral filtering routine is applied to the single-view backpropagated images introduced in Section 11; however, a priori information of the object's support is used. For each image, data outside the physical support of the object are zeroed. The process of eliminating data outside the object support is referred to as truncation. Lastly, we consider the effects of random noise on the backpropagated image of obj_4/2 and show a single-view filtered reconstruction of the scattering potential in the presence of this noise.

Figure 84 displays the truncated magnitude of the single-view backpropagated image of obj_1.1/1.03. The magnitude of its differential cepstrum is shown in Figure 85. Using a low-pass filter in the differential cepstral domain, we recover an estimate of V as shown in Figure 86. The filtered single-view image of Figure 86 is superior to the unfiltered image shown in Figure 64. Filtered estimates of V obtained from 15 equally spaced views are averaged in Figure 87. This post-filtering average produces a more symmetric estimate of the scattering potential.

The magnitude of the truncated single-view backpropagated image of obj_1.03/1.1 is shown in Figure 88, and its differential cepstrum is shown in Figure 89. After low-pass filtering in the differential cepstral domain, the reconstructed image is shown in Figure 90, where the estimate of V is superior to the unfiltered single-view backpropagated image shown in Figure 68. Figure 91 shows the magnitude of the reconstructed image averaged over 15 equally spaced illumination directions. The image of Figure 91 agrees qualitatively with the original scattering potential.

Similar plots are shown for obj_4/4, obj_4/2, and obj_2/4 in Figures 92 through 103 for these cases. The magnitudes of the reconstructed images all appear similar. The scattered far-field data from these strongly scattering objects are in fact quite different as illustrated in Appendix C. Features within these more strongly scattering objects are not well resolved due to the limited Fourier data available. Although the image of obj_4/2, shown in Figure 98, agrees qualitatively with the original scattering potential, a consistent solution is not obtained for the other two objects as illustrated in Figures 94 and 102.

Since measured data invariably contain some level of noise, we examine its effect on the differential cepstral filtering technique. A random component (uniform distribution) was added to both the real and imaginary parts of the simulated scattered field for obj_4/2. In Figures 104 through 107, the magnitudes of the single-view backpropagated images are shown for signal to noise (S/N) ratios of 20, 15, 10, and 5 dB, respectively. Figure 108 shows the magnitude of the

differential cepstrum of $V \frac{\Psi}{\Psi^i} ** h$ for obj_4/2 with S/N=20 dB. *A priori* knowledge of the object support was incorporated in generating Figure 108. Finally, the magnitude of the reconstructed image of V , after low-pass filtering in the differential cepstral domain, is shown in

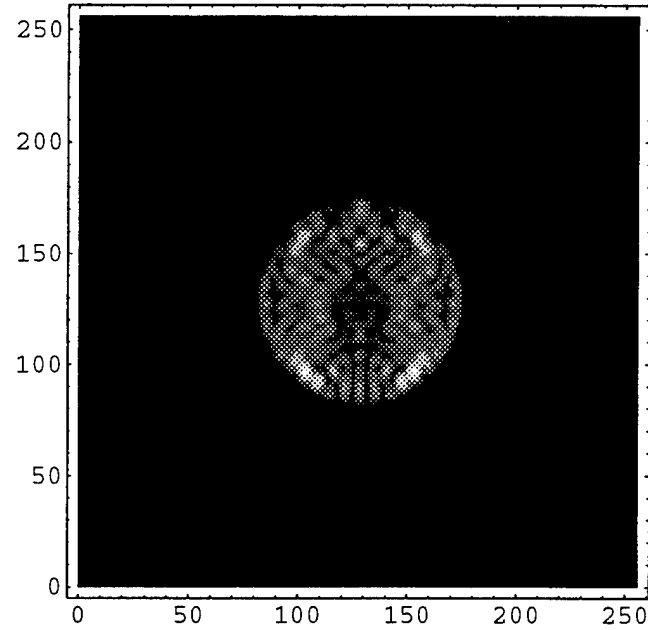


Figure 84 Magnitude of single-view backpropagated image $\left(\frac{\nabla\Psi}{\Psi^i} ** h\right)$ for obj_1.1/1.03 using *a priori* knowledge of object support. Field-of-view 64x64 cm².

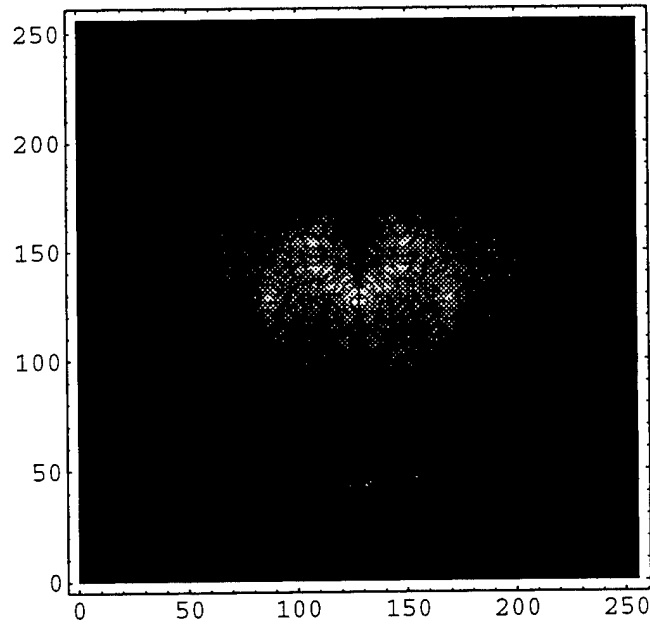


Figure 85 Magnitude of the differential cepstrum of $\frac{\nabla\Psi}{\Psi^i} ** h$ for obj_1.1/1.03 using *a priori* knowledge of object support.

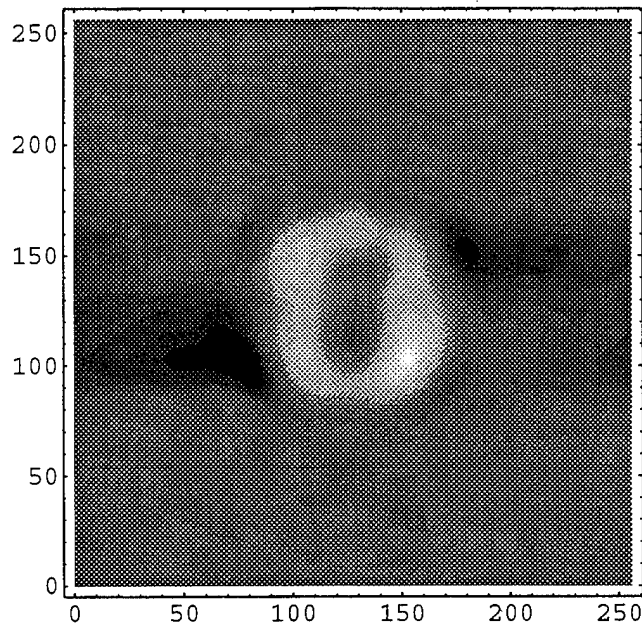


Figure 86 Magnitude of the reconstructed image of V after low pass filtering in the differential cepstral domain of obj_1.1/1.03 (using *a priori* knowledge of object support). Field-of-view $64 \times 64 \text{ cm}^2$.

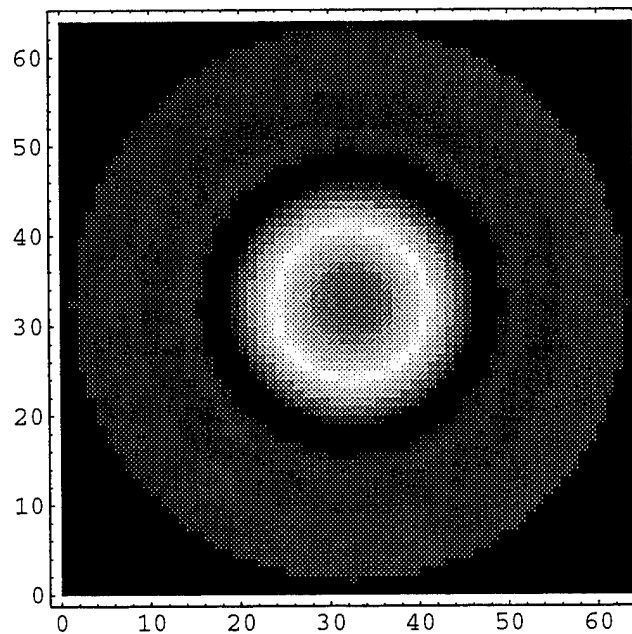


Figure 87 Magnitude of the image in Figure 86 averaged over 15 equally spaced views. Field-of-view $64 \times 64 \text{ cm}^2$.

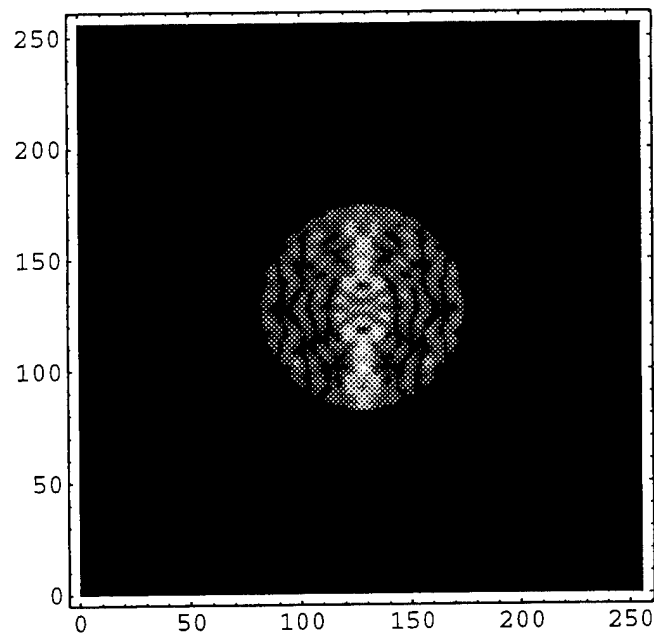


Figure 88 Magnitude of single-view backpropagated image $\left(\frac{\mathcal{V}\Psi}{\Psi^i} ** h\right)$ for obj_1.03/1.1 using *a priori* knowledge of object support. Field-of-view 64x64 cm².

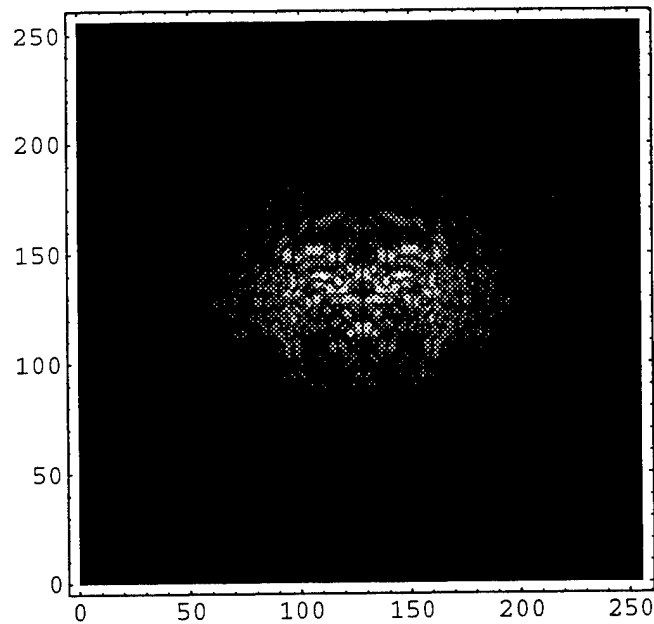


Figure 89 Magnitude of the differential cepstrum of $\frac{\mathcal{V}\Psi}{\Psi^i} ** h$ for obj_1.03/1.1 using *a priori* knowledge of object support.

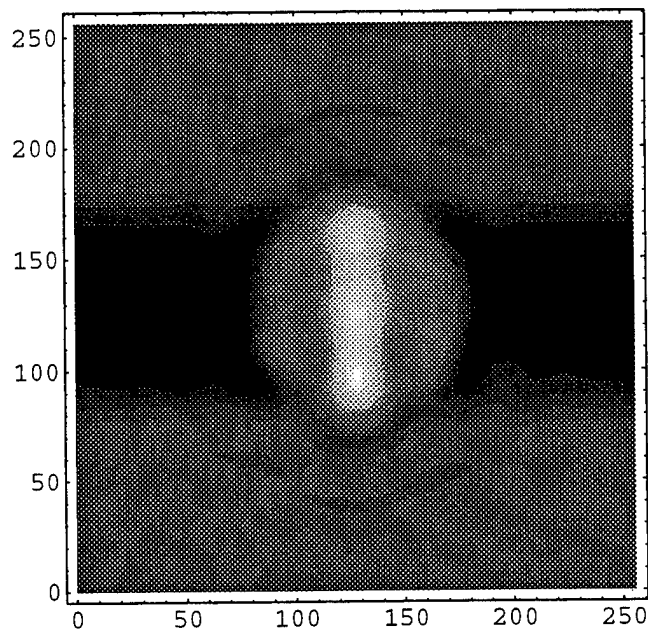


Figure 90 Magnitude of the reconstructed image of V after low pass filtering in the differential cepstral domain of obj_1.03/1.1 (using *a priori* knowledge of object support). Field-of-view $64 \times 64 \text{ cm}^2$.

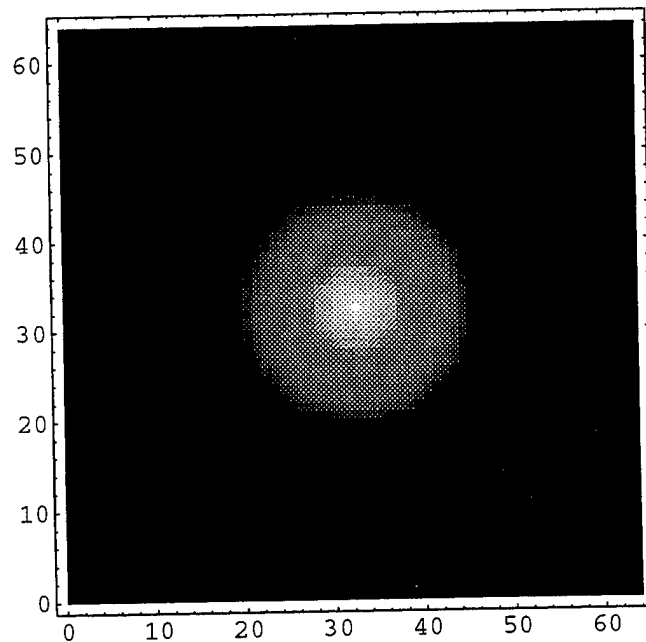


Figure 91 Magnitude of the image in Figure 90 averaged over 15 equally spaced views. Field-of-view $64 \times 64 \text{ cm}^2$.

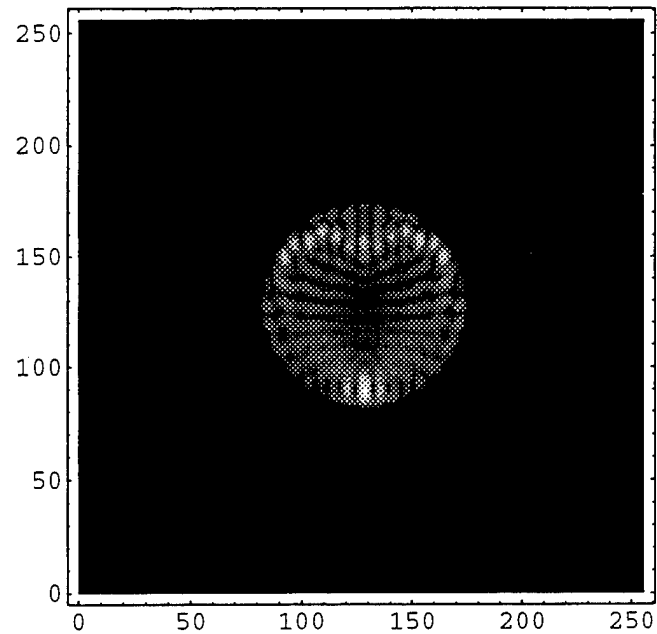


Figure 92 Magnitude of single-view backpropagated image $\left(\frac{\mathcal{V}\Psi}{\Psi^i} ** h\right)$ for obj_4/4 using *a priori* knowledge of object support. Field-of-view 64x64 cm².

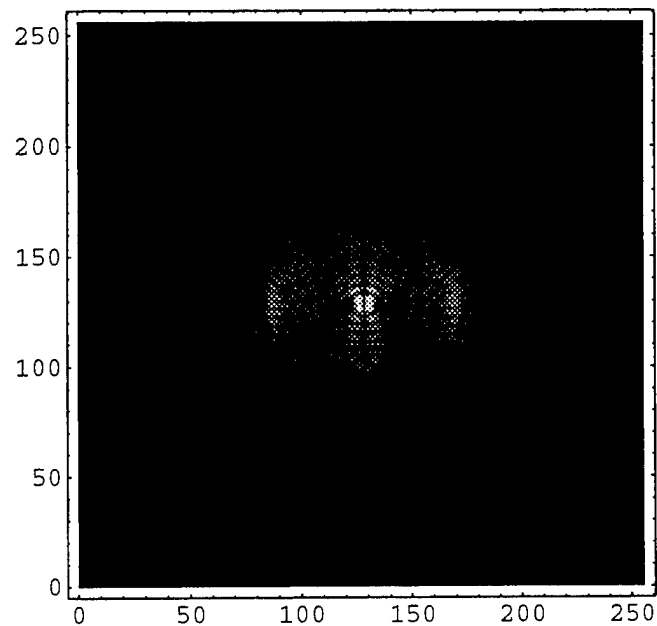


Figure 93 Magnitude of the differential cepstrum of $\frac{\mathcal{V}\Psi}{\Psi^i} ** h$ for obj_4/4 using *a priori* knowledge of object support.

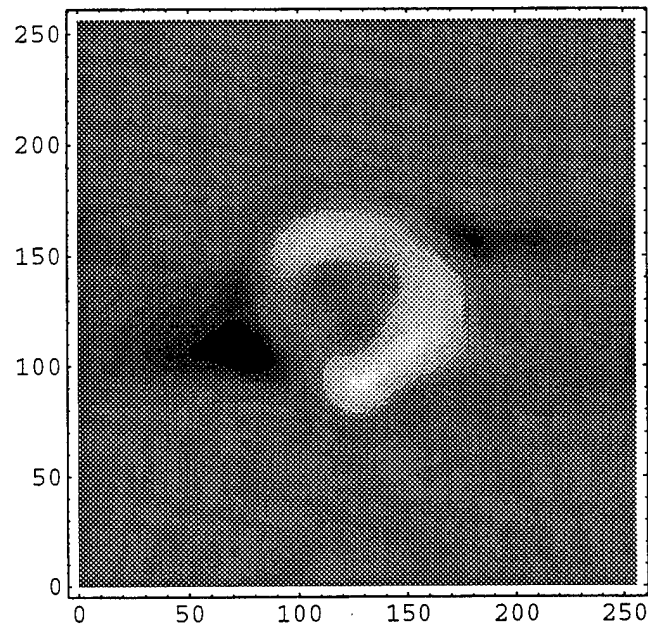


Figure 94 Magnitude of the reconstructed image of V after low pass filtering in the differential cepstral domain of obj 4/4 (using *a priori* knowledge of object support). Field-of-view $64 \times 64 \text{ cm}^2$.

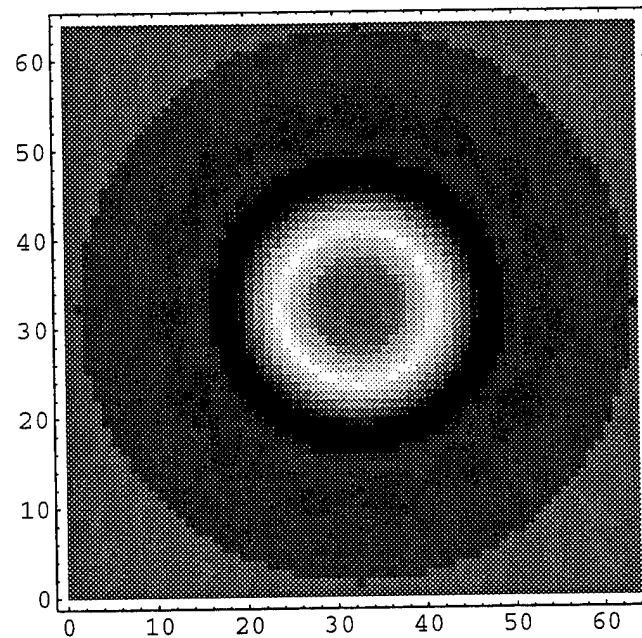


Figure 95 Magnitude of the image in Figure 94 averaged over 15 equally spaced views. Field-of-view $64 \times 64 \text{ cm}^2$.

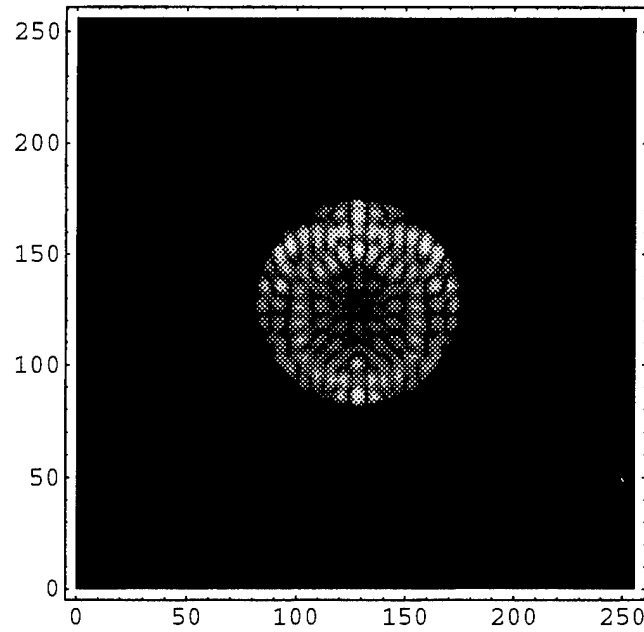


Figure 96 Magnitude of single-view backpropagated image $\left(\frac{\nu\Psi}{\Psi^i} ** h\right)$ for obj_4/2 using *a priori* knowledge of object support. Field-of-view 64x64 cm².

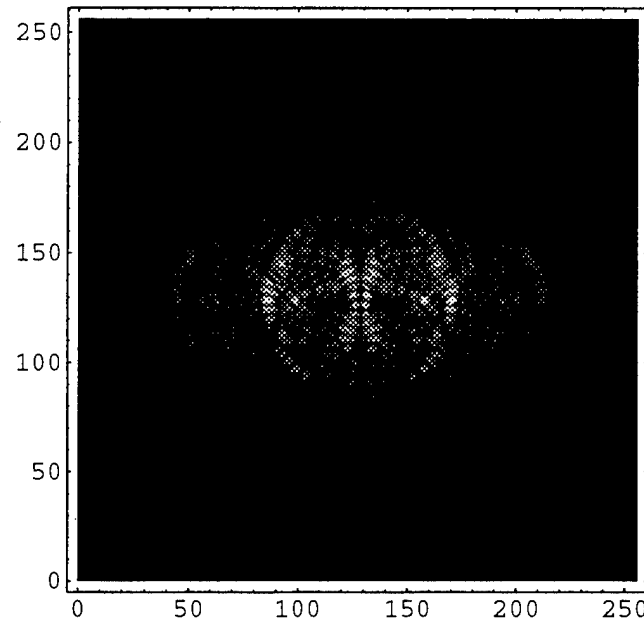


Figure 97 Magnitude of the differential cepstrum of $\frac{\nu\Psi}{\Psi^i} ** h$ for obj_4/2 using *a priori* knowledge of object support.

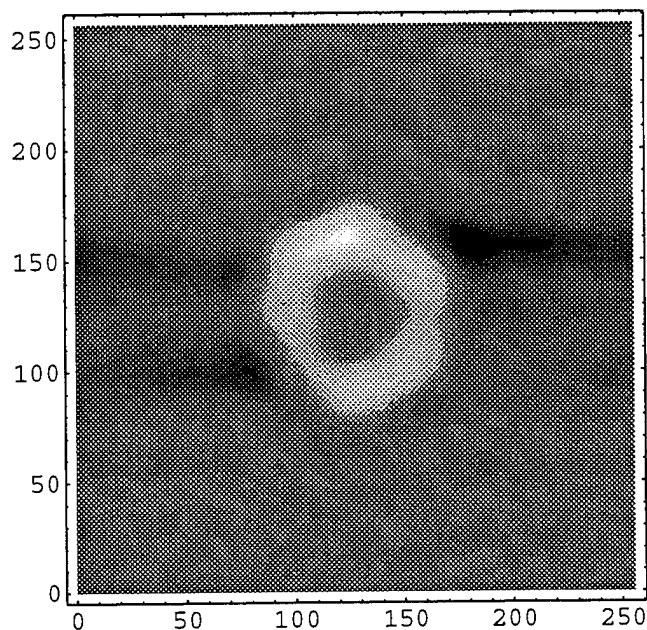


Figure 98 Magnitude of the reconstructed image of V after low pass filtering in the differential cepstral domain of obj_4/2 (using *a priori* knowledge of object support). Field-of-view $64 \times 64 \text{ cm}^2$.

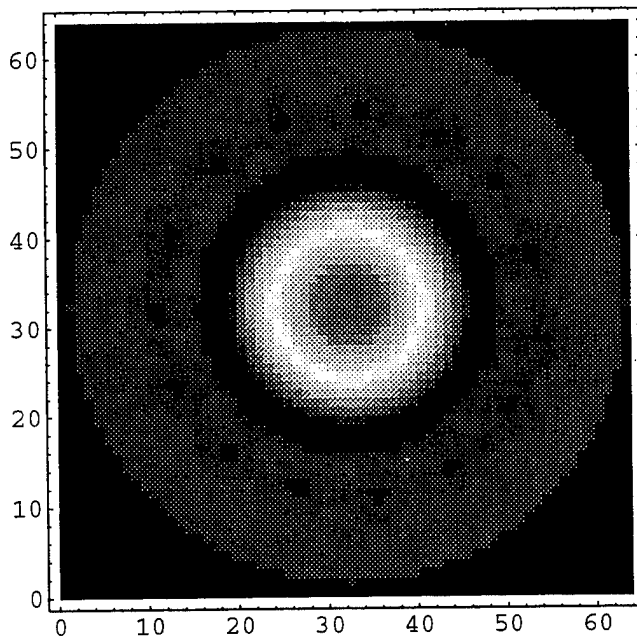


Figure 99 Magnitude of the image in Figure 98 averaged over 15 equally spaced views. Field-of-view $64 \times 64 \text{ cm}^2$.

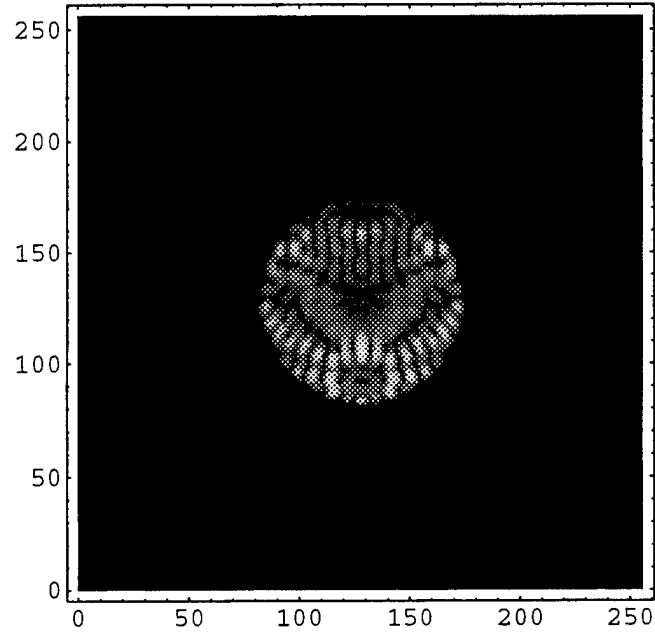


Figure 100 Magnitude of single-view backpropagated image $\left(\frac{\nabla\Psi}{\Psi^i} ** h\right)$ for obj_2/4 using *a priori* knowledge of object support. Field-of-view 64x64 cm².

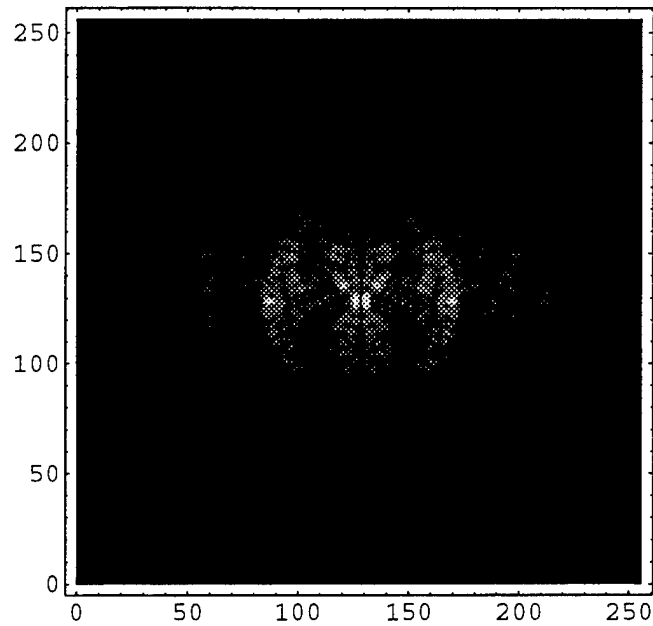


Figure 101 Magnitude of the differential cepstrum of $\frac{\nabla\Psi}{\Psi^i} ** h$ for obj_2/4 using *a priori* knowledge of object support.

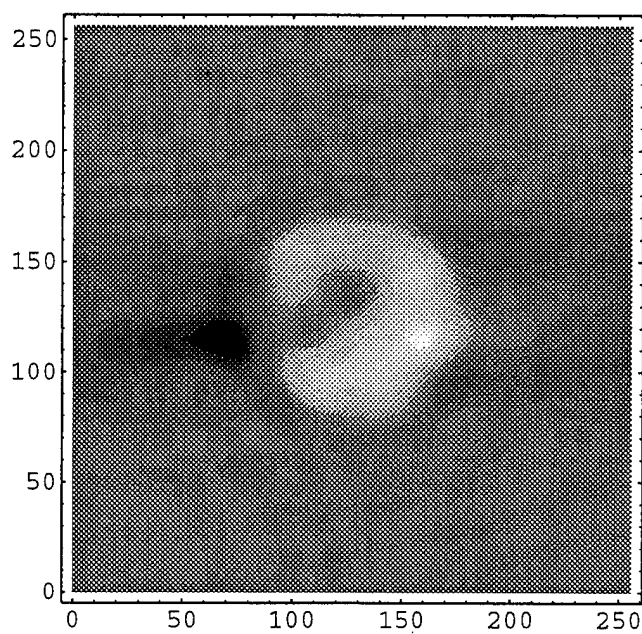


Figure 102 Magnitude of the reconstructed image of V after low pass filtering in the differential cepstral domain of obj_2/4 (using *a priori* knowledge of object support). Field-of-view $64 \times 64 \text{ cm}^2$.

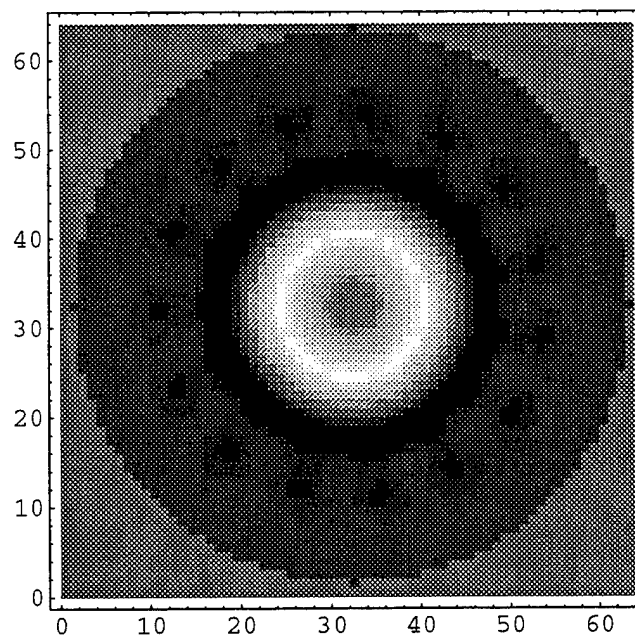


Figure 103 Magnitude of the image in Figure 102 averaged over 15 equally spaced views. Field-of-view $64 \times 64 \text{ cm}^2$.

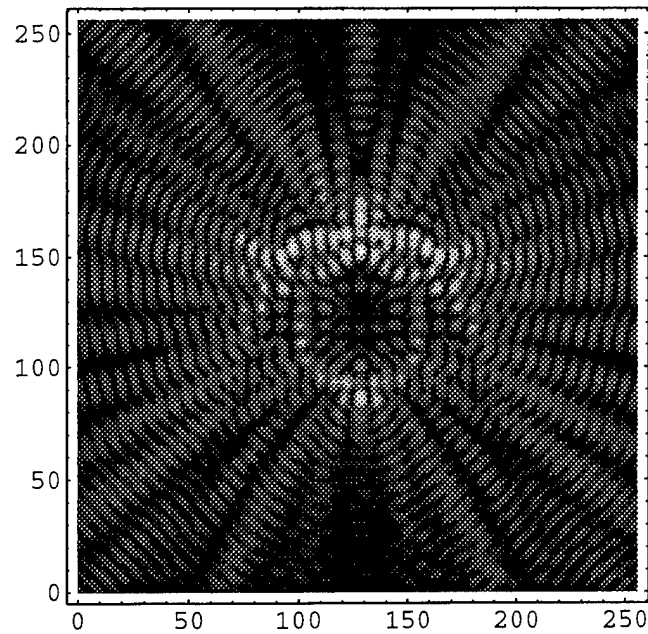


Figure 104 Magnitude of single-view backpropagated image $\left(\frac{\mathcal{V}\Psi}{\Psi^i} ** h\right)$ for obj_4/2 with S/N=20 dB. Field-of-view 64x64 cm².

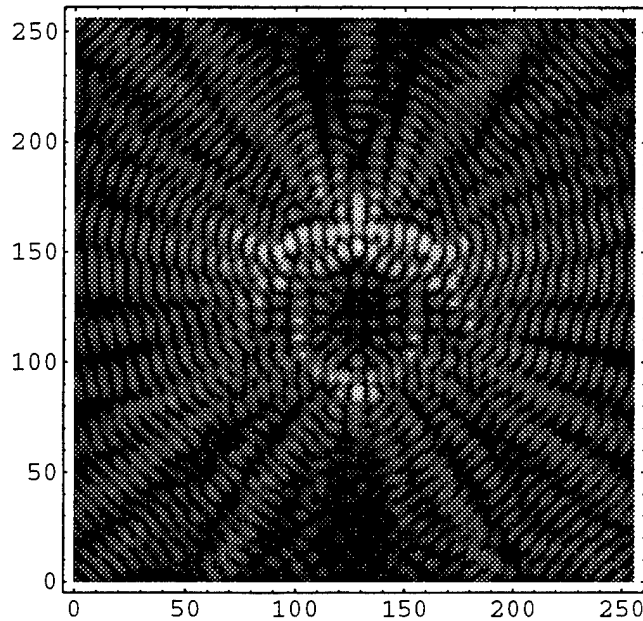


Figure 105 Magnitude of single-view backpropagated image $\left(\frac{\mathcal{V}\Psi}{\Psi^i} ** h\right)$ for obj_4/2 with S/N=15 dB. Field-of-view 64x64 cm².

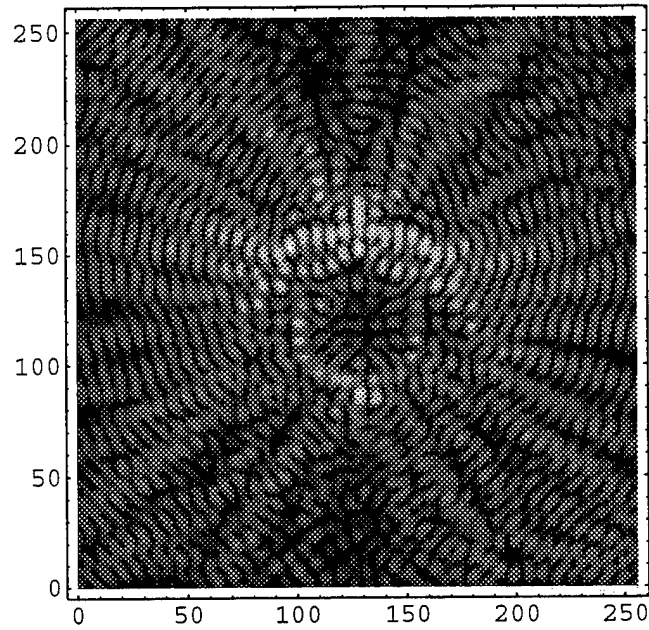


Figure 106 Magnitude of single-view backpropagated image $\left(\frac{\nabla\Psi}{\Psi^i} ** h\right)$ for obj_4/2 with S/N=10 dB. Field-of-view 64x64 cm².

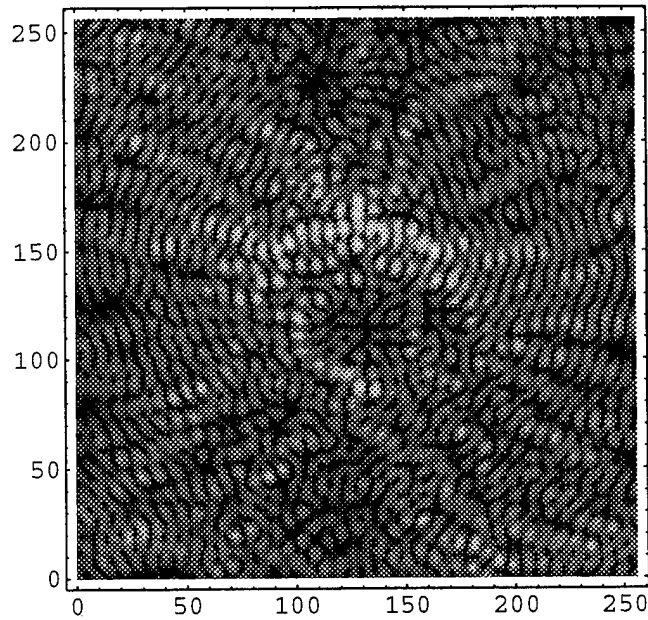


Figure 107 Magnitude of single-view backpropagated image $\left(\frac{\nabla\Psi}{\Psi^i} ** h\right)$ for obj_4/2 with S/N=5 dB. Field-of-view 64x64 cm².

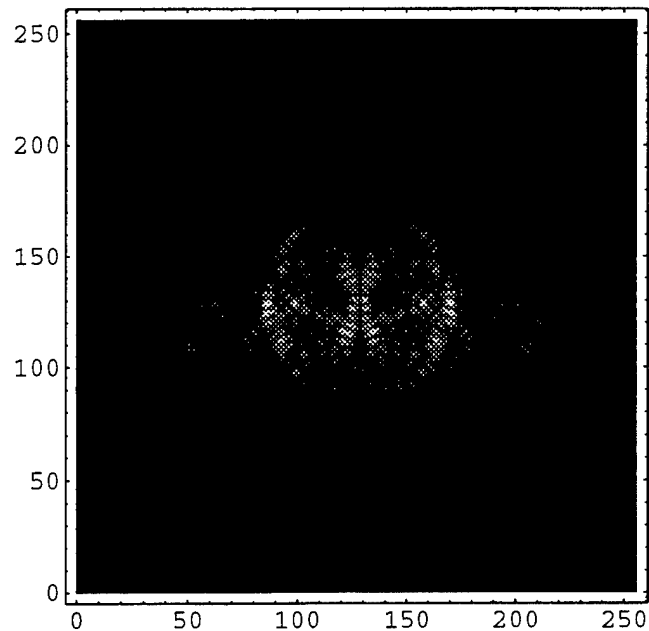


Figure 108 Magnitude of the differential cepstrum of $\frac{V\Psi}{\Psi^i} ** h$ for obj_4/2 using *a priori* knowledge of object support, S/N=20 dB.

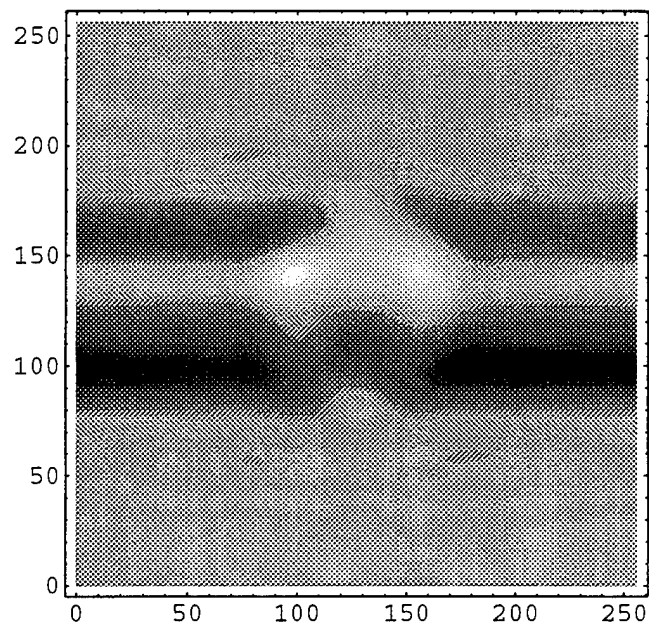


Figure 109 Magnitude of the reconstructed image of V after low pass filtering in the differential cepstral domain of obj_4/2, with S/N=20 dB (using *a priori* knowledge of object support). Field-of-view $64 \times 64 \text{ cm}^2$.

Figure 109. Although somewhat inferior to the noise-free case (Figure 98), the reconstruction in Figure 109 clearly shows the boundaries of obj_4/2. The algorithm is sensitive to noise because the various processing steps involved are nonlinear. As the differential cepstral filtering technique evolves, a more comprehensive noise analysis may be warranted.

13. DIFFERENTIAL CEPSTRAL FILTER APPLIED TO MEASURED DATA

Data were collected at Rome Laboratory's Ipswich, MA measurement facility and then processed. A homogeneous square dielectric cylinder was illuminated by a 10 GHz radar using a separated transmitter and receiver in a bistatic arrangement. The square cylinder was constructed of Styrofoam (polystyrene) and had a cross section of 13.6 cm by 13.6 cm. The height of the cylinder extended beyond the transmitter beam width and was considered infinite. For each of six fixed plane wave illumination directions, scattered far fields were collected every 1° for bistatic angles 0° to 180° .

The scattered fields map onto semi-circles in Fourier space and can be backpropagated into image space as described in Section 7. Figures 110 through 115 show the magnitudes of the backpropagated fields for the illumination directions 0° , 60° , 120° , 180° , 240° , and 300° , respectively.

Combinations of backpropagated fields from multiple views reveal an image that is equivalent to a Born reconstruction. In Figure 116, backpropagated fields are combined using the three different illumination directions 0° , 60° , and 120° . The magnitude of the image provides a crude estimate of the original object. As more views are added, the reconstruction improves. Figure 117 shows the magnitude of the equivalent Born reconstruction using the six views 0° , 60° , 120° , 180° , 240° , and 300° .

Only six views of the square cylinder were available due to time constraints on the measurement system. However, symmetry may be used to provide more Fourier data, which is valid only for a homogeneous case. That is, the data collected using a 0° illumination direction can be used to imitate data collected using a 90° illumination direction. Data collected at 60° can be used to imitate data collected at 150° , and so on. Figure 118 shows the magnitude of the equivalent Born reconstruction using twelve views assembled from six views actually measured and six views found through symmetry. Periodic structure within the image is an artifact that results from the field. A low-pass filter applied in the differential cepstrum of the twelve-view image produces Figure 119. To within the effects of low-pass filtering, Figure 119 shows a more uniform variation of permittivity that qualitatively agrees with the original object.

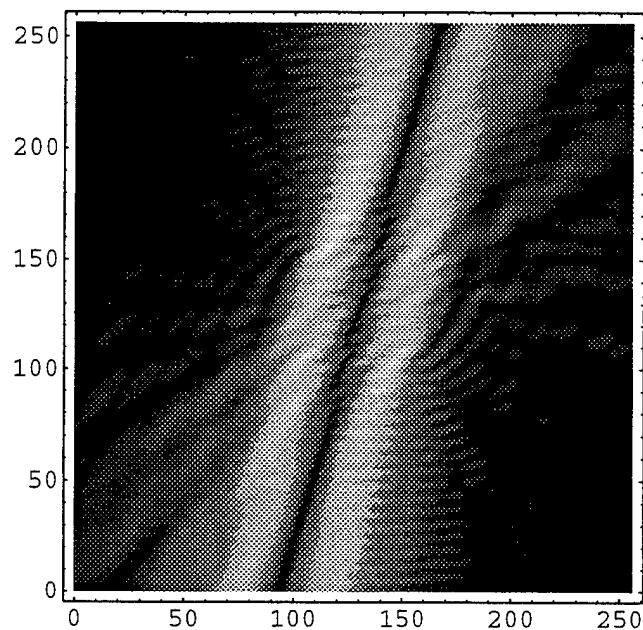


Figure 110 Magnitude of the single-view backpropagated image using bistatic angles 0° to 180° and incident angle 0° . Field-of-view $64 \times 64 \text{ cm}^2$.

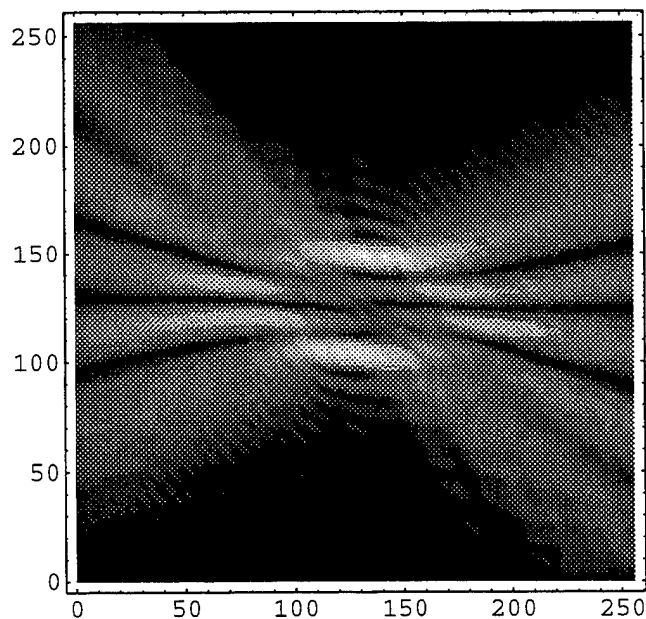


Figure 111 Magnitude of the single-view backpropagated image using bistatic angles 0° to 180° and incident angle 60° . Field-of-view $64 \times 64 \text{ cm}^2$.

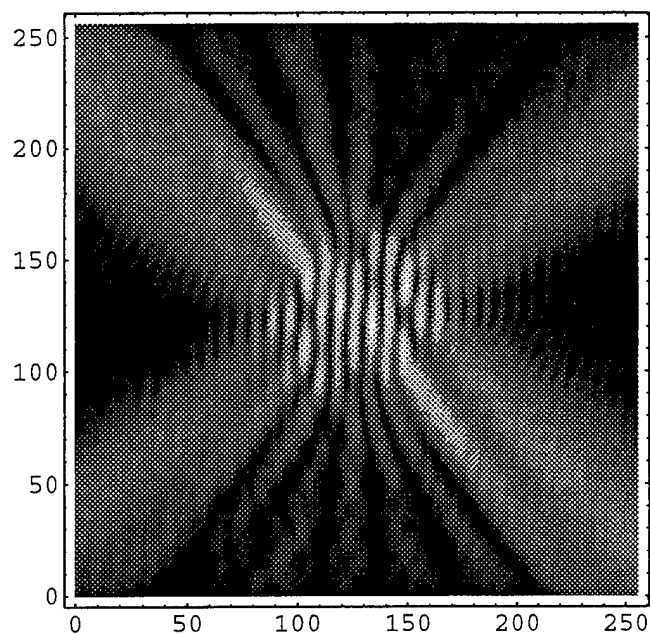


Figure 112 Magnitude of the single-view backpropagated image using bistatic angles 0° to 180° and incident angle 120° . Field-of-view $64 \times 64 \text{ cm}^2$.

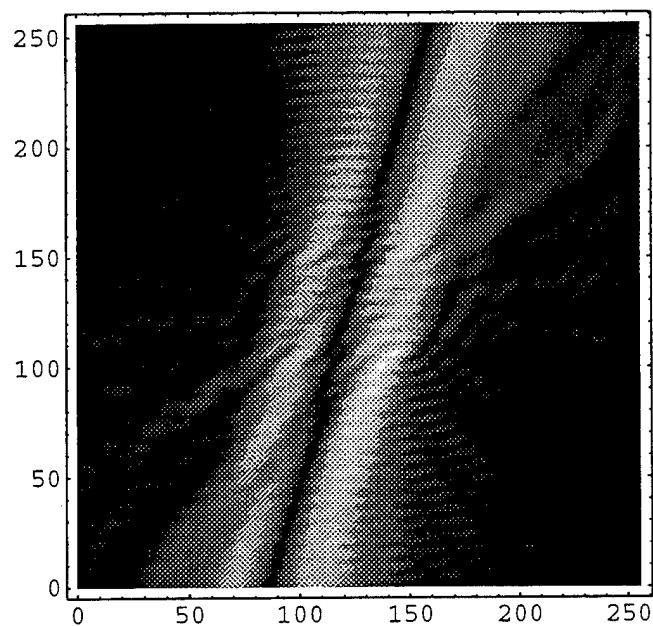


Figure 113 Magnitude of the single-view backpropagated image using bistatic angles 0° to 180° and incident angle 180° . Field-of-view $64 \times 64 \text{ cm}^2$.

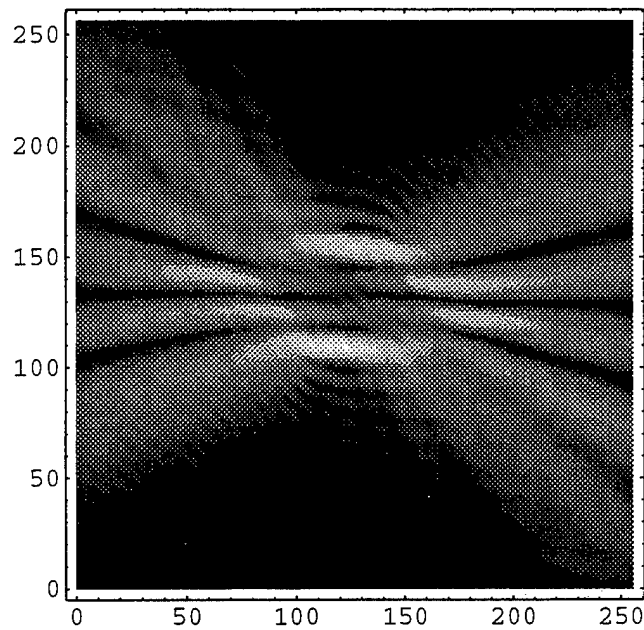


Figure 114 Magnitude of the single-view backpropagated image using bistatic angles 0° to 180° and incident angle 240° . Field-of-view $64 \times 64 \text{ cm}^2$.

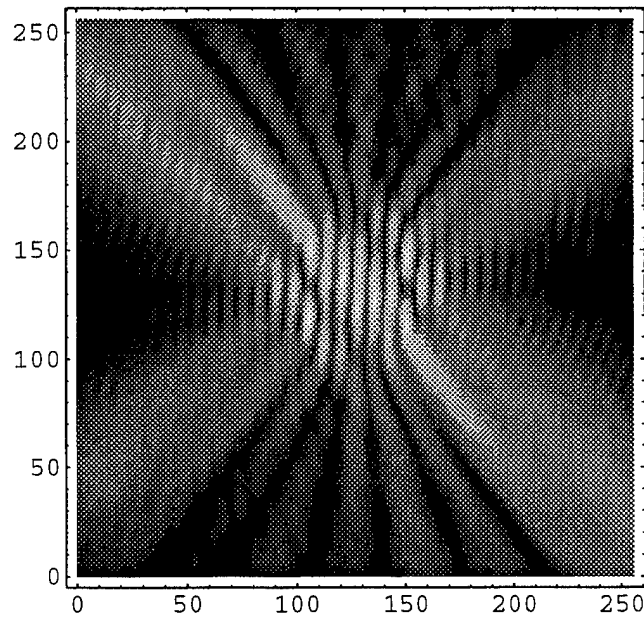


Figure 115 Magnitude of the single-view backpropagated image using bistatic angles 0° to 180° and incident angle 300° . Field-of-view $64 \times 64 \text{ cm}^2$.

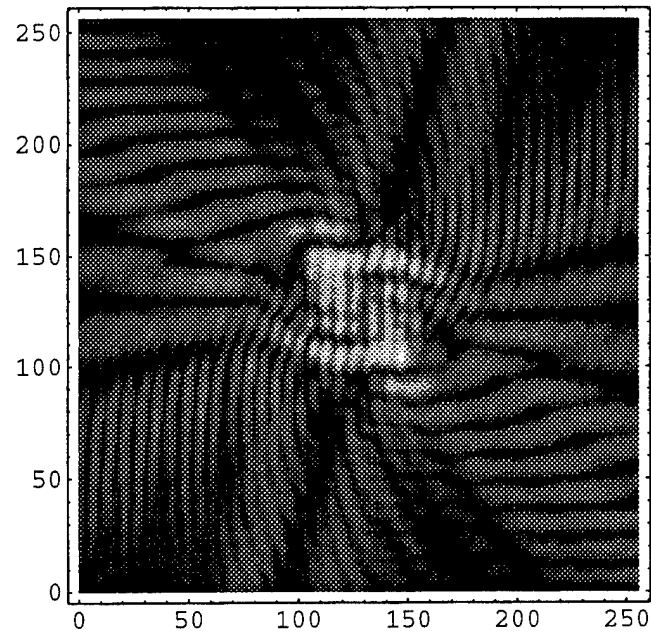


Figure 116 Magnitude of the equivalent Born reconstruction using three views (0° , 60° , 120°). Field-of-view $64 \times 64 \text{ cm}^2$.

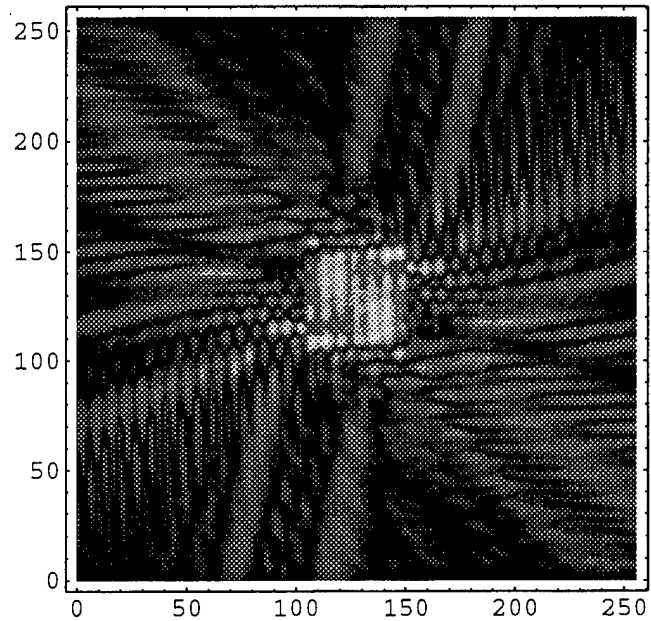


Figure 117 Magnitude of the equivalent Born reconstruction using six views (0° , 60° , 120° , 180° , 240° , 300°). Field-of-view $64 \times 64 \text{ cm}^2$.

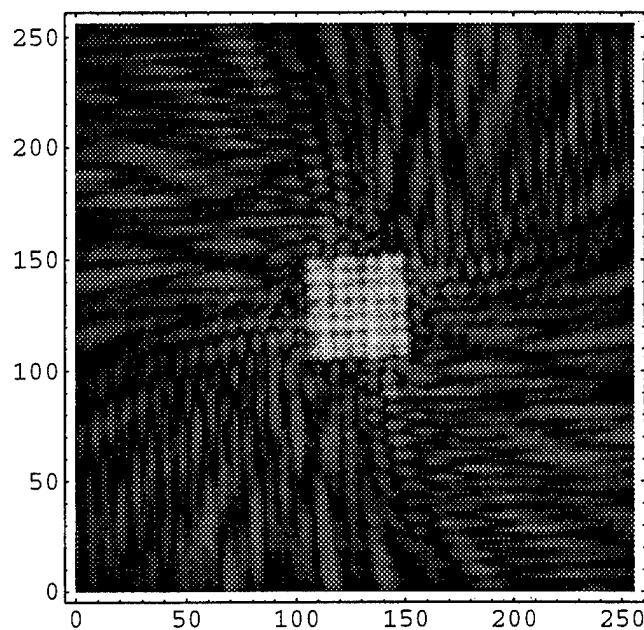


Figure 118 Magnitude of the equivalent Born reconstruction using twelve views (0° , 30° , 60° , 90° , 120° , 150° , 180° , 210° , 240° , 270° , 300° , 330°). Field-of-view $64 \times 64 \text{ cm}^2$.

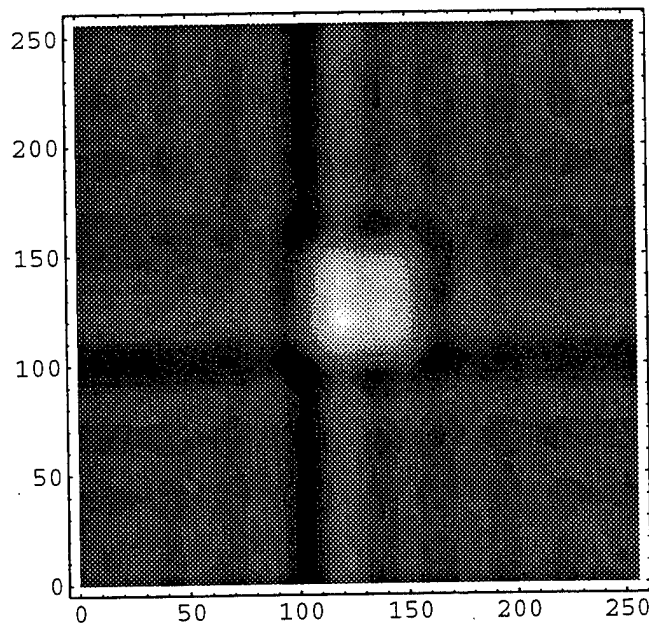


Figure 119 Magnitude of the resultant image when the differential cepstral filter is applied to the twelve-view reconstruction. Field-of-view $64 \times 64 \text{ cm}^2$.

14. CONCLUSIONS

The single-view backpropagated image generated from a strongly scattering object was shown to be the product of the scattering potential and the total field. A differential cepstral filter was then used to isolate an estimate of the scattering potential from the image since simple linear filtering is inappropriate for separating product functions. Sets of filtered single-view images were combined to better identify the scattering. This report presents the first application of this nonlinear filtering technique to single-view backpropagated images from two-dimensional strongly scattering objects, although McGahan [1992] successfully applied homomorphic filtering to one-dimensional slices of backpropagated images for both simulated and measured data.

Weak scattering approximations such as the Born or Rytov methods are well known to be inappropriate for objects that possess multiple scattering. The factor $\frac{\Psi(\mathbf{r}, \hat{\mathbf{r}}_i)}{\Psi^i(\mathbf{r}, \hat{\mathbf{r}}_i)}$ in the effective scattering potential of Eq. (7.15) complicates our interpretation of the true scattering potential by modulating the image of $V(\mathbf{r})$. In Sections 5 and 6, several examples were shown to illustrate the complexity of the internal field for strongly scattering concentric cylinders.

The inverse differential cepstral transform was simplified by defining the differential cepstrum as the spectrum of the derivative with respect to x of the logarithm of the function. As discussed in Section 9, this allows one to use integration with respect to x and exponentiation for the inverse transformation. Phase-wrapping artifacts due to use of the logarithm are, thereby, avoided. Of course, the differential cepstrum could have been defined using a derivative along some other arbitrary direction, or in both the x and y directions. The benefits of such options remain to be explored.

A promising reconstruction is shown in Figure 98. In this figure, good qualitative agreement is found with the profile of obj_4/2. This example represents $k_0|\sqrt{\varepsilon_r} - 1|a \cong 41$ and is a strong scatterer by our definition that $k_0|\sqrt{\varepsilon_r} - 1|a < \pi$ for those objects that satisfy the Born approximation. A priori information concerning the object's size was used in this reconstruction. Only backpropagated data within a region loosely bounding the object's domain D were processed, the rest were set to zero. In this way, unwanted cepstral components are removed and better separation of the scattering potential and total field is possible.

The fact that Figure 102 shows poor qualitative agreement with the complementary object obj_2/4 may imply that more care is needed in excising the field factor in the differential cepstral domain. A simple low-pass filter was used throughout this report, rather than a well defined, but generic, notch filter.

Other researchers have tried to image strongly scattering objects and have achieved varying degrees of success. Duchene, et al, [1985] simply performed a Born inversion on strong scatterers even though there was no clear relationship between the processed image and the scattering potential. Consequently, the reconstructed images showed poor agreement with the original scattering potentials.

Feinberg and Rebane [1994] recently proposed a technique that involves time gating the received signal so that multiply scattered components (those that arrive later in time due to the increased path length) are effectively truncated. This particular imaging method uses visible light as the source and measures an attenuation profile for the intervening medium. In diffraction tomography, we cannot, however, exploit a similar procedure since the scattered field is characterized by a diffraction phenomenon rather than straight line propagation.

One difficulty with our proposed method is that Fourier data are limited to an offset circle in 2-D Fourier space according to Eq. (7.11) when a fixed illumination direction is used. Higher spatial frequencies are filtered out by the limited Fourier domain that is accessible. As a result, fine detail in the reconstructed images of more strongly scattering structures with higher permittivities is not resolved. One might argue that this selective filtering improves the obtainable image; however, the point spread function (PSF) in the backpropagated image becomes more pronounced. In this case, the convolution term $h_{sv}(\mathbf{r}, \hat{\mathbf{r}}_i)$ in Eq. (7.20) cannot be neglected and the differential cepstral filtering routine may need modification to accommodate the PSF. The first sidelobe of the PSF is approximately 8 dB below the peak value and will limit the final image contrast by the same amount.

In principle, one would like to reduce the smearing effect of the PSF (that is, make it more like an ideal delta function) by using multiple illumination directions or multiple wavelengths. However, $V(\mathbf{r}) \frac{\Psi(\mathbf{r}, \hat{\mathbf{r}}_i)}{\Psi^i(\mathbf{r}, \hat{\mathbf{r}}_i)}$ varies strongly with both $\hat{\mathbf{r}}_i$ and k_0 although the dependence on k_0 is not shown explicitly within the arguments since a single wavenumber was assumed throughout this report. Therefore, any appreciable change in these values provides Fourier data for a very different effective scattering potential.

15. RECOMMENDATIONS

Differential cepstral filtering applied to single-view backpropagated images of strong scatterers is a developing technique. The purpose of this report is to demonstrate the validity and applicability of this technique to strong scatterers. In Section 10, a simple low-pass filter was used to filter the differential cepstrum of exact $V(\mathbf{r}) \frac{\Psi(\mathbf{r}, \hat{\mathbf{r}}_i)}{\Psi^i(\mathbf{r}, \hat{\mathbf{r}}_i)}$ for several objects. A result consistent with the data was found, in each case, demonstrating the validity of the method.

However, backpropagated images of the more strongly scattering objects were found to be convolved with a point spread function due to limited Fourier data. The PSF blurred the higher spatial frequencies associated with an increased relative permittivity. To mitigate the effects of the PSF, it is recommended that a superresolution technique be used for frequency space extrapolation. This technique should provide a better estimate of $V(\mathbf{r}) \frac{\Psi(\mathbf{r}, \hat{\mathbf{r}}_i)}{\Psi^i(\mathbf{r}, \hat{\mathbf{r}}_i)}$ for strong scatterers.

The concurrent use of multiple frequencies does not readily lend itself to improving the PSF. However, use of two, or more, frequencies may help separate components of $V(\mathbf{r})$ from $\frac{\Psi(\mathbf{r}, \hat{\mathbf{r}}_i)}{\Psi^i(\mathbf{r}, \hat{\mathbf{r}}_i)}$ in the differential cepstral domain. If $V(\mathbf{r})$ is nondispersive (that is, $V(\mathbf{r})$ does not vary with k_0), cepstral components of $V(\mathbf{r})$ should not change when a new frequency is introduced. The cepstral components of $\frac{\Psi(\mathbf{r}, k_0 \hat{\mathbf{r}}_i)}{\Psi^i(\mathbf{r}, k_0 \hat{\mathbf{r}}_i)}$ will differ due to the dependence on k_0 .

Use of the two frequency approach may lead to the design of more effective filters in the differential cepstral domain.

Combinations of post-filtered images using multiple frequencies may improve estimates of $V(\mathbf{r})$. In this case, the frequency dependent factor $\frac{\Psi(\mathbf{r}, k_0 \hat{\mathbf{r}}_i)}{\Psi^i(\mathbf{r}, k_0 \hat{\mathbf{r}}_i)}$ is theoretically removed through proper filtering at each frequency.

The differential cepstral filtering technique represents a novel application of homomorphic signal processing to the inverse problem for strong scatterers. Perhaps, as the technique matures, many of the present challenges can be overcome. The most exciting aspect of this effort will be the realization of the potential benefits of the technique in the areas of target identification, medical imaging, nondestructive evaluation, and geophysical imaging.

REFERENCES

- Balanis, C.A., Antenna Theory, Harper & Row Publishers, New York, 1982.
- Beyer, W.H., CRC Standard Mathematical Tables, CRC Press, Inc., 26th edition, Boca Raton, Florida,
- Bogert, R.P., M.J. Healy and J.W. Tukey, The quefrency alanalysis of time series for echoes: cepstrum, pseudo-autocovariance, cross-cepstrum and saphe cracking, in Time Series Analysis, Edited by M. Rosenblatt, John Wiley and Sons, Inc., New York, 1963.
- Bracewell, R., The Fourier Transform and its Applications, McGraw-Hill Book Company, New York, 1965.
- Brigham, E. O., The Fast Fourier Transform and its Applications, Prentice Hall, Englewood Cliffs, New Jersey, 1988.
- Butkov, E., Mathematical Physics, Addison-Wesley Publishing Co., Reading, Massachusetts, 1968.
- Caorsi, S., G.L. Gragnani and M. Pastorino, "Two-dimensional microwave imaging by a numerical inverse scattering solution," IEEE Transactions on Microwave Theory and Techniques, Vol. 38, No. 8, pp. 981-989, August 1990.
- Chew, W.C., Waves and Fields in Inhomogeneous Media, Van Nostrand Reinhold, New York, 1990.
- Devaney, A.J., "Nonuniqueness in the inverse scattering problem," Journal of Mathematical Physics, 19, pp. 1526-1531, July 1978.
- Devaney, A.J., "Inverse-scattering theory within the Rytov approximation," Optics Letters, Vol. 6, No. 8, pp. 374-376, 1981.
- Devaney, A.J., "A filtered backpropagation algorithm for diffraction tomography," Ultrasonic Imaging, Vol. 4, pp. 336-350, 1982.
- Duchene, B., D. Lesselier and W. Tabbara, "Diffraction tomography approach to acoustical imaging and media characterization," Journal Optical Society of America, A, Vol. 2, No. 11, pp. 1943-1953, 1985.
- Feinberg J. and A. Rebane, "Imaging without x rays", Optical Engineering Reports, Published by SPIE, No. 131, November 1994.

Fiddy, M.A., "Inversion of optical scattered field data," Journal of Physics, D: Applied Physics, Vol. 19, 301-317, 1986.

Grossman, S. I., Multivariable Calculus, Linear Algebra, and Differential Equations, Academic Press, Inc., Orlando, 1986

Harrington, R.F., Time-Harmonic Electromagnetic Fields, McGraw-Hill Book Co., Inc., New York, 1961.

Ho, P.C. and W.H. Carter, "Structural measurement by inverse scattering in the first Born Approximation," Applied Optics, Vol. 15, No. 2, 1976.

Ishimaru A., Electromagnetic Wave Propagation, Radiation, and Scattering, Prentice Hall, Englewood Cliffs, New Jersey, 1991.

Jones D.S., The Theory of Electromagnetism, Pergamon Press, The Macmillian Company, New York, 1964.

Lin, F.C. and M.A. Fiddy, "Image estimation from scattered field data," International Journal of Imaging Systems and Technology, Vol. 2, 76-95, 1990.

Lin, F.C. and M.A. Fiddy, "The Born-Rytov controversy: I. Comparing analytical and approximate expressions for the one-dimensional case," Journal of the Optical Society of America A, Vol. 9, No. 7, 1992.

McGahan, R.V., Image Reconstruction From Real Data Using Homomorphic Filtering, D.Eng. Dissertation, University of Massachusetts, Lowell, 1992.

Morita, N., Kumagai and N., Mautz, J.R., Integral Equation Methods for Electromagnetics, Artech House, Boston, 1990.

Morse P.M. and H. Feshbach, Methods of Theoretical Physics, Part I, McGraw-Hill Book Co., Inc., 1953.

Morse P.M. and H. Feshbach, Methods of Theoretical Physics, Part II, McGraw-Hill Book Co., Inc., 1953.

Mueller, R.K., M. Kaveh and G. Wade, "Reconstructive tomography and applications to ultrasonics," Proceedings of the IEEE, Vol. 67, No. 4, pp. 567-587, April 1979.

Oppenheim, A.V., "Superposition in a class of non-linear systems," Research Lab. of electronics, M.I.T. , Cambridge, MA, Tech . Rept. 432, March 31, 1965.

Oppenheim, A.V., R.W. Schafer and T.G. Stockham, "Nonlinear filtering of multiplied and convolved signals," Proceedings of the IEEE, Vol. 56, No. 8, pp. 1264-1291, August 1968.

Oppenheim, A.V. and R.W. Schafer, Digital Signal Processing, Prentice-Hall, Englewood Cliffs, New Jersey, 1975.

Pan, S.X. and A.C. Kak, "A computational study of reconstruction algorithms from diffraction tomography: interpolation versus backpropagation," IEEE Transactions on Acoustic, Speech, Signal Processing, Vol. ASSP-31, pp. 1262-1275, Oct. 1983.

Papoulis, A., Systems and Transforms with Applications in Optics, McGraw-Hill, New York, 1968.

Pichot, C., L. Jofre, G. Peronnet and J.C. Bolomey, "Active microwave imaging of homogeneous bodies," IEEE Transactions on Antennas and Propagation, Vol. AP-33, No. 4, 416-425, 1985.

Polydoros, A. and A.T. Fam, "The differential cepstrum: definition and properties," 1981 IEEE International Symposium on Circuits and Systems Proceedings, Chicago, IL, Vol. 1, pp. 77-80, April 1981.

Raghuramireddy and D., R. Unbehauen, "The two-dimensional differential cepstrum," IEEE Transactions on Acoustics, Speech, and Signal Processing, Vol. ASSP-33, No. 4, pp. 1335-1337, October 1985.

Raghuramireddy and D., R. Unbehauen, "Multidimensional homomorphic deconvolution systems," Proceedings of 24th Conference on Decision and Control, Ft. Lauderdale, FL, pp. 1606-1612, December 1985.

Richmond, J. H., "Scattering by a dielectric cylinder of arbitrary cross section shape," IEEE Transactions on Antennas and Propagation, AP-13, No. 3, pp. 334-341, May 1965.

Ruck, G.T., Radar Cross Section Handbook, Vol. 1, Plenum Press, New York, 1970.

Scivier M.S. and M.A. Fiddy, "Phase ambiguities and the zeros of multidimensional band-limited functions," Journal of the Optical Society America, A2, pp. 693-697, 1985.

Slaney M., A.C. Kak and L.E. Larsen, "Limitations of imaging with first-order diffraction tomography," IEEE Transactions on Microwave Theory and Techniques, Vol. MTT-32, No. 8, 860-874, 1984.

Tatarski V.I., Wave Propagation in a Turbulent Medium, McGraw-Hill, New York, 1961.

Tang, C.H., "Backscattering from dielectric-coated infinite cylindrical obstacles," Journal of Applied Physics, Vol. 28, No. 5, 628-633, 1957.

Tribolet, J. M., "A new phase unwrapping algorithm," IEEE Transactions on Acoustics, Speech, and Signal Processing, ASSP -25, pp. 170-177, 1977.

Van Bladel, J., Electromagnetic Fields, Hemisphere Publishing Corp., New York, 1985.

Wolf E., "Three-dimensional structure determination of semi-transparent objects from holographic data," Optics Communications, Vol. 1, No. 4, 153-156, 1969.

APPENDIX A. FAR-FIELD APPROXIMATION

Given the source (r', ϕ') and observation (r, ϕ) coordinates, we wish to approximate $|\mathbf{r} - \mathbf{r}'|$ for the case $|\mathbf{r}| \gg |\mathbf{r}'|$. Although the solution is given in many textbooks including [Balanis, 1982, p. 114] and [Van Bladel, 1985, p. 214], its derivation will be shown here to provide a more complete understanding of the approximation.

Using the law of cosines applied to the triangle formed by sides \mathbf{r}, \mathbf{r}' and $\mathbf{r} - \mathbf{r}'$, one may write

$$|\mathbf{r} - \mathbf{r}'| = [r^2 - 2rr' \cos(\phi - \phi') + r'^2]^{1/2} \quad (\text{A.1})$$

Recall the following binomial expansion [Beyer, 1981, p. 347]

$$(x + y)^n = x^n + nx^{n-1}y + \frac{n(n-1)}{2!}x^{n-2}y^2 + \dots \quad (y^2 < x^2) \quad (\text{A.2})$$

Letting $x = r^2$, $y = -2rr' \cos(\phi - \phi') + r'^2$, and $|\mathbf{r}| \gg |\mathbf{r}'|$ the far-field approximation to (A.1) becomes

$$\begin{aligned} |\mathbf{r} - \mathbf{r}'| &\cong r - r' \cos(\phi - \phi') \\ &= r - \mathbf{r}' \cdot \hat{\mathbf{r}} \end{aligned} \quad (\text{A.3})$$

Only the first two terms were considered significant in the expansion since the rest degrades as r^{-1} and faster.

APPENDIX B. 2-D INVERSE FOURIER TRANSFORM

Although the inverse Fourier transform is defined in many texts, for example [Bracewell, 1965], and [Brigham, 1988], its derivation is not. In this appendix, we briefly review the derivation of the inverse Fourier transform for a function of two variables.

Given the forward Fourier transform

$$X(\omega_1, \omega_2) = \int_{t_2=-\infty}^{\infty} \int_{t_1=-\infty}^{\infty} x(t_1, t_2) e^{-i\omega_1 t_1} e^{-i\omega_2 t_2} dt_1 dt_2 \quad (\text{B.1})$$

we desire to solve for $x(t_1, t_2)$. First, multiply both sides of (B.1) by $e^{i\omega_1 \tau_1} e^{i\omega_2 \tau_2}$ and integrate over ω_1 and ω_2 to obtain

$$\begin{aligned} \int_{\omega_2=-\infty}^{\infty} \int_{\omega_1=-\infty}^{\infty} X(\omega_1, \omega_2) e^{i\omega_1 \tau_1} e^{i\omega_2 \tau_2} d\omega_1 d\omega_2 = \\ \int_{\omega_2=-\infty}^{\infty} \int_{\omega_1=-\infty}^{\infty} \left[\int_{t_2=-\infty}^{\infty} \int_{t_1=-\infty}^{\infty} x(t_1, t_2) e^{-i\omega_1 t_1} e^{-i\omega_2 t_2} dt_1 dt_2 \right] e^{i\omega_1 \tau_1} e^{i\omega_2 \tau_2} d\omega_1 d\omega_2. \end{aligned} \quad (\text{B.2})$$

Next, swap the order of integration in Eq. (B.2) to get

$$\begin{aligned} \int_{\omega_2=-\infty}^{\infty} \int_{\omega_1=-\infty}^{\infty} X(\omega_1, \omega_2) e^{i\omega_1 \tau_1} e^{i\omega_2 \tau_2} d\omega_1 d\omega_2 = \\ \int_{t_2=-\infty}^{\infty} \int_{t_1=-\infty}^{\infty} \left[\int_{\omega_2=-\infty}^{\infty} \int_{\omega_1=-\infty}^{\infty} x(t_1, t_2) e^{-i\omega_1 t_1} e^{-i\omega_2 t_2} e^{i\omega_1 \tau_1} e^{i\omega_2 \tau_2} d\omega_1 d\omega_2 \right] dt_1 dt_2. \end{aligned} \quad (\text{B.3})$$

The function $x(t_1, t_2)$ may be removed from the innermost two integrals in the right hand side of Eq. (B.3) since it does not vary with ω_1 or ω_2 . In this case, we write

$$\begin{aligned}
& \int_{\omega_2=-\infty}^{\infty} \int_{\omega_1=-\infty}^{\infty} X(\omega_1, \omega_2) e^{i\omega_1 \tau_1} e^{i\omega_2 \tau_2} d\omega_1 d\omega_2 = \\
& \int_{t_2=-\infty}^{\infty} \int_{t_1=-\infty}^{\infty} x(t_1, t_2) \left[\int_{\omega_2=-\infty}^{\infty} \int_{\omega_1=-\infty}^{\infty} e^{-i\omega_1 t_1} e^{-i\omega_2 t_2} e^{i\omega_1 \tau_1} e^{i\omega_2 \tau_2} d\omega_1 d\omega_2 \right] dt_1 dt_2.
\end{aligned} \tag{B.4}$$

Finally, using the following integral representation for the delta function [Papoulis, 1968, p. 99]

$$\delta(\tau_1 - t_1, \tau_2 - t_2) = \frac{1}{4\pi^2} \int_{\omega_2=-\infty}^{\infty} \int_{\omega_1=-\infty}^{\infty} e^{i\omega_1(\tau_1 - t_1)} e^{i\omega_2(\tau_2 - t_2)} d\omega_1 d\omega_2 \tag{B.5}$$

for the bracketed term in Eq. (B.4), we write the inverse 2-D Fourier transform

$$\frac{1}{4\pi^2} \int_{\omega_2=-\infty}^{\infty} \int_{\omega_1=-\infty}^{\infty} X(\omega_1, \omega_2) e^{i\omega_1 \tau_1} e^{i\omega_2 \tau_2} d\omega_1 d\omega_2 = x(\tau_1, \tau_2). \tag{B.6}$$

APPENDIX C. SIMULATED SCATTERED FAR-FIELDS

Figures C.1 through C.3 illustrate the magnitude and phase of the simulated scattered far-fields for obj_4/4 , obj_4/2 , and obj_2/4 . For these strongly scattering objects, we note that the information in the scattered field is indeed quite different for each object considered. The scattered far-fields are computed from the exact solution outlined in Section 6.

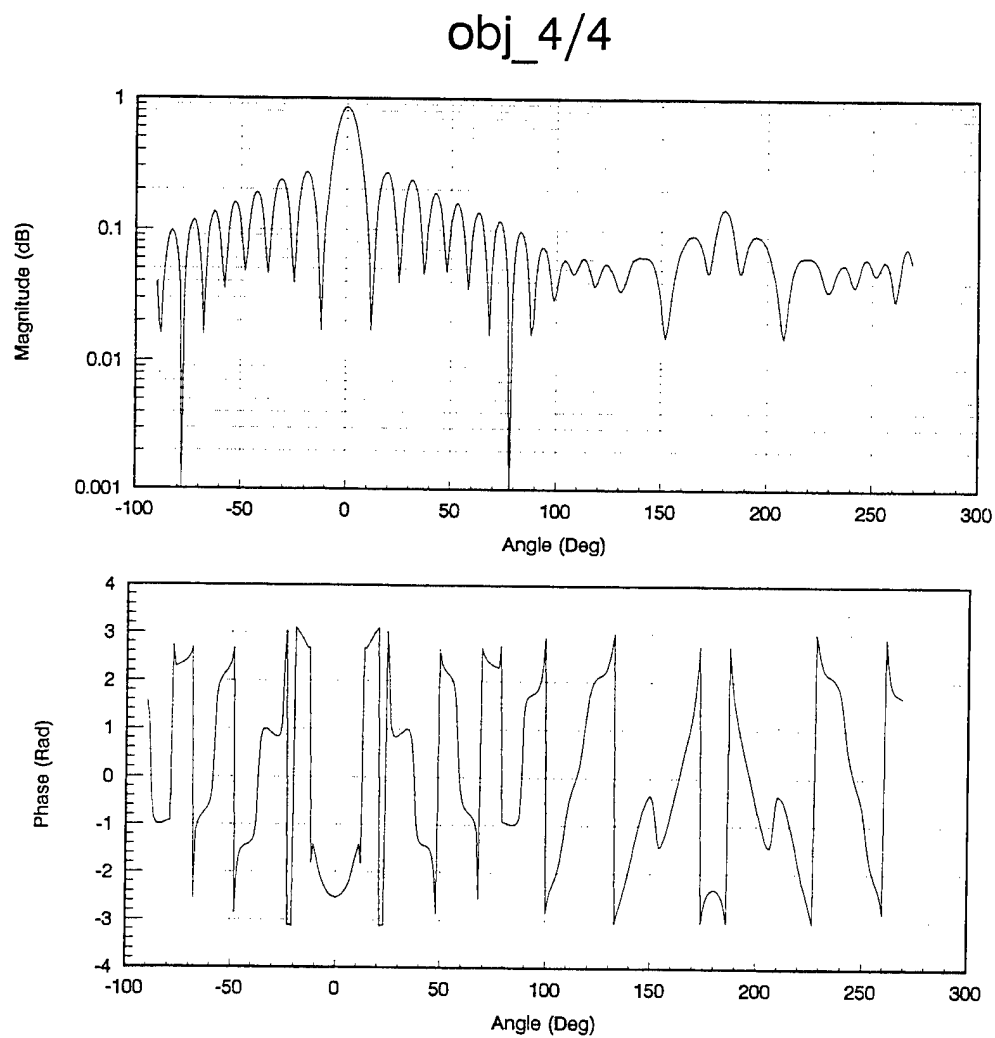


Figure C.1 Magnitude and Phase (simulated) of the scattered far-field from obj_4/4.

obj_4/2

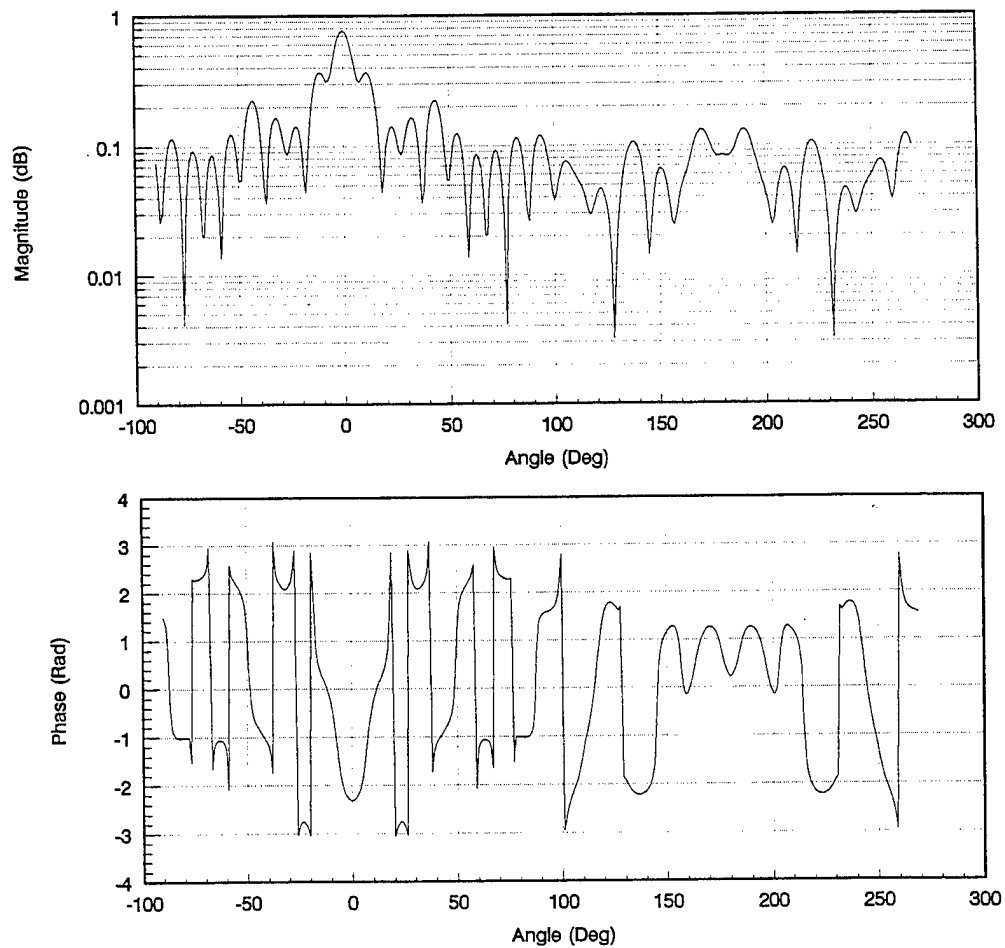


Figure C.2 Magnitude and Phase (simulated) of the scattered far-field from obj_4/2.

obj_2/4

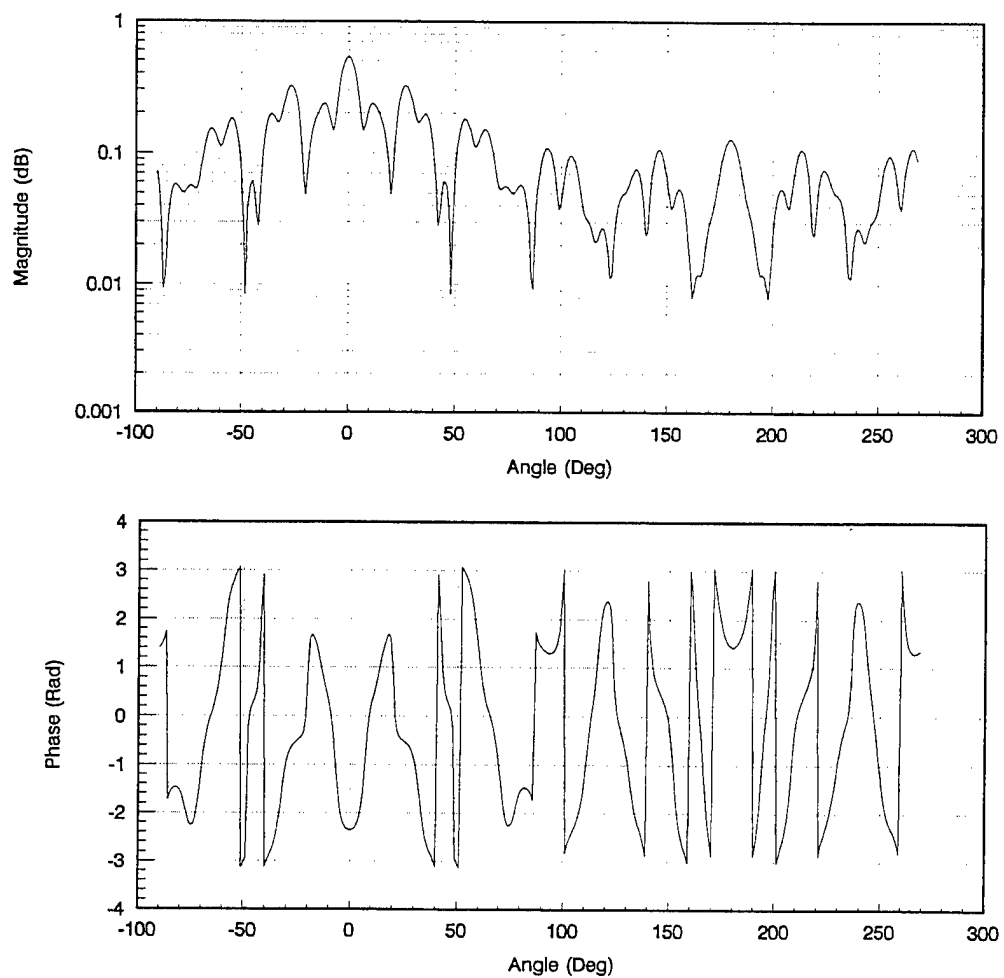


Figure C.3 Magnitude and Phase (simulated) of the scattered far-field from obj_2/4.